

The two-sided relativistic outflow in Cygnus A: extragalactic jet physics at extreme spatial resolution

INAUGURAL-DISSERTATION

zur
Erlangung des Doktorgrades
der Mathematisch-Naturwissenschaftlichen Fakultät
der Universität zu Köln



vorgelegt von

Biagina Boccardi

aus
San Martino in Pensilis, Italien

Koeln 2015

Berichterstatter:

Prof. Dr. J. Anton Zensus
Prof. Dr. Andreas Eckart

Tag der letzten mündlichen Prüfung: 20/10/2015

I dedicate this thesis to those who would have liked to study, but did not have the chance to do so.

I especially think to my 94-year-old grandfather, nonno Peppe, who had to leave school when he was 9 but still asks me what are stars made of.

Abstract

Extragalactic jets are collimated and magnetized outflows of relativistic plasma produced by accreting supermassive black holes. Although their understanding has significantly progressed over the years, the physical processes driving their launching, acceleration and collimation are still unclear. One reason is that the crucial mechanisms for jet formation take place on extremely small scales, and the angular resolution achievable in observations is only recently becoming sufficient. This thesis aims at investigating the nuclear regions of the jet in the radio galaxy Cygnus A through Very Long Baseline Interferometry (VLBI) observations down to millimeter wavelengths. The large viewing angle of this jet ($\theta \sim 75^\circ$) facilitates the study of the intrinsic properties of the flow thanks to the reduced geometrical and relativistic effects, and allows a counter-jet to be detected. At the source redshift ($z=0.056$), mm-VLBI can achieve a resolution of only ~ 200 Schwarzschild radii (R_S).

This thesis starts with an introduction to the physics of active galactic nuclei (AGN), with an emphasis on the radio-loud class (Chapter 1). A review of the currently most favored jet launching models is given in Chapter 2, complemented by a comparison with results from state-of-the-art observational studies. A large part of the work for this thesis was spent for the calibration and imaging of VLBI data, therefore Chapter 3 is dedicated to the description of this elegant and challenging observational technique. Chapter 4, 5 and 6 are focused on the study of Cygnus A, and the main findings are summarized in Chapter 7.

Monitoring of the source at 43 GHz (Chapter 4) reveals that the flow is parabolic in its acceleration region, which extends for $\sim 10^4 R_S$. Results are in agreement with predictions for a magnetically-driven jet confined by an external medium with mild pressure gradient. The presence of a speed transverse gradient with spine-sheath structure, likely giving rise to the limb brightening observed, is also inferred at 43 GHz. Its origin is further investigated in Chapter 5 at 86 GHz. At this frequency, the improved resolution enables to trace the limb brightened structure down to the base of the two-sided flow, suggesting that stratification is a direct result of the jet launching mechanism. The minimum jet transverse size of $135 \pm 27 R_S$ is much larger than the radius of the Innermost Stable Circular Orbit ($1-9 R_S$), implying that the launching region must involve also the outer part of the accretion disk. A spectral analysis in the frequency range 8–86 GHz (Chapter 6) constrains the location of the true central engine to coincide with a prominent gap of emission seen at 43 GHz

and at lower frequencies, at a distance of $\sim 1000 R_S$ from the 86 GHz core. The gap is a synchrotron self-absorbed region which becomes partially optically thin at 86 GHz. The counter-jet exhibits a flat or inverted spectrum up to high frequencies, compatible with the presence of a compact absorber extending between ~ 0.5 and 1.5 pc from the central engine. Spectral fitting indicates that the absorber may have a second, more diffuse component spread over the entire source.

Zusammenfassung

Extragalaktische Jets bezeichnen den gebündelten, magnetisierten, relativistischen Plasmafluss, der von extrem massereichen Schwarzen Löchern ausgeht, die von Akkretionsmaterial gespeist werden. Obwohl sich die Erkenntnisse über diese Objekte über die Jahre signifikant weiter entwickelt haben, sind die physikalischen Prozesse, die zur Entstehung, Bündelung und Beschleunigung der Jets führen, bisher nicht verstanden. Ein Grund dafür ist, dass die entscheidenden Mechanismen der Jetentstehung auf sehr kleinen Größenskalen wirken und erst in jüngerer Zeit die nötige Winkelauflösung erreicht wurde, um diese Skalen zu beobachten. Ziel dieser Arbeit ist es, die Kernregion des Jets in der Radiogalaxie Cygnus A mittels Very Long Baseline Interferometry (VLBI) Beobachtungen in verschiedenen Wellenlängenbereichen bis hin zu Millimeterwellenlängen zu untersuchen. Der große Blickwinkel ($\theta \sim 75^\circ$), unter dem dieser Jet betrachtet wird, ermöglicht es die intrinsischen Eigenschaften des Plasmafluxes zu untersuchen, da geometrische und relativistische Effekte gering ausfallen. Außerdem ist es möglich einen entgegengesetzten Ausfluss (counter-jet) zu beobachten. Bei der Rotverschiebung von $z = 0.056$ kann mit mm-VLBI Beobachtungen eine Auflösung von ca. 200 Schwarzschild-Radien erreicht werden.

Diese Arbeit beginnt mit einer Einleitung zur Physik aktiver Galaxienkerne (AGN) mit Fokus auf die Unterkategorie der radiolauten AGN (Kapitel 1). Die momentan favorisierten Modelle zur Jetentstehung werden in Kapitel 2 einleitend beschrieben und mit den Ergebnissen aktueller Beobachtungen auf dem neusten Stand der Technik verglichen. Ein großer Teil dieser Arbeit befasst sich mit der Kalibration und Abbildung (imaging) der VLBI-Daten. Daher ist Kapitel 3 der Beschreibung dieser eleganten und herausfordernden Beobachtungstechnik gewidmet. In den Kapiteln 4, 5 und 6 wird Cygnus A untersucht. Kapitel 7 fasst die wesentlichen Resultate zusammen.

Die regelmäßige Beobachtung bei 43 GHz zeigt, dass der Plasmafluss in der Region, in der dieser beschleunigt wird, parabolisch ist und sich diese Region über $\sim 10^4 R_S$ erstreckt (s. Kapitel 4). Die Ergebnisse stimmen mit den Vorhersagen für einen magnetisch angetriebenen Jet überein, der von einem externen Medium mit geringem Druckgradienten eingeschlossen ist. Des Weiteren wird bei 43 GHz ein Geschwindigkeitsgradient senkrecht zur Flussrichtung festgestellt, entsprechend der Struktur eines zentralen Fluxes umgeben

von einem Mantel (spine-sheath), welcher der potentielle Ursprung für die erhöhte Emission der Jetflanken (limb brightening) ist. Der Ursprung dieser Struktur wird in Kapitel 5 bei 86 GHz genauer untersucht. Die bessere Auflösung bei dieser Frequenz ermöglicht es, die Helligkeitsstruktur bis zum Ursprung des zweiseitigen Ausflusses zurückzuverfolgen. Dies legt nahe, dass die Schichtung des Flusses (stratification) eine direkte Konsequenz des Ursprungsmechanismus ist. Die Größe des Jets senkrecht zur Ausbreitungsrichtung wird auf mindestens $135 \pm 27 R_S$ geschätzt, wesentlich größer als Radius des innersten, stabilen, zirkularen Orbits (ISCO). Dies impliziert, dass die Region des Jetursprungs die äußeren Regionen der Akkretionsscheibe mit einschließt. Die Spektralanalyse des Frequenzbereichs 8-86 GHz (Kapitel 6) schränkt die Lage des zentralen Schwarzen Loches und der Akkretionsscheibe (central engine) dahingehend ein, dass diese mit einer Lücke in der Emission bei 43 GHz und niedrigeren Frequenzen übereinstimmt, die $\sim 1000 R_S$ vom 86 GHz-Kern entfernt ist. Diese Lücke entsteht durch die Selbstsorption der Synchrotronstrahlung. Bei 86 GHz hingegen wird die Region teilweise optisch dünn. Der entgegengesetzte Jet zeigt ein flaches oder invertiertes Spektrum bis zu höheren Frequenzen. Diese Invertierung kann durch eine kompakte Region absorbierenden Materials erklärt werden, welches sich über einen Bereich zwischen ~ 0.5 und 1.5 pc entfernt vom zentralen Objekt erstreckt. Das Fitten des Spektrums deutet darauf hin, dass die absorbierende Region eine zweite, diffusere Komponente hat, die sich über das gesamte Objekt ausweitet.

In this thesis, a Λ CDM cosmology with Hubble constant $H_0 = 70.5 \text{ h}^{-1} \text{ km s}^{-1} \text{ Mpc}^{-1}$, $\Omega_M = 0.27$, $\Omega_\Lambda = 0.73$ is assumed. The spectral index α is defined following the convention $S_\nu \propto \nu^\alpha$.

Contents

1	Active galactic nuclei	1
1.1	Dissecting an Active Galactic Nucleus	2
1.1.1	The supermassive black hole	4
1.1.2	The accretion disk	6
1.1.3	The Broad- and Narrow-line regions	8
1.1.4	The torus	9
1.2	The AGN zoo and the unified scheme	11
1.3	Relativistic Jets	13
1.3.1	Relativistic and geometrical effects	15
1.3.2	Radiation processes	18
1.3.3	The spectral energy distribution and the VLBI core	21
2	The formation of relativistic jets	25
2.1	Relativistic plasmas	26
2.1.1	Fundamental parameters	26
2.1.2	Fundamental relativistic MHD equations	26
2.1.3	MHD waves	28
2.1.4	Resistive MHD	28
2.2	The central engine: a unipolar inductor	29
2.2.1	Magnetic fields and jet power	31
2.2.2	The radio-loud / radio-quiet dichotomy	32
2.3	Acceleration and collimation	33
2.3.1	Observational constraints	35

3 Radio Interferometry	37
3.1 The radio window	38
3.2 Antenna basics	38
3.3 Interferometry	41
3.4 VLBI arrays	45
3.5 The calibration of VLBI data at mm-wavelengths	46
3.5.1 Inspecting the data in AIPS	47
3.5.2 Phase calibration	48
3.5.3 Amplitude calibration	49
3.6 Imaging and self-calibration	51
4 The stratified two-sided jet of Cygnus A: acceleration and collimation	53
4.1 Introduction	55
4.2 Observations and data reduction	56
4.3 Data analysis	58
4.3.1 Model fitting and alignment of the images	58
4.3.2 Transverse structure	61
4.4 Results	61
4.4.1 Kinematic analysis and components light-curves	61
4.4.2 Ridge-line	65
4.5 Discussion	66
4.5.1 Two-layers acceleration	66
4.5.2 Mean opening angle	67
4.5.3 Narrowing of the jet at $z \sim 2$ mas	69
4.5.4 Collimation regime	70
4.5.5 Comparison with M87	71
4.5.6 Nature of the gap of emission	72
4.6 Conclusions	72
5 GMVA observations	75
5.1 Data set and analysis	76
5.2 Intensity profiles	78
5.3 Alignment and proper motion	80

<i>CONTENTS</i>	ix
5.4 Width profile and jet origin	81
5.5 Size and structure of the jet base	83
5.6 Conclusions	84
6 High-resolution spectral study	87
6.1 Introduction	87
6.2 The multi-frequency data set	88
6.3 Alignment of maps at different frequencies	93
6.3.1 8 and 15 GHz	94
6.3.2 15 and 43 GHz	95
6.3.3 22 and 43 GHz	98
6.3.4 43 and 86 GHz	99
6.4 Spectral analysis	102
6.4.1 Ridge line spectrum	103
6.4.2 Spectral index maps	104
6.4.3 Spectral fitting	106
6.5 FFA opacity	110
6.6 Core shift	112
6.7 Conclusions	113
7 Conclusions and future work	115
A	119
Bibliography	121

Chapter 1

Active galactic nuclei

Since their discovery by Carl Seyfert in 1943, Active Galactic Nuclei (AGN) are among the most studied objects in the sky. Originally, the interest from astronomers was triggered by the mysterious nature of the newly discovered sources. The galaxies observed in the optical by Seyfert were really peculiar: they were characterized by a very bright, semi-stellar nucleus and by broad emission lines with velocities up to 8500 km s^{-1} ([Seyfert 1943](#)). In those same years, the first radio telescopes were built, unveiling the beauty of the radio sky for the first time. Next to the radio emission associated with the center of the Galaxy, other bright spots started to emerge. The angular resolution of the early radio telescopes was of course poor, and it was not until the development of the first interferometers that a fundamental property of these radio spots was understood: they were extremely compact. The increased positional accuracy in the radio also allowed to identify the optical counterparts, which turned out to be even smaller in size. These facts, together with the observed high brightness, led to the most plausible (or rather less unbelievable) conclusion: a new class of galactic sources, stars emitting strongly in radio, had been discovered. This scenario remained the most favored until the sixties, despite some disturbing evidence. For example, a spectroscopic study of the “radio-star” 3C 84 revealed unusual colors and broad emission lines which could not be identified with any known species ([Matthews & Sandage 1963](#)). Spectroscopy was exactly the tool which finally allowed to solve the mystery, in 1963. By examining the strong broad lines in the spectrum of another source, 3C 273, Maarten Schmidt recognized the pattern of the Balmer series of hydrogen, which was however red-shifted to completely different frequencies ([Schmidt 1963](#)). The inferred cosmological distance ($\sim 950 \text{ Mpc}$) implied that 3C 273 was the most powerful object ever observed! Since then, the redshifts of other similar sources were determined, and the extragalactic objects forming the new class were named *quasars* (Quasi-Stellar Radio Sources). Rapid variability

of the emission was, since the beginning, identified as one of the key features of the class. Most importantly, it allowed to obtain tight estimates on the emitting region sizes: by measuring the variability time scale and by assuming that no signal can travel faster than the speed of light, upper limits for the scale of the emitting regions can be obtained. In the case of quasars, these measurements implied that huge amounts of energy are produced in regions as small as few light months ([Rees 1970](#)). Accretion onto a super-massive black hole, i.e. conversion of gravitational energy into radiation, soon appeared as the most viable power source ([Zel'dovich & Novikov 1964](#); [Salpeter 1964](#); [Lynden-Bell 1969](#)).

In the following, I review the observational and physical properties of the building blocks of an AGN, I describe the main AGN classes and I discuss the attempt of unifying them through a simple model. Then, I focus on those AGN which are bright in the radio band due to the presence of a relativistic jet emanating from the center. In fact, the main target of my study, the powerful radio galaxy Cygnus A, is one them.

1.1 Dissecting an Active Galactic Nucleus

Active galactic nuclei are complex systems placed at the center of a minority ($\sim 10\%-15\%$) of galaxies. Due to the extreme conditions characterizing their environment, they represent a unique laboratory for the study of high energy physical processes, which makes them yet among the most studied objects in astrophysics.

As discussed below, a number of effects causes the observational properties of these sources to be highly sensitive to the orientation respect to the observer's line of sight. Although we have today a global understanding of such effects (see Sect. 1.2), the exact knowledge of the intrinsic physical properties and structure of AGN is still missing, and their classification is sometimes ambiguous. In this section I describe the main constituents of an AGN, a simplified version of which is depicted in Fig. 1.1, and I focus on those aspects which are more relevant for this thesis. I start with the two elements which are believed to be present in all AGN and lie at the very center: a supermassive black hole and a rotating accretion disk. Then I introduce the properties of certain clouds of gas and dust rotating at different distances from the central object and affecting, often significantly, the observed spectral energy distributions, both in emission and in absorption. Figure 1.1 also shows a narrow collimated jet, launched from the center in the direction perpendicular to the plane of the rotation. This is actually present in a small fraction of AGN, the class of radio-loud objects, and it is widely described in Sect. 1.3.

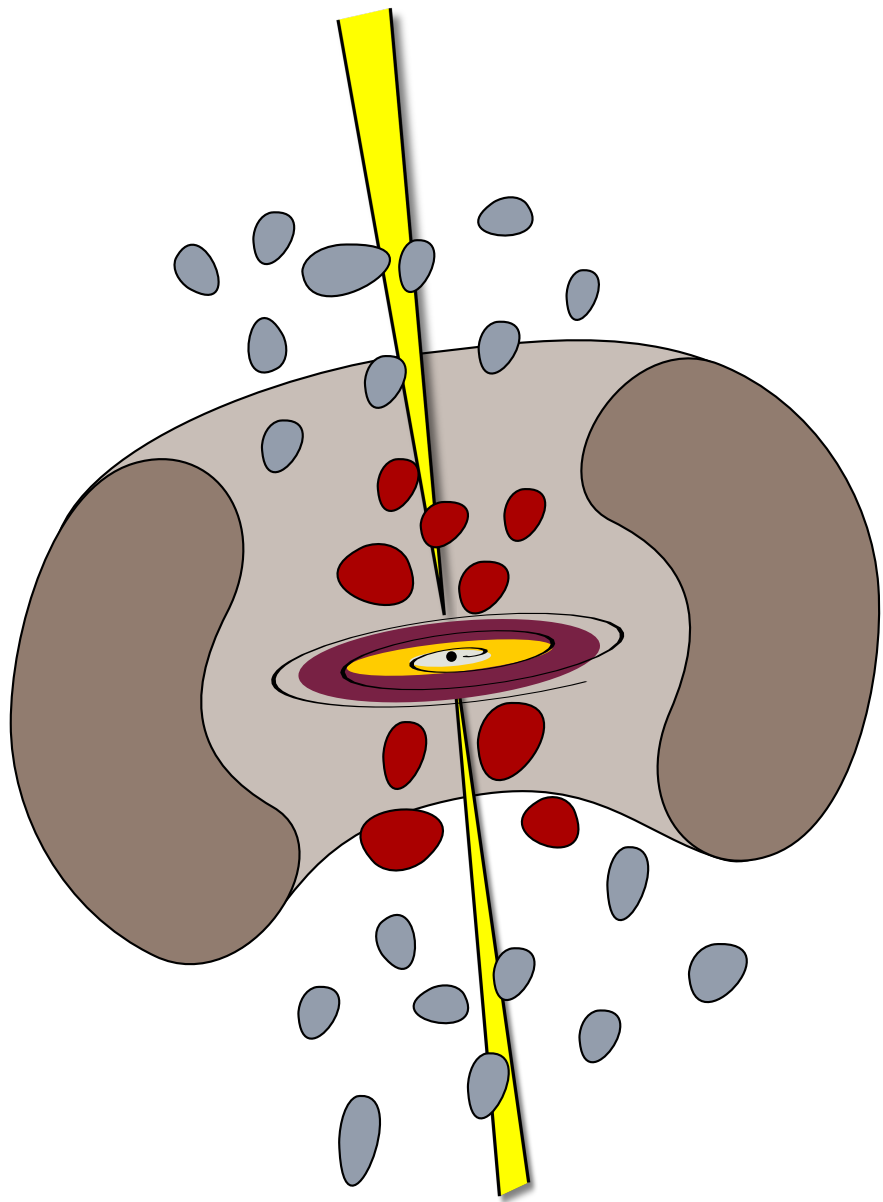


Figure 1.1: Sketch of the main constituents of an Active Galactic Nucleus (AGN). The small black point at the very center is the supermassive black hole, surrounded by the accretion disk (in orange and violet). Clouds of gas are rotating at different distances from the nucleus, producing broad (red clouds) and narrow (light blue clouds) emission lines. A torus of thick material (gray, donut-like structure) can encase the nuclear regions. A jet of relativistic particles (in yellow) is sometimes emitted from the nucleus. Image courtesy of Vassilis Karamanavis ([Karamanavis 2015](#)).

1.1.1 The supermassive black hole

PHYSICAL PROPERTIES

Supermassive black holes (SMBH) at the center of active galaxies feature huge masses of the order of $10^7 - 10^{10}$ solar masses (1 solar mass $M_{\odot} \sim 1.99 \times 10^{30}$ Kg). In the astrophysical context, the mass M_{BH} and the angular momentum J are the only parameters characterizing the space-time surrounding the object. The mass uniquely determines the *Schwarzschild radius* $r_S = 2GM_{\text{BH}}/c^2$ (where G is the gravitational constant and c the speed of light), classically defining a surface called the *event horizon* within which the escape velocity becomes larger than the speed of light. If, however, the black hole is rotating (Kerr black hole) with a spin $\alpha_* = (Jc)/(GM_{\text{BH}}^2)$ comprised between 0 and 1, the event horizon shrinks, and it reaches down to $0.5r_S$ in the case of a maximally spinning black hole ($\alpha_* = 1$). A rotating black hole differs from a static one also because of the presence of a region of elliptical shape called the *ergosphere* (Fig. 1.2) in which the space-time rotates with the black hole with a speed decreasing from the center and reaching zero at the edge. This process is known as *Lense-Thirring effect* or *frame dragging* (Thirring 1918). The fate of a particle entering the ergosphere is not necessarily the disappearance in the event horizon, because the particle can actually gain energy from the rotation and escape. This mechanism of extraction of rotational energy from the black hole is important in the context of jet formation (Chapt. 2).

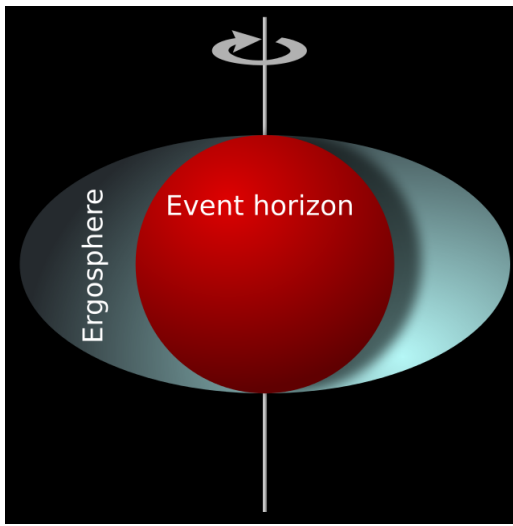


Figure 1.2: Ergosphere and event horizon of a rotating black hole. Credit: Wikipedia.

As a final remark on the physical properties of SMBH, it is worth noting that, quite counter-intuitively, they are not high density objects. If we define the *mean density* ρ as the ratio

between the mass M and the volume $\frac{4}{3}\pi r_S^3$, ρ is of the order of the density of water for a moderate mass of $10^8 M_\odot$, and even lower for higher masses. Thus, unlike in the case of stellar black holes, the conditions of matter forming SMBHs are not extreme.

ARE SMBH REALLY OUT THERE?

The whole AGN paradigm is based on the assumption that a SMBH exists at the center. But how solid is this assumption? After all, nobody has ever seen a black hole, because it is, by definition, invisible. I have already mentioned how variability can constrain the size of the emission, which is a small fraction of a parsec in AGN. But what about the mass? Astronomers have developed several methods for deriving it, and they all agree on the orders of magnitude. The conclusion is that a supermassive black hole is the only object, according to the present knowledge of physics, which can combine such a huge mass and small size. Given the importance of these measurements, I report below the main methods developed for the mass estimate. For a more complete description the reader can refer to [Peterson \(2014\)](#). The direct measurements firstly include dynamical studies, either of the gas or of the stellar populations orbiting the SMBH. The most accurate studies are those considering the motion of individual sources, for example of single stars in the Galactic center (e.g [Eckart et al. 2002](#); [Meyer et al. 2012](#)) or of the megamaser in the galaxy NGC 4258 ([Miyoshi et al. 1995](#)). These are however unique cases, due to the extreme vicinity of the sources. The second best direct measurements are based on statistical dynamical properties of the rotating systems. In a good number of galaxies, the high resolution provided by telescopes like *Hubble* allows to probe scales comparable with the black hole's *radius of influence* R_{BH} , and to infer its mass from the collective motion of the stars using the relation ([Peebles 1972](#)):

$$M_{\text{BH}} = \frac{R_{\text{BH}}\sigma_*^2}{G} \quad (1.1.1)$$

where σ_* is the velocity dispersion of the stars. Gas dynamics can also provide an important direct insight, for example through a method called *reverberation mapping* ([Blandford & McKee 1982](#)). This method exploits the connection between the variability of the continuum emission from the accretion process and the variability of the emission lines produced in the surrounding, fast rotating gas clouds due to the ionizing continuum (Sect. 1.1.3). The measured time delay between the two constrains the distance r of the gas from the central object, and with the additional information on the velocity dispersion of the gas ΔV^2 , as deduced from the lines width, the mass M_{BH} is given by:

$$M_{\text{BH}} = \frac{fr\Delta V^2}{G} \quad (1.1.2)$$

where f is a form factor of order unity encasing the unknown parameters (geometry, kinematics, inclination) of the system (Peterson 2014). The advantage of this technique is that it does not require high angular resolution, but only time resolution, thus it can in principle be applied also at high redshift. As a drawback, however, it is resource-intensive, meaning that a large number of observations is needed. Therefore, many mass estimates rather exploit indirect methods, based on some empirical relations proved to be quite solid. Among others, the M - σ relation (Ferrarese & Merritt 2000)

$$\frac{M_{\text{BH}}}{10^8 M_{\odot}} = 3.1 \left(\frac{\sigma_b}{200 \text{Km} \cdot \text{s}} \right)^4 \quad (1.1.3)$$

is a tight correlation between the stellar velocity dispersion in the bulge, σ_b , of the galaxy and the black hole mass. Its importance also resides in the implications for the formation of galaxies: the black hole mass and the host galaxy co-evolve.

1.1.2 The accretion disk

The accretion disk can be considered as the key constituent of an active nucleus. Indeed, while most galaxies are thought to host a supermassive black hole at their center, only active galaxies, as their name suggests, are characterized by a significant accretion activity. The accretion disk is formed after the infall of gas surrounding the strong gravitational potential of the central object as a consequence of the conservation of angular momentum. In order for matter to move inward, the angular momentum must be transported outward. How exactly this is achieved is not yet clear, but it is likely through stresses involving a combination of gravity, hydrodynamics, viscosity, radiation and magnetic fields. One of the most efficient mechanisms may be the enhancement of the viscosity through the magneto-rotational instability (MRI), a turbulence developing in charged fluids which rotate differentially in a magnetic field (Balbus & Hawley 1991).

The differential rotation of the material forming the disk also gives rise to an intense frictional heating and to copious thermal radiation over a broad electromagnetic spectrum. There is an upper limit to the luminosity which can be reached in this mechanism: if the force generated by the radiation pressure is at some point larger than the gravitational force, the accretion stops. This limit, called Eddington luminosity, is

$$L_{\text{Edd}} = \frac{4\pi G m_p M_{\text{BH}}}{\sigma_T} = 1.26 \times 10^{38} \frac{M_{\text{BH}}}{M_{\odot}} \text{erg/s} \quad (1.1.4)$$

where m_p is the proton mass and σ_T is the Thomson cross-section. If the central object is accreting matter at a rate \dot{M} , then the luminosity L deriving from the accretion can be

expressed as a fraction η of the rest mass energy:

$$L = \eta \dot{M} c^2 \quad (1.1.5)$$

This luminosity, as I said, cannot exceed the Eddington limit, which implies that also the accretion rate is, in principle, limited. By equating the relations 1.1.4 and 1.1.5 we obtain the *Eddington accretion rate*

$$\dot{M}_{\text{Edd}} = \frac{4\pi G m_p M_{\text{BH}}}{\eta c \sigma_T} \quad (1.1.6)$$

The factor η depends on the physical conditions of the disk, and is maximized if the disk is assumed to be optically thick and geometrically thin ([Shakura & Sunyaev 1973](#)). Typically, about 10% of the mass can be converted in AGN ([Soltan 1982](#)), which makes accretion the most efficient mechanism of conversion of rest-mass energy known in nature.

It should be noted, however, that different kind of disks can be characterized by much lower efficiencies. For example, optically thin, geometrically thick disks, e.g. Advection Dominated Accretion Flows ([Begeleman 1979](#); [Narayan & Yi 1994](#)), may radiate very inefficiently. Their study is important for the interpretation of the different ranges of luminosities observed in AGN, including the faint ones. Also, such disks may feature super-Eddington accretion rates. This is especially relevant in the attempt to explain the fast growth of black holes in the early Universe, and much effort has been put lately in their modeling through numerical simulations (e.g. [Sadowski et al. 2014](#)).

In the rest of the section I focus on the classical geometrically thin, optically thick disk for describing the expected temperature profile and spectrum of the emission. It can be assumed that the optically thick disk radiates as a black-body, and by applying the Stefan-Boltzmann law it can be shown that the temperature T depends on the radial distance R from the center as:

$$T(R) = \left(\frac{3GM_{\text{BH}}\dot{M}}{8\pi R^3\sigma} \right)^{1/4} \quad (1.1.7)$$

where σ is the Stefan-Boltzmann constant. The temperatures derived from this formula are in the range $10^4 - 10^6$ K, therefore most of the radiation is emitted in the optical-UV, forming the so-called *blue bump* in the spectra, possibly with some extension to the soft X-rays.

THE HOT CORONA AND THE HARD X-RAY EMISSION

Equation 1.1.7 clearly shows that the maximum reachable temperature in the accretion disk depends strongly on its inner-radius. The accretion disk is indeed truncated at a certain

distance from the black hole. While in Newtonian gravity there exist stable circular orbits at any distance from a point mass, in general relativity this is no longer true. The inner part of the accretion disk experiences the strong-properties of gravity within the radius of the Innermost Stable Circular Orbit (ISCO) and, unless there is an external support by non-gravitational forces (e.g. magnetic field), gas within the ISCO is fated to fall down into the black hole. The ISCO radius r_{ISCO} depends on SMBH's spin and on the kind of orbits, and it varies from the maximum value of $9r_S$ for a maximally spinning black hole ($\alpha_* = 1$) with retrograde orbit to the minimum of $1r_S$ for a maximally spinning Kerr black hole ($\alpha_* = 1$). A very powerful tool for testing the general relativistic effects in the proximity of the ISCO is the iron K α line, emitted at 6.4 keV. This line if thought to be produced as the result of the interaction between material in the accretion disk and a corona of hot plasma ($T \sim 10^6$ K) surrounding it (Haardt & Maraschi 1991). Thermal photons from the accretion disk are up-scattered by electrons in the corona (this is the inverse-Compton scattering, see Sect. 1.3.2), giving rise to a non-thermal power-law component in the hard X-rays. This, in turn, irradiates the accretion disk, being partially absorbed and partially reflected by it. This process gives rise to fluorescent K α lines of the most abundant metals in the innermost regions of the accretion disk, and the iron line is the strongest of them. The iron line profile appears affected by a number of general relativistic effects, such as gravitational redshift, and is extremely sensitive to the ISCO radius. Therefore it is one of the best tools for calculating the spin parameter (Reynolds 2014).

1.1.3 The Broad- and Narrow-line regions

Since the seventies it has been clear that the emission-line spectra in AGN are kinematically composite (Khachikian & Weedman 1974), often showing both narrow and broad components. These are thought to result from the photo-ionization of gas clouds orbiting at different distances from ionizing continuum, i.e the emission from the accretion disk. The narrow components have Doppler widths less than ~ 500 km/s and often comprise forbidden lines, implying that they arise in low-density gas clouds ($n_e \simeq 10^3 \text{ cm}^{-3}$). Such clouds are named the Narrow-Line Regions (NLR). In contrast, the broad components have Doppler widths in the range 1000 to 25000 km/s and arise in gas of high density ($n_e > 10^9 \text{ cm}^{-3}$) at a temperature of $\sim 10^4$ K, the Broad-Line Regions (BLR) (Peterson 2006). The extraordinary Doppler widths of some broad lines and the short time delay between the variability of the continuum and of the lines strongly suggests that the BLR is extremely close to the central engine, likely less than 1 parsec away, and as such it represents a fundamental probe. For instance, the use of the BLR for estimating the black hole mass

was discussed in Sect. 1.1.1. Conversely, the variability time scale of the narrow lines is long, implying that the region is spatially extended and lies at a larger distance from the central engine, in a range from ten to hundreds, or even a thousand parsecs (Netzer 2015). This means that the NLR can be more easily spatially resolved and mapped, for example tracing the prominent [OIII] forbidden line. The most intense lines from the BLR, instead, are usually the hydrogen Lyman alpha, CIV and the semi-forbidden CIII]. Figure 1.3 shows some spectra including these lines obtained from the averaging of a large number of sources in different luminosity/redshift bins (vanden Berk et al. 2004). Interestingly they look very similar, indicating that the physical and chemical properties of the BLR do not evolve strongly with redshift or luminosity.

However, the BLR is not observed in all AGN. While this absence may be intrinsic in some low luminosity AGN, in most of the cases it is thought to be caused by the absorption from a thick torus obscuring the nucleus. Indeed, the broad lines scattered by this material can often be observed in polarized light, as first discovered by Antonucci & Miller (1985).

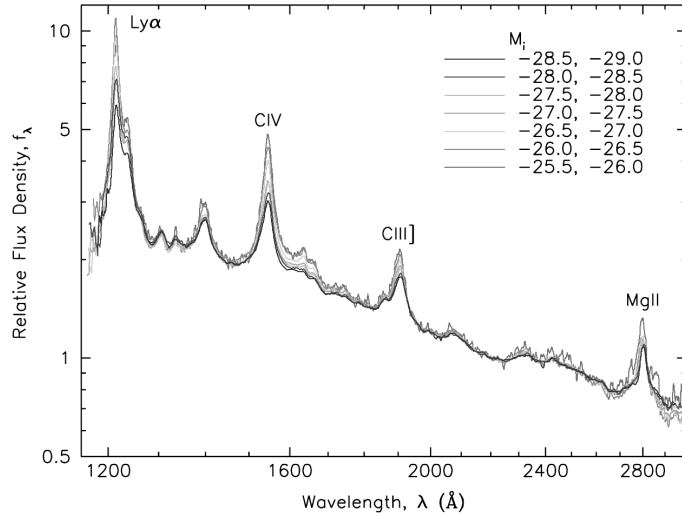


Figure 1.3: Composite spectra of Quasars in different luminosity bins from the Sloan Digital Sky Survey (vanden Berk et al. 2004).

1.1.4 The torus

As mentioned in the previous section, the central regions of some AGN can be obscured due to the presence of a circumnuclear material with the approximate geometry of a torus. The physical and geometrical properties of the clouds forming it can be inferred from various observational signatures. Concerning the composition, the strong extinction implies the

presence of dust, dense enough to be opaque to hard X-rays, which are also missing in the spectrum of the obscured sources. The average column density must be of the order of $\sim 10^{24} \text{ cm}^{-2}$ (Krolik & Begelman 1988). Near and mid-infrared observations confirm the existence of emission associated both with warm and hot dust, in a range of temperatures between $10^2 - 10^3 \text{ K}$ (Edelson & Malkan 1986; Raban et al. 2009). A considerable fraction of the gas, with a mass as high as $10^9 M_\odot$, is thought to be made of molecules, which can survive to the extreme environmental conditions thanks to the screening from the dust. A direct, high resolution imaging of the molecular component has been obtained in the spiral active galaxy NGC 1068 through ALMA observations (García-Burillo et al. 2014), showing the presence of intense emission from high density tracers (high rotational transitions of CO, HNC, HCO+, CS) in the nuclear regions (Fig.1.4). Concerning the geometrical properties of the torus, it is first of all well known that it has a small size. Near and mid-infrared interferometry constrains the radius to be not larger than a few parsecs (Jaffe et al. 2004; Burtscher et al. 2013), compatible with the fact that the emission lines from the NLR do not appear to be affected. Reverberation mapping studies reveal that the inner edge of the torus lies at a distance from the central engine which scales with its luminosity as $L^{0.5}$ (e.g. Suganuma et al. 2006). Indeed, the dust grains are heated by the strong radiation field (at $T \sim 10^4 \text{ K}$) and sublimate at a distance which is typically smaller than $\sim 1 \text{ parsec}$. By

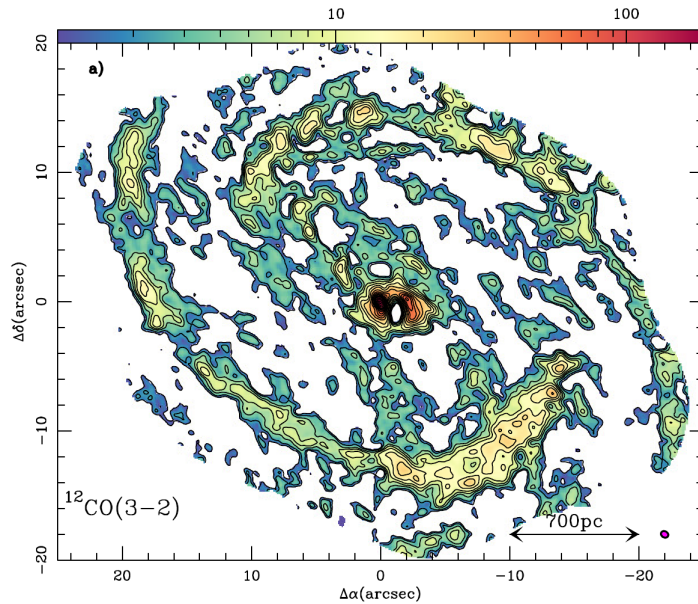


Figure 1.4: Map of the CO (3-2) emission intensity in the spiral active galaxy NGC1068 from ALMA observations at $\sim 350 \text{ GHz}$. Emission from both the galaxy disk and the central gas is detected (García-Burillo et al. 2014).

considering the ratio between the number of AGN with visible BLR and those with obscured BLR, it is deduced that the torus must be geometrically thick, i.e. with an height comparable with the radius. The material is likely not uniformly distributed, but is characterized by a certain degree of clumpiness. The clearest evidence of this comes from the variability and eclipse events of X-ray absorption, recently observed in several AGN ([Markowitz et al. 2014](#)). Also, high random velocities (100km/s) are measured within the torus (e.g. [Tacconi et al. 1994](#)). While in the case of a uniform material they would imply a high thermal temperature and consequent destruction of dust, they can be well understood if the torus is comprised of randomly moving high-density clouds. On the other hand, such a random motion is not only observed but also required for supporting the toroidal structure of the clouds, which would otherwise rapidly settle in a disk configuration. Collisions between the clouds will cause some of them to loose angular momentum and be captured by the black hole, feeding the accretion. In turn, the torus is thought to be continuously replenished by material extended over a much larger scale.

1.2 The AGN zoo and the unified scheme

In the description of the main constituents of an AGN (Sect. 1.1), one important feature of these systems has already emerged: they are spatially asymmetric, matter is mostly distributed in a plane defined by the rotation of the central object. As a consequence, a dependence of the observational properties on the orientation of the system respect to the line of sight of the observer is expected. While this sounds natural today, it has been quite challenging in the past to come up with a simple model which could account for the multiplicity of flavors observed in AGN, and it was not until the nineties, with the works of [Antonucci \(1993\)](#) and [Urry & Padovani \(1995\)](#), that a unification scheme was conceived. Except for the presence or absence of a jet, these models assume that AGN can otherwise differ only in two parameters: the orientation and the luminosity, with the former being the most fundamental. Specifically, depending on the relative orientation of the molecular torus, active nuclei can be classified in:

- **Type 1** - The nucleus is seen face on. Broad lines from the BLR, as well as narrow lines from the NLR are detected. The spectrum is characterized by a strong continuum emission, including hard X-rays.
- **Type 2** - The nucleus is seen edge-on and the molecular torus obscures it, preventing the broad lines and the hard X-rays to be detected. The continuum emission from the central source is reduced, while a strong infrared component from the dust re-emission

arises.

- **Intermediate** - The orientation of the torus is such that the nucleus is only partially obscured. The observational properties are intermediate between type 1 and type 2.

The second parameter, the luminosity, further divides the (radio-quiet) AGN in two, not well-separated classes:

- **Seyferts** - Low redshift sources in which the host galaxy, usually a spiral, is often visible besides the active nucleus.
- **Quasi Stellar Objects (QSOs)** - Higher redshift sources whose emission is completely dominated by the accretion process, outshining the host galaxy. They can be extremely luminous and found at very high redshift. The most distant QSO currently known is at redshift 7.1 ([Mortlock et al. 2011](#)).

This simple scheme holds in most of the cases. Nevertheless, AGN are complex systems, and objects which are intrinsically different may exist. For example, some sources, named “true type 2” are thought to actually miss a BLR (e.g. [Bianchi et al. 2012](#)). Also, in a number of low power sources there is no clear evidence for the presence of a torus (e.g. [Chiaberge et al. 1999](#); [Panessa & Bassani 2002](#)).

In the original papers presenting the unification scheme ([Antonucci 1993](#); [Urry & Padovani 1995](#)), the radio-loud AGN, i.e. those featuring a relativistic jet, are also discussed. Radio-loud AGN do not appear to differ substantially from the radio-quiet ones in any of the fundamental building blocks described in Sect. 1, and the aforementioned distinction in Type 1 and 2s, as well as in luminosity classes, may apply in a similar way. However, the presence of a jet affects, often dramatically, the observed emission, leading to consider these objects as forming a very different class. As already anticipated in previous works ([Blandford & Königl 1979](#); [Barthel 1989](#)), the orientation, in this case not only of the torus but especially of the jet, plays again a fundamental role. In the next session, the orientation-dependent effects related to the physics of relativistic jets will be deeply discussed. Here, I report the definition of the main classes of radio-loud AGN as defined in the classical scheme.

- **Radio galaxies** - Radio-loud AGN with a jet oriented close to the plane of the sky and diffuse, bright radio emission from kilo-parsecs up to mega-parsecs scales. Depending on their luminosity in the radio band at 1.4 GHz ([Fanaroff & Riley 1974](#)) they are further divided into:

- **Fanaroff-Riley type I (FRI)**. Their luminosities are below 10^{41} erg/s and they exhibit extended, edge darkened twin lobe structures connected to the center by not well collimated, often double-sided jets.
- **Fanaroff-Riley type II (FRII)**. Their luminosities are above 10^{41} erg/s, and they present edge-brightened lobes with bright knots of emission (hot-spots) at their outer extremities. Their jets are highly collimated and often appear one-sided.
- **Blazars** - Radio-loud AGN with a jet oriented close to the line of sight of the observer, which cause the emission to be strongly affected by relativistic effects. They are characterized by a high core dominance, meaning that the parsec scale radio emission accounts for most of the total flux, by a strong variability and high degree of polarization. They are further divided based on the spectral properties, and ultimately on the luminosity, in:
 - **BLLac objects** - Generally lower power and lower redshift Blazars characterized by weak broad emission lines with equivalent widths $< 5\text{\AA}$ ([Stickel et al. 1991](#)).
 - **Flat Spectrum Radio Quasars (FSRQs)** - Generally higher power and higher redshift Blazars showing broad emission lines.

In the simple unification scheme, Radio galaxies and Blazars are not different objects, but are simply one the “rotated version” of the other. Specifically, FRI and BLLac objects form the low-power parent populations, while FRII and FSRQs represent different manifestations of the high-power radio-loud populations.

1.3 Relativistic Jets

Jets are collimated outflows of plasma and magnetic field, ejected from a variety of astronomical objects, namely Young Stellar Objects (YSOs), X-ray binaries, Active Nuclei and Gamma-ray bursts. They span many order of magnitudes, both in the energy domain and in linear scale. In AGN, jets are believed to propagate at relativistic speeds with bulk Lorentz factors of the order of tens ([Lister et al. 2013](#)) and jet power typically comprised between $10^{43} - 10^{48}$ erg/s ([Ghisellini et al. 2014](#)), up to kpc and sometimes Mpc scales ([Mack et al. 1997](#)). Their knowledge is largely based on interferometric observations in the radio band, capable of providing high resolution imaging down to sub-parsec scales (Fig. 1.5) thanks to the Very Long Baseline Interferometry (VLBI) technique (Chapt. 3). The high-resolution imaging best reveals the extreme nature of relativistic jets, emblems

of which are, for example, the extra-ordinary compactness of the emission or the “faster-than-light” motions, often observed on parsec scales. On larger scales, the jets terminate in large structures of diffuse and bright radio emission known as the radio lobes (Fig. 1.6).

Below, I firstly explain the main effects which makes relativistic jets so peculiar. Then I describe the principal emission mechanisms and the characteristics of the observed spectra in different classes of sources. Apart from the specific references reported in the text, I also refer to the textbooks by [Hughes \(1991\)](#) and [Robson \(1996\)](#).

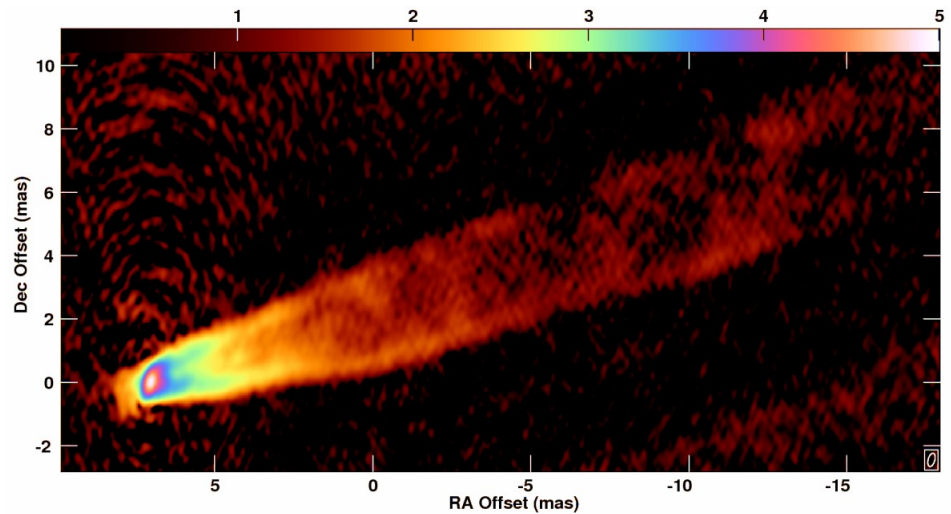


Figure 1.5: Radio image of the parsec scale jet in M87 from VLBI observations at 43 GHz (<http://www.aoc.nrao.edu/cwalker/M87/>).

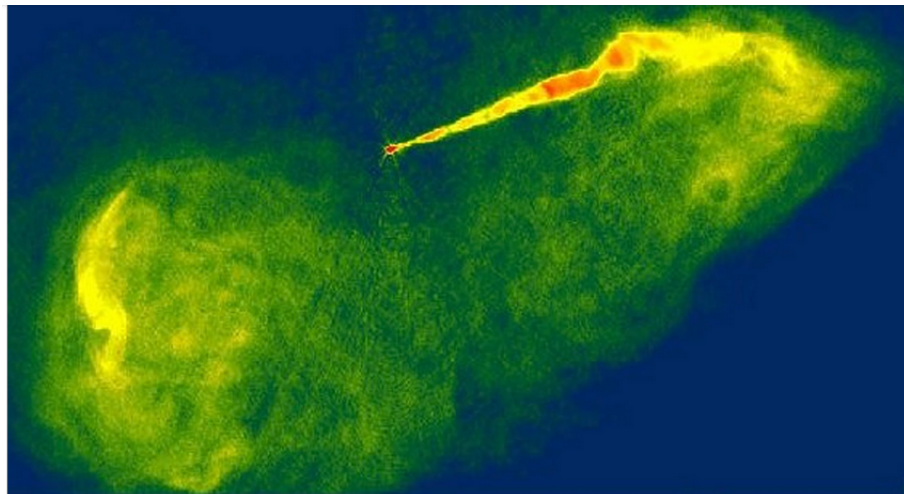


Figure 1.6: Radio image of the kilo-parsec scale jet in M87 from VLA observations in C band. (Credit - National Radio Astronomy Observatory/National Science Foundation).

1.3.1 Relativistic and geometrical effects

SUPERLUMINAL MOTION

The first observational evidence for an apparently faster-than-light motion came in 1969 from VLBI observations of the blazar 3C 273 ([Gubbay et al. 1969](#)). The phenomenon of superluminal motion, already predicted in 1966 by Martin Rees ([Rees 1966](#)), does not contradict special relativity and can be easily explained by examining the geometry of the system. Although relativistic speeds are required, superluminal motion is not strictly a relativistic effect, because no Lorentz transformations are involved. Consider a stationary feature in the jet, named the core (Sect. 1.3.3), emitting a photon at time t_a in position A (Fig. 1 - left). Simultaneously, a blob of matter is ejected in A with speed v in a direction forming an angle θ with the line of sight of the observer. At a time $t_b = t_a + \Delta t$, the photon emitted from the core is at position D, while the blob is in position B and emits a photon. The observer will not receive the two photons at the same time, because the one coming from the blob has to travel an additional distance equal to:

$$CD = AD - AC = c\Delta t - v\Delta t \cos \theta.$$

Therefore, the difference between the arrival times of the photons measured by the observer is:

$$\Delta t_{\text{obs}} = CD/c.$$

Also, the distance between the blob and the core appears contracted to the observer due to projection, and can be written as:

$$BC = v\Delta t \sin \theta.$$

As a result, the measured velocity of the blob is:

$$v_{\text{obs}} = \frac{BC}{\Delta t_{\text{obs}}} = \frac{v\Delta t \sin \theta}{(c\Delta t - v\Delta t \cos \theta)/c}$$

which, by setting $\beta = v/c$, is equivalent to

$$\beta_{\text{app}} = \frac{\beta \sin \theta}{1 - \beta \cos \theta}$$

The previous expression implies that, for small viewing angles and large intrinsic speeds, β_{app} can be much larger than 1 (Fig. 1 - right). To date, apparent speeds as large as $\sim 50c$ have been measured in extragalactic jets ([Lister et al. 2009](#)).

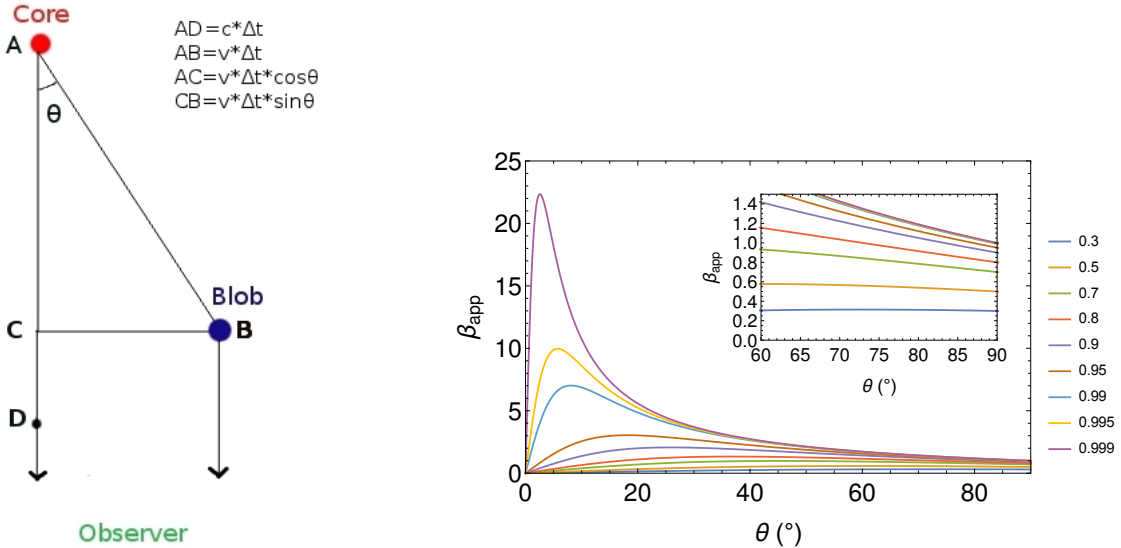


Figure 1.7: **Left** - Geometry of the superluminal motion. **Right** - Apparent beta versus viewing angle for different values of the intrinsic speed. The inset zooms into the large θ interval, in which the observed speed are in general close to the intrinsic ones. However, superluminal motion can in principle be observed in jets seen at any $\theta < 90^\circ$ for $\beta \sim 1$.

RELATIVISTIC DOPPLER BEAMING

In Section 1.1.2, I have briefly discussed the energetic processes taking place in the accretion disk of an AGN. In radio-loud sources, additional power is carried by the jet in different forms, mainly radiation, bulk motion and magnetic field. The jet radiation power can be, depending on the physical condition, intrinsically large. However, in most radio-loud AGN the intrinsic radiation power is only a tiny fraction, often one part per $10^4 - 10^5$, of the observed one due to relativistic effects. The *relativistic beaming* is maybe the most striking feature of relativistic jets. The observed luminosity is increased, as a result of the superposition of different relativistic effects, by a factor δ^4 , where

$$\delta = \frac{1}{\Gamma(1 - \beta \cos \theta)} \quad (1.3.1)$$

is known as *relativistic Doppler factor*. The demonstration of this relation requires a formal application of the Lorentz transformations. However, the different contributions can be easily evaluated from a qualitative point of view. The luminosity is energy per unit time. The energy depends on the frequency of the emission which, as in classical physics, is blue-shifted or red-shifted when the emitting material is approaching or receding from the observer, respectively. The observed and intrinsic frequencies ν_o and ν_e are related by the Doppler factor as $\nu_o = \nu_e \delta$, therefore the observed energy is increased by a factor δ .

Analogously to the super-luminal motion, the fact that the source is moving relativistically and catches up with its own radiation affects the time dt_o between the arrival of two photons as perceived from the observer, which differs from the intrinsic time dt_e by a factor $1/\delta$. Therefore the energy is increased by a factor δ^2 at this point. An additional δ^2 factor comes as an effect of *relativistic aberration*, due to which the radiation from a moving object, isotropic in the rest frame, is focused into a cone of semi-angle $\phi = 1/\Gamma$ in the observer's frame. If one is dealing with mono-chromatic quantities, the dependence of the frequency on δ cancels out and the multiplication factor is diminished to δ^3 . In practice, the observable monochromatic quantity is the *flux density* S_ν , i.e. the spectral radiance integrated over the source solid angle. As I will discuss in Sect. 1.3.2, the flux density observed in jets has a power law dependence on frequency, thus $S_\nu \propto \nu^\alpha$ with α being the spectral index. Since the observed and intrinsic flux densities S_o and S_e correspond to different frequencies, the transformation from one to the other needs to take into account the frequency shift. This can be done by introducing the dependence on the spectral index, as:

$$S_o = S_e^{(3-\alpha)} \quad (1.3.2)$$

For a jet showing a smooth emission, i.e. non “blobby”, [Scheuer & Readhead \(1979\)](#) have suggested that a power of $(2 - \alpha)$ may be more appropriate in 1.3.2.

Equation 1.4.1 and Figure 1.7 immediately show that the Doppler beaming is stronger for small viewing angles and large β , with δ diverging to infinity for $\theta = 0$ and $\beta = 1$. By recalling the classification given in Sect. 1.2, it is clear that the class of blazars will be the most strongly affected by it. Indeed, if one considers the entire radio-loud AGN class, it can be noted that most of the sources have a jet oriented at a small angle, which is simply a selection effect deriving from the beaming. In other words, jets oriented at larger angles are much dimmer and difficult to detect. This is also the reason why the radio galaxies population mainly comprises low redshift sources. Another important consequence of the beaming is the jet *sidedness*. It is believed that all jets are intrinsically two-sided, but relativistic effects usually allow to detect only the approaching side. The strong beaming of the approaching jet and de-beaming of the counter-jet results in a huge ratio R between their observed flux densities, which is derived to be:

$$R = \left(\frac{1 + \beta \cos \theta}{1 - \beta \cos \theta} \right)^{(3-\alpha)} \quad (1.3.3)$$

Again, the power index is reduced to $(2 - \alpha)$ in the case of continuous emission. The jet to counter-jet ratio can be measured from observations, allowing to constrain the intrinsic

parameters β and θ . As a final remark, it should be noticed that if θ or β are sufficiently large, the de-beaming can concern not only the receding side, but also the approaching one (Fig. 1.7). As a consequence, radio galaxies with energetic jets oriented close to the plane of the sky are usually more difficult to observe.

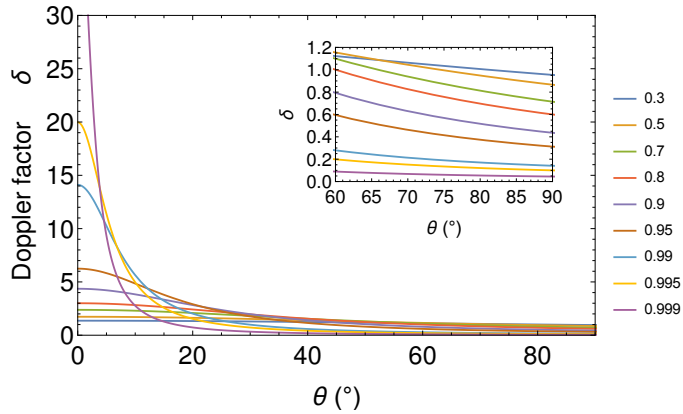


Figure 1.8: Doppler factor δ as a function of viewing angle θ for different values of intrinsic speed β . The inset zooms into the large θ range, in order to better show that the de-beaming can affect also the approaching jet.

1.3.2 Radiation processes

Relativistic jets emit over the whole electromagnetic spectrum, from the radio to X-rays and often γ -rays. The bulk of the radiation is produced through high-energy non-thermal processes, in a context involving relativistic particles immersed in strong photon fields and magnetic fields. The non-thermal nature of the emission is firstly indicated by the high measured values of *brightness temperature* T_B , as derived from the Rayleigh-Jeans law:

$$T_B = \frac{I_\nu c^2}{2k\nu^2} \quad (1.3.4)$$

The intensities I_ν observed from jets would imply exceedingly high physical temperatures if the nature of the emission was actually thermal. Although deprived of its classical physical meaning, the concept of brightness temperature is widely used in the description of non-thermal processes and in the study of jets in particular, as it represents a valid indicator for the energy content and compactness of the sources. Observational evidence indicates that synchrotron and inverse Compton are the main emission mechanisms at play in jets. In the following I introduce the basics of the theories.

SYNCHROTRON RADIATION

The *synchrotron radiation* is emitted as a consequence of the radial acceleration experienced by a relativistic particle. In the astrophysical context, this condition is met in various objects due to the presence of a magnetic field \mathbf{B} causing the particles to follow helical trajectories along the field direction. The magnetic force only affects the direction of v_{\perp} , the component of the particle speed perpendicular to it, inducing a uniform circular motion. The radiation is emitted at a characteristic frequency

$$\nu_s = (\gamma^2 B e) / (2\pi m c) \quad (1.3.5)$$

with m and e being the mass and the charge of the electron respectively, and γ its Lorentz factor. This differs from the non-relativistic gyro-frequency by a factor γ^2 . While in the low energy case the emitted radiation has a dipole pattern, in the relativistic case it is beamed in a cone of semi-opening angle $1/\gamma$ centered along the instantaneous direction of motion. The power radiated P_s (or, equivalently, the energy lost dE/dt) in this process by a single electron depends on the *pitch angle* $\psi = \cos^{-1}(v_{\parallel}/v)$, i.e. on the angle between the direction of the motion and that of the magnetic field, and is given by

$$P_s = - \left(\frac{dE}{dt} \right) = 2\sigma_{TC} \sin^2 \psi \beta^2 \gamma^2 u_B \quad (1.3.6)$$

where u_B is the energy density of the magnetic field and $\beta = v/c$ is the electron speed in units of c . The average power is obtained by averaging over all the pitch angles, which yields $\sin^2 \psi = 2/3$. By remembering that $\gamma \propto E$ and $u_B \propto B^2$, we note that $P_e = dE/dt \propto B^2 E^2$. In order to describe the emission from an ensemble of electrons immersed in a uniform magnetic field, it is now necessary to assume certain distributions of pitch angles and energy. The first is plausibly isotropic, while the second is constrained from observations to be a power law. Thus the number of particles per energy range is $N(E)dE \propto E^{-s}dE$, where s is the index of the power law distribution. If the emission is *optically thin*, i.e all the energy lost by the electrons per unit time corresponds to emission of photons, the intensity of emission $I(\nu)d\nu$ can be written as

$$I(\nu)d\nu \propto E^{-s}dE \frac{dE}{dt} \propto \nu^{(1-s)/2} d\nu \quad (1.3.7)$$

By introducing the *spectral index* α of the radiation spectrum, which is also a power law, the intensity of emission can otherwise be written as $I(\nu)d\nu \propto \nu^{\alpha}$, and it is thus inferred that $\alpha = (1-s)/2$. In astrophysical sources, the typical spectral index of optically thin synchrotron emission is observed to be -0.7 , implying the existence of an acceleration

mechanism, e.g. *Fermi acceleration*, causing electrons populations to have power-law energy spectra with index $s \sim 2.5$. Let us now consider the *optically thick* regime, in which the emitted photons do not have sufficient energy for escaping the electron field and are self-absorbed. The absorption cross-section is larger at longer wavelengths, therefore the very long wavelength emission can only be detected if coming from the surface of the source, while deeper and deeper layers become visible at shorter wavelengths, until the mean free path becomes comparable with the source size. The frequency at which this happens, and the optically thin regime takes over, is called *turnover frequency* ν_n . The spectral index of the thick emission assumes the fixed value of +2.5, equivalent to the Planck spectrum. Indeed, although the electrons have a non-Maxwellian energy distribution, in such conditions they cannot emit radiation more effectively than a black body. Therefore, as in the thermal case, an energy-dependent effective temperature T_{eff} can be associated. In the ultra-relativistic case this is $T_{\text{eff}} = E/3k = (\gamma mc^2)/3k$. By replacing the energy with the frequency from equation 1.4.2 it is found:

$$T_{\text{eff}} \simeq \left(\frac{2\pi mc\nu}{eB} \right)^{\frac{1}{2}} \frac{mc^2}{3k} \simeq 1.18 \times 10^6 \left(\frac{\nu}{\text{Hertz}} \right)^{\frac{1}{2}} \left(\frac{B}{\text{Gauss}} \right)^{-\frac{1}{2}} \quad (1.3.8)$$

In the optically thick regime, T_{eff} represents an upper limit for the brightness temperature T_B , and it is equaled by this at the turnover frequency. In practical applications, the observation of the turnover frequency and of the brightness temperature allows to estimate the magnetic field strength by equating the expressions for T_{eff} and T_B :

$$\left(\frac{B}{\text{Gauss}} \right) \simeq 1.4 \times 10^{12} \left(\frac{\nu_n}{\text{Hertz}} \right) \left(\frac{T_B}{\text{K}} \right)^{-2} \quad (1.3.9)$$

The turnover frequency and the brightness temperature are in turn related by another useful expression, applicable if the angular size Ω of the source is known:

$$\nu_n = \frac{c}{\Omega} \left(\frac{2S_n}{kT_B\pi(1+z)} \right)^{0.5} \quad (1.3.10)$$

where S_n the flux density at ν_n , z the redshift.

As a final remark about the synchrotron radiation, it should be noted that it is characterized by a high degree of linear polarization. By considering the power parallel P_{\parallel} and perpendicular P_{\perp} to the projected direction of the magnetic field, the frequency-dependent fractional linear polarization

$$\pi_L = \frac{P_{\perp} - P_{\parallel}}{P_{\perp} + P_{\parallel}} \quad (1.3.11)$$

turns out to be 0.75 for a single electron and 0.7 for an ensemble of electrons. These are theoretical values, while in practice and for a number of reasons (e.g. instrumental effects, randomness of the magnetic field) much lower degrees are usually observed.

INVERSE COMPTON

Another relevant emission mechanism in the case of relativistic jets is the *inverse Compton scattering*. This process involves the interaction between a relativistic electron and a photon, with the up-scattering of the latter to higher energies. The inverse Compton effect can be somewhat regarded as specular to the synchrotron: the latter involves the scattering of a magnetic field and the former the scattering of a photon field. Indeed, the equations describing the two mechanisms have exactly the same form. The energy loss suffered by a single electron is written:

$$P_{\text{IC}} = - \left(\frac{dE}{dt} \right) = \frac{4}{3} \sigma_{\text{TC}} \beta^2 \gamma^2 U_{\text{rad}} \quad (1.3.12)$$

where U_{rad} is this time the energy density of the photon field. Note the analogy with equation 1.3.6. The photon number density is conserved in the scattering, only the energies are boosted by a factor γ^2 . The spectral shape then depends solely on the energy distribution of the electrons. If it is a power law with index d , the inverse Compton spectrum is a power-law as well with spectral index $\alpha = (1 - d)/2$. In relativistic jets, the seeds photons for the inverse Compton can be the synchrotron photons, up-scattered by the very electron population that produced them. This process, known as *synchrotron self-Compton*, critically limits the temperature that a self-absorbed synchrotron source can reach. At some point, the electron and photon energy densities become sufficiently large for the onset of the so-called *Compton catastrophe*, i.e. synchrotron self-Compton which cools down the system and limits the electron temperature to $\sim 10^{12}$ K ([Kellermann & Pauliny-Toth 1969](#)).

1.3.3 The spectral energy distribution and the VLBI core

According to the unification scheme, blazars and radio galaxies are substantially the same objects seen from different perspectives. However, because of the effects described in Sect. 1.3.1, jets from radio galaxies generally appear slower and much dimmer than those from blazars. Another difference between the two classes of jets is in their observed Spectral Energy Distributions (SEDs). It is believed that the same emission mechanisms, synchrotron and IC scattering, are taking place in all jets, the former generating photons in the radio band and often extending up to optical frequencies, and the latter producing the high energy

emission, sometimes up to TeV energies. Nevertheless, the different orientation of the jets also gives rise to different kinds of spectra. First of all, very high energy photons are more often detected in blazars than in radio galaxies. This is likely because they originate in the inner, compact sections of the jet, which are indeed the dominant contribution in blazars. Moreover, the synchrotron component appear remarkably different in the two classes. In order to understand this, it is firstly necessary to distinguish between the jet emission on parsec scale and the large scale emission associated with the radio lobes. The lobes mark the locations were the jets finally impinges into the medium and dissipate their huge kinetic energy, giving rise to shocks, acceleration of particles and ultimately copious synchrotron radiation. In the radio band, especially at low frequencies, the lobes are by far the brightest component in the source frame. However, material forming the lobes is slow, and the emission is not beamed. On the contrary, the parsec scale emission originates in a relativistic flow, and thus is beamed. By remembering how dramatic the beaming effect can be at small viewing angles (Sect. 1.3.1), it is then easy to understand that the observed emission in blazars will be dominated by the parsec-scale component, while in radio galaxies the lobes will be decidedly more prominent. This difference in the contributions to the synchrotron emission also reflects in a different shape of the observed synchrotron spectra for the two classes. Unlike in radio galaxies, the spectral index of the synchrotron emission in blazars is in general flat, contrary to the expectations for jets in thin regime. How does the flat spectrum of blazars come about?

According to the most favored theory ([Marscher 1996](#)), the flat spectrum results from the superposition of different synchrotron self-absorbed components. In a jet pointing towards the observer, the brightest feature, known in the jargon as the *VLBI core* ([Blandford & Königl 1979](#)), is located at the very base of the, assumed conical, jet. In its extension, the VLBI core is characterized by a gradient of magnetic field and electron density which makes it a “mixed” feature: optically thick in the narrower regions closer to the central engine and optically thin on the outer and wider surface. Each surface forming the core becomes thin at a different turnover frequency, increasing with decreasing distance from the black hole. As a result, the overall spectrum of the core region appears flat (Fig. 1.9). The weakness of this model may be that it requires a certain “fine tuning” of the physical conditions at the base of the jet, for example that the magnetic field strength decreases with distance from the origin z as z^{-1} .

In Figures 1.10 and 1.11 I compare the SEDs of two sources, the radio galaxy 3C 079 and the blazar BLLAC, clearly showing the aforementioned differences. Note that the SED of BLLAC extends to much higher frequencies.

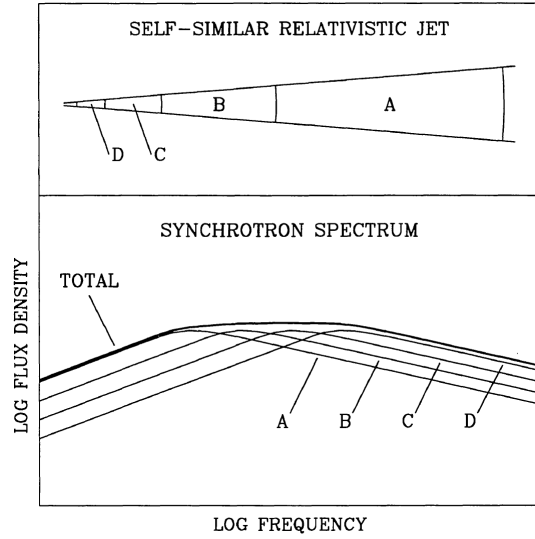


Figure 1.9: Formation of the flat spectrum at the base of the jet ([Marscher 1996](#)).

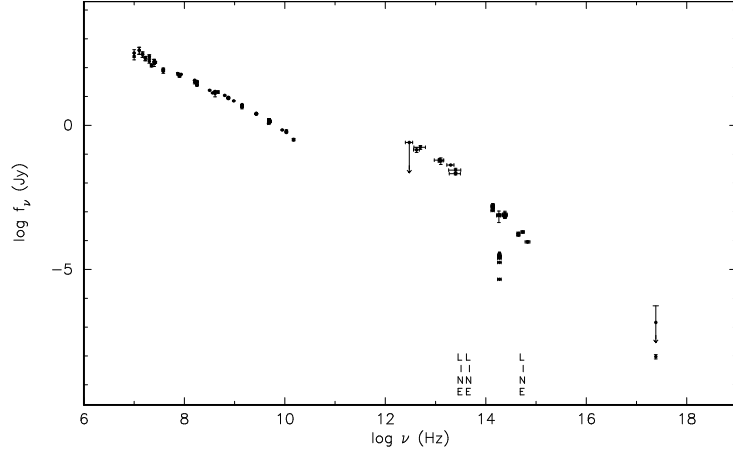


Figure 1.10: Spectral energy distribution of the radio galaxy 3C079 (Credit - NASA/IPAC Extragalactic Database).

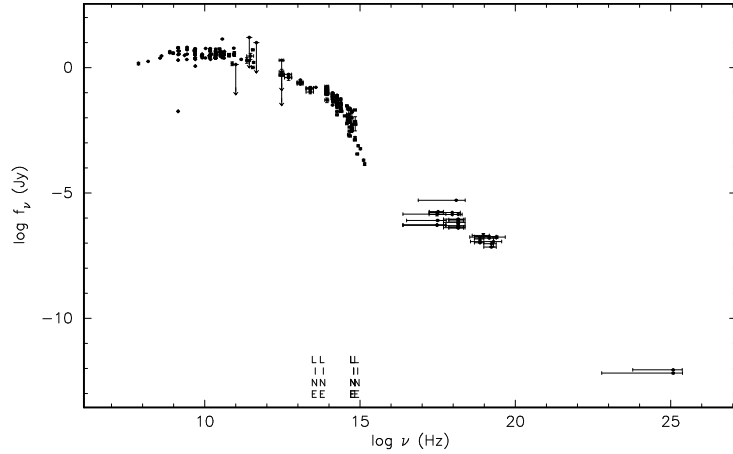


Figure 1.11: Spectral energy distribution of the blazar BLLAC (Credit - NASA/IPAC Extragalactic Database).

Chapter 2

The formation of relativistic jets

The understanding of relativistic jets has significantly advanced in the past decades. By interpreting jets as fluid phenomena, their properties on parsec and kilo-parsec scales are quite well explained by applying the laws of relativistic hydrodynamics. However, a fundamental problem is still unsolved: how can jets be accelerated up to Lorentz factors of tens, and how can they be so sharply collimated? The answer to these questions must be intimately related to the mechanism of jet launching. The physical description of the extreme environment in the surroundings of supermassive black holes and accretion disks is very challenging, and requires a full GRMHD (General Relativistic Magneto-Hydro-Dynamic) formalism. Big steps forward have been done over the past 20 years since the development of numerical simulations, through which different theories are tested, with continuously increasing degree of complexity, in order to reproduce the observed properties of jets on various scales. On the other side, VLBI observations at millimeter wavelengths (Chapter 3) are today able to probe scales which are comparable to the Schwarzschild radius in the most nearby sources, and are decisive for discriminating between different scenari.

Since jets are made of relativistic plasma, this chapter starts with the introduction of some basic notions of plasma physics necessary for understanding the following sections. I then proceed by outlining the fundamental ideas which are at the base of the current paradigm for jet formation, acceleration and collimation, supporting the discussion with state of the art observational results. Besides the specific references reported in the text, I refer to the textbooks by [Chiuderi & Velli \(2012\)](#); [Böttcher et al. \(2012\)](#); [Contopoulos et al. \(2015\)](#) and to the review by [Spruit \(2010\)](#).

2.1 Relativistic plasmas

2.1.1 Fundamental parameters

A plasma is an ensemble of charged particles and of the electromagnetic fields generated by them. Being the dynamics of the system dominated by the fields, plasmas possess very peculiar properties compared to the three ordinary states of matter (solid, liquid, gaseous), and can therefore be considered as the fourth state. This is indeed the most common state in the Universe, as it constitutes nearly 95% of the total baryonic matter. Relativistic jets are a spectacular manifestation of matter in the plasma state. In the following, some fundamental parameters for plasma physics are introduced.

A plasma can be considered quasi-neutral on scales comparable to the *Debye length* λ_D .

$$\lambda_D = \sqrt{\frac{kT}{4\pi e^2 n}} \quad (2.1.1)$$

where k is the Boltzman constant, T is the temperature, e is the proton (electron) charge and n is the particle number density. Within a sphere of radius λ_D , the electric screening is high enough that the net charge $Q(\lambda_D)$ becomes small. If the particle distribution is slightly perturbed, particles react to the local violation of charge neutrality with an harmonic motion of frequency ω_p , named *plasma frequency*. This quantity can be derived dimensionally as:

$$\omega_p = \frac{1}{\tau_p} = \frac{v_T}{\lambda_D} = \sqrt{\frac{4\pi e^2 n}{m}} \quad (2.1.2)$$

where $\tau_p = \lambda_D/v_T$ is the characteristic time, $v_T = \sqrt{3kT/m}$ is the (thermal) characteristic speed and m is the mass of the particles. The Debye length and the plasma frequency set the fundamental scales for the collective behavior of a plasma, meaning that, on these scales, the single particles composing the plasma do not play a relevant role, and the dynamics of the system is only determined by the long-range term of the electric potential.

2.1.2 Fundamental relativistic MHD equations

Since the Debye length is usually very small and the plasma frequency is very large, plasmas can, in general, be conveniently treated as neutral fluids with null electric fields. This is the approach of magnetohydrodynamics (MHD). This approximation is valid as long as the timescale for electromagnetic phenomena is of the same order as the timescale for hydrodynamic phenomena. In the MHD regime, a kinetic description of the system, i.e.

concerning the trajectories and the velocity distributions of the particles, is of course not possible. On the other hand, the knowledge of the global parameter of the fluid (density, temperature, velocity) is sufficient in most of the problems. In the framework of relativistic jets physics, MHD equations are usually simplified by assuming that the fluid is in steady-state, i.e. there is no time dependence, and that it is cold, meaning that thermal effects can be neglected. Under these conditions, the first two fundamental equations describing the system are the relativistic continuity equation and momentum conservation, respectively:

$$(\mathbf{v} \cdot \nabla)(\Gamma\rho) + \Gamma\rho\nabla \cdot \mathbf{v} = 0 \quad (2.1.3)$$

$$\Gamma\rho(\mathbf{v} \cdot \nabla)(\Gamma\mathbf{v}) = \frac{1}{c}(j^0\mathbf{E} + \mathbf{j} \times \mathbf{B}) \quad (2.1.4)$$

where \mathbf{v} is the velocity vector, ρ is the rest mass density, Γ is the Lorentz factor, j^0 is the charge density, \mathbf{j} is the current density, \mathbf{E} and \mathbf{B} are the electric and magnetic field respectively. The system is completely described when adding the Maxwell's equations and the equation of state. In the case of ultra-relativistic fluids, the equation of state can be expressed as $P \propto \rho^{\frac{4}{3}}$, with P being the pressure.

Ideal MHD is based on the further simplification that the fluid has an infinite conductivity, $\sigma \rightarrow \infty$, thus the electric field in the fluid frame vanishes. The Alfvén theorem demonstrates that, in such conditions, the magnetic field configuration is tightly bound to the evolution of the fluid speed. This is expressed formally by the *flux freezing* equation:

$$\mathbf{E} = -\frac{1}{c}\mathbf{v} \times \mathbf{B} \quad (2.1.5)$$

The presence of magnetic fields introduces qualitative changes in the dynamics of plasmas compared to purely hydrodynamic fluids. Next to the isotropic thermal pressure, an anisotropic term associated with the electromagnetic field, capable of moving the plasma or guiding the plasma motions, arises. The Lorentz force $\mathbf{j} \times \mathbf{B}$ provides the link between the fluid equations and the fundamental properties of electromagnetism. It can also be written as:

$$\mathbf{j} \times \mathbf{B} = \mathbf{i}_n \frac{1}{R_c} \frac{B^2}{4\pi} + \mathbf{i}_t \frac{d}{ds} \left(\frac{B^2}{8\pi} \right) - \nabla \left(\frac{B^2}{8\pi} \right) \quad (2.1.6)$$

where \mathbf{i}_n and R_c define the curvature of the magnetic field line (the first is the unit vector pointing towards the center of curvature, the second is the radius of curvature), s is the distance along the magnetic field line and \mathbf{i}_t is the unit vector tangent to the line. This equation expresses the Lorentz force as the difference between two magnetic pressure gradients. The first, represented by the first two terms, is called *magnetic tension*. It

appears only when magnetic field lines are curved and it acts in the direction parallel to B by straightening them. The last term is the gradient of what is commonly known as *magnetic pressure*, and it arises isotropically whenever the intensity of the B field changes with position. Equilibrium is achieved when there is a balance between magnetic pressure and tension.

2.1.3 MHD waves

Another qualitative difference between simple fluid dynamics and magnetohydrodynamics is that the magnetic field is elastic, and can support magnetic waves, arising as a consequence of perturbations of either the pressure or the magnetic field. The *Alfvén wave* transports magnetic perturbations by keeping the total pressure constant. It is transmitted along the magnetic field lines through oscillations of the ions. In relativistic regime, the Alfvén speed is

$$c_a^2 = c^2 \frac{B^2}{B^2 + 4\pi w} \quad (2.1.7)$$

where $w = \rho c^2 + p\gamma/(\gamma - 1)$ is the relativistic enthalpy, and γ is the ratio of specific heats. The formula clearly shows that, in the presence of intense magnetic fields or of small densities, the Alfvén speed approaches the speed of light. If the perturbation concerns the total pressure, another kind of wave, called *magnetosonic wave* arises. Depending on its speed, this is classified as *fast* or *slow*. A fast magnetosonic wave has a speed exceeding the Alfvén speed and the sound speed ($a_s^2 = c^2\gamma(p/w)$), therefore it can propagate in any direction. In its transmission, the gas pressure and the magnetic pressure are modified in the same way, i.e. they are both either increased or decreased. The slow magnetosonic wave has a lower speed compared to the Alfvén and the sound speed, and it mostly propagates along the magnetic field lines. In its transmission, the gas pressure and the magnetic pressure are modified in the opposite way.

2.1.4 Resistive MHD

The flux freezing condition in ideal MHD has important consequences both on the energetics and on the dynamics of the plasma. The impossibility for the topology of the magnetic field to re-arrange itself leads to an accumulation of magnetic energy. When the assumption of perfect conductivity is relaxed, this energy can be dissipated. In collisionless plasma, like those forming jets, the dissipation is caused by the collective interaction of the charges, and results in plasma heating. Another form of dissipation and heating also comes with a process called *magnetic reconnection*, which is the topological rearrangement of the

magnetic field lines. An important characteristic of reconnection is that it can also give rise to an acceleration of the particles. This can happen in strongly magnetized configurations when reconnection breaks the equilibrium between magnetic pressure and tension, so that magnetic energy is converted into bulk kinetic energy.

2.2 The central engine: a unipolar inductor

Up to date, a theoretical model for the jet formation capable of fully reproducing the observed properties is still under development. However, the basic process through which energy can be initially channeled into a jet is quite clear. The gradient of a pressure P , the latter exceeding the particle energy density at the base of the flow, is needed in order to accelerate the plasma. A jet launching solely exploiting the gradient of thermal pressure is ruled out, as it implies too high a mass loading for the jet to reach relativistic speeds ([McKinney 2006](#)) and it requires very high temperatures of the gas in the accretion disk. At present, the most successful launching models are those involving the magnetic pressure. Two main properties of the central engine are needed in the magnetic launching scenario:

- the presence of a conductive charged object threading a poloidal magnetic field
- the rotation of the central object

The accretion disk orbiting the central SMBH clearly satisfies these conditions, as strong currents can be maintained in it and a magnetosphere can be anchored. [Blandford & Payne \(1982\)](#) were the first to describe how the rotation of a magnetized accretion disk can efficiently power a jet (BP mechanism). Alternatively, it had been previously shown ([Blandford & Znajek 1977](#)) that the source of energy can be the rotation of the SMBH itself (BZ mechanism). Qualitatively, the mechanism of extraction of energy is independent on the nature of the central source, and it is though to act like an unipolar inductor. Since the magnetic field lines are frozen in the plasma, a rotation of the central object also implies a rotation of the magnetosphere. Let Ω be the angular velocity of the system about its polar axis. The free charges on the surface of the disk will experience a Lorentz force $f = q\mathbf{v} \times \mathbf{B}$, with q being the electric charge, $\mathbf{v} = \Omega r$ the linear rotational velocity and r the cylindrical radius. This leads to a separation of the charge on the disk surface and to the generation of a quadrupole electric field (Fig. 2.1). If the magnetic momentum vector is aligned with the spin vector, the current will flow from the poles to the equator. The important result of this process is that the Lorentz force provides a net torque extracting the rotational energy of the central object. Actually, in the [Blandford & Znajek \(1977\)](#) mechanism the quadrupole electric field can in principle be generated independently of the

presence of surrounding matter, and therefore charge separation. [Wald \(1974\)](#) has shown that a black hole with a magnetic field rotating in the vacuum can, equally to a conductive disk, generate a quadrupole electric field. However, since black holes have approximately no charge, they cannot support magnetic fields by themselves, therefore an accretion disk is anyway necessary. One difference between the BP and BZ mechanism may reside in the composition of the jet they produce. A jet launched from the disk may more easily be loaded with protons and ions besides electrons and positrons, while material launched from the black hole's ergosphere may more likely be composed of light particles only (e^+ , e^-). These are thought to be produced from the collisions of high energy photons from the accretion disk in the black hole's magnetosphere. Concerning the mass loading, this should depend in both cases on the physical conditions of the disk and also on the inclination of the field lines, given that lines which are too close to the axis cannot efficiently load material ([Blandford & Payne 1982](#)).

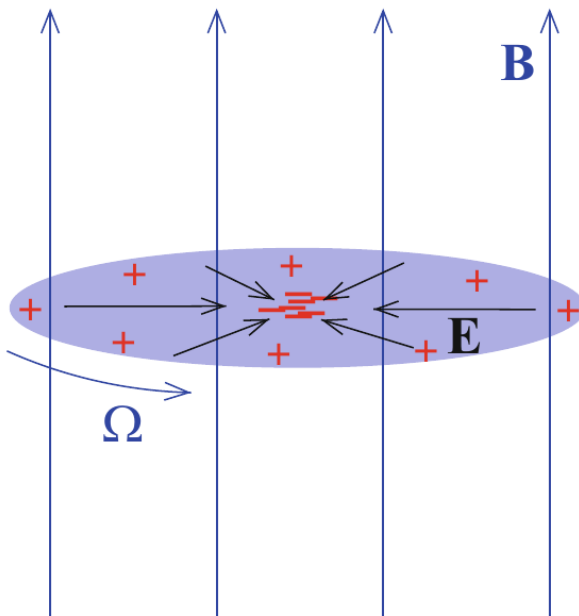


Figure 2.1: A conductive object rotating with angular velocity Ω in a uniform magnetic field B experiences a Lorentz force causing a charge separation. The latter generates a quadrupole electric field E . Image Credit: [Contopoulos et al. \(2015\)](#).

2.2.1 Magnetic fields and jet power

The jet power L_J resulting from the magnetic launching depends, both in the BP and BZ case, on the angular velocity Ω of the central object and on the accumulated magnetic flux Ψ as:

$$L_J \propto \Psi^2 \Omega^2 \quad (2.2.1)$$

The possibility of accumulating a certain large scale magnetic field in the disk is strictly related to the very origin of the field and to the physics regulating its transportation and penetration through the accretion disk. Both things are, nevertheless, poorly understood. The magnetic field permeating the ISM clouds in the host galaxy at a micro-Gauss level can, in principle, be accreted towards the center and ultimately reach much higher strengths. But in order for this to happen, some stabilizing mechanism must be at play for contrasting the turbulences and the outward diffusion in the disk and enabling the field to stay highly ordered. According to [Rothstein & Lovelace \(2008\)](#), the field accretion can be successful, as turbulences can be dumped if the field is strong enough. Other studies have analyzed the possibility that the field is generated on small scales. As it happens in other conductive astrophysical objects, a regular field may arise locally by a MHD disk dynamo ([Brandenburg et al. 1995](#)), supported in this case by the MRI turbulence (Sect. 1.1.2). However, it is not clear how efficient this mechanism can be. Despite these theoretical difficulties, observations strongly suggest that the magnetic field finds his way, somehow, to the inner sections of the accretion disk. In a recent study of a large sample of radio-loud sources ([Zamaninasab et al. 2014](#)), the nuclear magnetic field strength has been derived from the jet radio luminosity. Surprisingly, the inferred magnetic forces are as high as they can be, i.e. comparable with the black hole's gravitational pull. Disks featuring dynamically important magnetic fields were already theorized by [Narayan et al. \(2003\)](#): they are the so-called *Magnetically Arrested Disks* (MADs). The adjective "arrested" is connected to the fact that in the inner disk the magnetic pressure gets enough strong for disrupting it and ceasing the accretion. This happens at a radius which is typically quite larger than the event horizon, which may have important implications for the accretion disk physics and for the jet formation. Numerical simulations ([Tchekhovskoy et al. 2011](#)) confirm that MAD systems can produce strong jets, with powers up to 140% of the accreted rest-mass energy $\dot{M}c^2$ in the case of a maximally spinning black hole. This means that more than what comes in can goes out, and the difference must then be at the expenses of the black hole's rotational energy. This prediction agrees very well with another recent observational study ([Ghisellini et al. 2014](#)), showing that the jet luminosity is correlated with the disk luminosity but at the same time is much larger than it. Most importantly, these results indicates that the BZ mechanism best explains

the properties of relativistic jets, at least of the most powerful ones which we preferentially observe.

2.2.2 The radio-loud / radio-quiet dichotomy

As explained in Section 1.2, the class of radio-loud objects does not differ significantly from the radio-quiet class in anything but the presence of a jet. If, on the one hand, the transition between the radio-quiet and radio-loud modes may be smoother than previously thought (e.g [Panessa & Giroletti 2013](#)), it is undeniable that a dichotomy exists. What is its origin? This is one of the big open questions in the field. By considering the expression 2.2.1 for the jet power, we note that it is function of only the black hole's angular velocity and of the magnetic flux accumulated in the accretion disk. Therefore, the dichotomy should be driven by one of these parameters or by both. If the magnetic field is indeed accreted from the medium in the host galaxy, and not generated *in situ*, it is reasonable to think that different AGN can accumulate a very different magnetic flux depending on the local conditions of the ISM clouds. Anyhow, this is somewhat speculative for the moment, as systematic studies pointing in this direction are still missing. Concerning the BH-spin, this parameter is strictly related to the dynamical history of the system. In the most likely case, accretion may consist of a large number of events with a randomly oriented angular momentum, resulting in a final spin-down of the black hole ([Moderski et al. 1998](#)). Therefore, one possibility is that radio-loud objects represent the minority of cases with an history leading to a spin-up. However, this hypothesis has no solid ground at the observational level. Spin measurements from X-ray reflection spectroscopy (Sect. 1.1.2) have identified a fairly large population of rapidly spinning radio-quiet objects ([Reynolds 2014](#)). On the other hand, radio-loud AGN with a measured spin are not many. One of them is 3C 120, whose black hole is also maximally spinning. The conclusion from these results is that the spin may be an important parameter, but not the only one determining the presence or absence of a jet. In the last years, different studies (e.g. [Garofalo et al. 2010](#)) have suggested the idea that black hole/accretion disk systems with retrograde orbits may more easily trigger a jet. This is due to the fact that, in such conditions, a much larger magnetic flux can be accumulated (*flux trapping effect*- [Reynolds et al. 2006](#)). A normal prograde orbit may turn into retrograde after a massive change in the angular momentum of the gas, for instance as a consequence of a major galactic merger. Qualitatively, this idea fits well with the notion that radio-loud AGN are mainly sitting in merging systems. A recent study ([Chiaberge et al. 2015](#)) has determined that 92% of the radio-loud AGN in the sample at redshift $z>1$ are associated with merger events, while this percentage decreases to 38% for the radio-quiet

objects.

2.3 Acceleration and collimation

Right after the plasma is channeled into a jet, the energy content of the flow is mostly dominated by the magnetic field. In order for the jet to reach the Lorentz factors of the order of tens, typically observed on parsec scales, this magnetic energy has to be converted into kinetic energy. Moreover, there must be some mechanism which collimates the flow, ultimately matching the observed small opening angles. The mechanism of conversion of Poynting flux, through which the jet is accelerated and collimated, is another strongly debated and difficult topic. In the following I describe the most favored theories, but other scenari may also be possible. As in the case of many other astrophysical problems, the equations can be greatly simplified by assuming no time dependence and axi-symmetry, which is what most studies assume. The magnetic field vector can then conveniently be decomposed into a poloidal and an azimuthal component, \mathbf{B}_p and \mathbf{B}_ϕ respectively, which in cylindrical coordinates (z, r, ϕ) can be written as $B_p = B_r(r, z)\hat{r} + B_z(r, z)\hat{z}$ and $B_\phi = B_\phi(r, z)\hat{\phi}$. The magnetic launching theory implies that the field is initially predominantly poloidal, while the field structure is subject to change as the jet expands.

The acceleration of the flow is thought to be driven by different mechanisms at different stages (see e.g. [Meier 2012](#)). The two main variables are the speed of the flow as compared to the characteristic speeds of magnetic waves (Sect. 2.1.3) and the magnetic field structure. The importance of the former is related to existence of critical surfaces associated with each magnetic wave, marking the location where the flow gets as fast as the wave. Any information carried by a certain type of wave cannot cross the respective critical surface, which therefore represents a wall between causally disconnected parts of the flow. With this in mind, we can identify different regimes in the acceleration region. Right at the launch point, close to the surface of the accretion disk, the speed of the flow is low enough for hydrodynamic processes to act. Depending on the thermodynamic conditions of the disk, the gas pressure may contribute to a certain extent to the initial acceleration. When the speed surpasses the slow magnetosonic limit, only magnetic acceleration can take over. Assuming that the disk is cool, the region above it is characterized by a low density, so that the magnetic pressure dominates over the gas pressure and the field can be considered *force-free*. In these conditions the central object, the magnetic field lines and the gas co-rotate altogether. The description of the acceleration mechanism in the force-free region depends on the reference frame. From the point of view of the rotating central object, the flow is everywhere parallel to the field and it is accelerated by the centrifugal force. In this

system, the magnetic field does no work. However, if the process is seen in an inertial frame (e.g the observer), the magnetic field has an azimuthal component and the acceleration is driven by the gradient of the magnetic pressure. The acceleration can only take place if the field lines are sufficiently inclined outward, implying that the jet will be broad at this point. This description is valid up to the Alfvén radius, i.e until the flow speed is lower than the Alfvén speed. When this threshold is reached, the field lines start lagging behind and co-rotation ceases (Fig. 2.2). The field develops a significant toroidal component (this time also in the frame of the central object) and acquires an helical geometry. The magnetic pressure gradient keeps driving the flow until the last speed barrier, reached on the fast magnetosonic critical surface. However, the speeds measured in jets typically exceed their

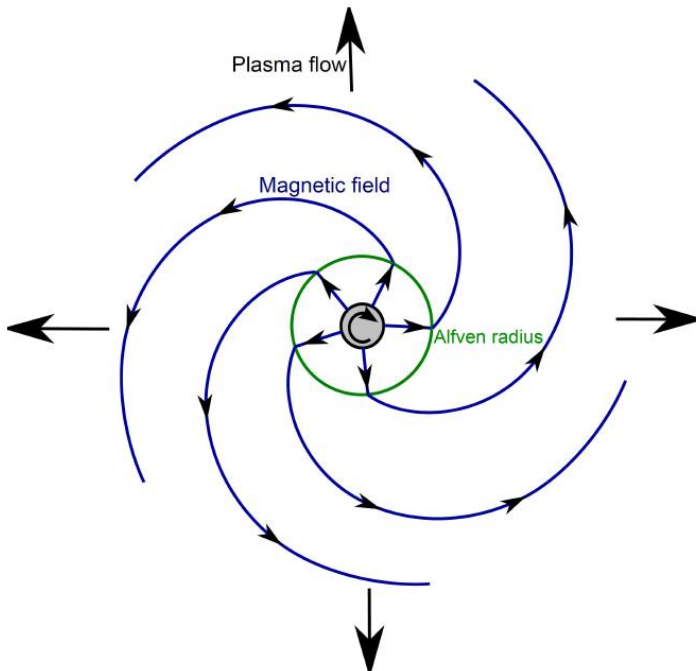


Figure 2.2: Magnetic field lines projected onto the equatorial plane. The field is poloidal up to the Alfvén radius, after which it develops a toroidal component. In 3D, the field structure beyond the Alfvén radius is an helix. Image Credit: [Clausen-Brown \(2012\)](#)

fast magnetosonic limit. How is the remaining acceleration produced? Various studies (e.g [Michel 1969](#); [Contopoulos & Lovelace 1994](#); [Beskin & Nokhrina 2006](#)) have addressed the problem of determining the terminal Lorentz factor Γ_∞ the flow is able to reach. The conclusion is that Γ_∞ depends on two parameters: the degree of magnetization at the base of the flow and the geometry of the flow. The former is quantified by the *magnetization parameter*

$$m = \frac{B_0^2}{4\pi\rho_0c^2} \quad (2.3.1)$$

where B_0 and ρ_0 are respectively the magnetic field strength and the mass density at the base of the flow. The terminal Lorentz factor can attain the maximum value $\Gamma_\infty \sim m$ if the Poynting flux is completely converted into kinetic flux. However, Michel (1969) demonstrated that in the classical and simpler assumption that the poloidal magnetic field is purely radial, i.e. it has a *split-monopole geometry*, the conversion of Poynting flux is inefficient, because the magnetic tension and pressure terms in Eq. 2.1.6 become comparable and cancels out as soon as the flow develops a significant Lorentz factor. In this geometry, Γ_∞ cannot exceed the limit $m^{1/3}$ and the flow remains magnetized up to long distances. More efficient accelerations can be achieved if the magnetic pressure term is at least slightly larger than the tension term. Analytical studies and simulations (Li et al. 1992; Tchekhovskoy et al. 2009) have shown that this condition is verified in collimating flows, because in this case the transverse component of the speed can be still smaller than the fast magnetosonic speed. The flow is, in this last regime, accelerated by the pinching force (or hoop stress) exerted by the azimuthal magnetic field, until also the transverse speed equals the fast magnetosonic limit. At this point, acceleration ceases and the jet becomes causally disconnected from the central engine, event which may possibly manifest through a shock or a re-collimation feature. In collimating flows, the terminal Lorentz factor can reach much higher fractions of the magnetization parameter. For instance, in a parabolic geometry it is possible to achieve equipartition between the magnetic energy and kinetic energy, with $\Gamma_\infty \sim m$ (e.g Lyubarsky 2009).

It should be noted that the azimuthal field alone cannot provide self-collimation because, even if the pinching force can act in the interior of the jet, the overall structure tends anyway to expand. Therefore, an ambient medium is necessary for the collimation to take place (Uzdensky & MacFadyen 2006; Spruit 2010).

2.3.1 Observational constraints

In terms of spatial scales, the acceleration and collimation processes described above are believed to act on extended regions, of the order of $10^3 - 10^4$ Schwarzschild radii (McKinney 2006), corresponding to a fraction of a parsec or to few parsecs, depending on the source. On an observational ground, this linear scales can be probed through VLBI observations. However, on the one hand speeds measurements are complicated in jets. This is especially true for blazars, in which the strong relativistic and projection effects make the calculation of the intrinsic parameters of the flow difficult. On the other hand, jets which are transversally resolved on these scales are few, and the exact geometry of the flow can not easily be determined. Among the few systematic VLBI studies of acceleration in jets,

the results found for the MOJAVE sample ([Homan et al. 2014](#)) appear compatible with the predicted extended nature of the acceleration. As a matter of fact, the average de-projected acceleration scale is ~ 100 pc, even larger than expected. Concerning the geometry of the flow, this was determined in few nearby FRI objects, M 87 ([Asada & Nakamura 2012](#)), 3C 84 ([Nagai et al. 2014](#)) and Cen A ([Müller et al. 2011](#)). The jet is found to expand parabolically in the case of M 87, and at an even slower rate in the other two objects, indicating that collimation from the medium is indeed acting.

Chapter 3

Radio Interferometry

Since the discovery of extraterrestrial radio emission by Carl Jansky, in the 1930's, the radio sky has been a continuous source of amazement for astronomers. The possibility of observing radio emission from the ground has allowed, since then, to constantly improve the observing technologies over the years, so to adapt to the rapidly evolving needs of the radio astronomy science. The driving scientific motivations have required increasing sensitivity and resolutions to characterize the instruments, which in the radio band can be especially difficult to obtain. In particular, the angular resolution of a telescope is inversely proportional to the wavelength of the radiation, implying that even very large telescopes can achieve only a modest angular resolution. In the 1940's, this problem has prompted astronomers to look for smart solutions, which were indeed found very soon ([Ryle & Vonberg 1946](#); [Ryle & Hewish 1960](#)) with the development of Aperture Synthesis. This discovery led to the award of the first Nobel prize for astronomical research, in 1974. Aperture Synthesis is the art of synthesizing a very large effective aperture from an array of telescopes. This elegant technique is applied in its full glory in Very Long Baseline Interferometry (VLBI), in which an aperture as large as the Earth size can be synthesized. This thesis makes entirely use of data from VLBI observations at high radio frequencies, up to \sim 86 GHz. In the following, I report the basic notions necessary for understanding the functioning of Radio telescopes and Interferometers (Sect. 3.1 - 3.3), while the second part of the chapter is dedicated to the calibration and imaging of VLBI data, with a special emphasis on the issues one might face when dealing with high radio frequencies. Apart from the specific references reported in the text, I refer to the textbooks from [Rohlfs & Wilson \(1996\)](#); [Taylor et al. \(1999\)](#) and to the online material from the European Radio Interferometry School 2013 (<http://www.astron.nl/eris2013/lectures.php>) and from the IMPRS blackboard lectures 2014 (<http://www.mpifr-bonn.mpg.de/2962412/2014>).

3.1 The radio window

From the point of view of an observer, the radio band comes with a series of advantages and disadvantages compared to other bands of the electromagnetic spectrum. The main and considerable advantage is that the radio waves are the only, together with the optical waves, capable of penetrating the atmosphere. This means that the construction of expensive space telescopes can be avoided. While the optical covers a tiny range of frequencies in the electromagnetic spectrum, the radio band extends for several orders of magnitude, approximately from ~ 300 GHz down to the very low frequencies. In practice, however, the effective observable window from the Earth is reduced due to a number of reasons. Above ~ 30 GHz (1 cm) the radiation is partially absorbed by the atmosphere, due to the vibrational and rotational transitions of molecules like water, oxygen and carbon dioxide. Moreover, the atmosphere itself is a radio emitter, which sometimes limits the possibility of performing sensitive observations, e.g in the vicinity of the water vapor line at ~ 22 GHz. At the very high frequencies, observations become accessible only from high and/or dry sites, like 2550 m site of the Plateau de Bure interferometer, in France, or the 5000 m site of the ALMA (Atacama Large Millimeter Array) radio telescopes, in Chile. In the far side of the low frequencies, below ~ 30 MHz (10 m), radio waves are reflected by the ionosphere, whose opacity depends on the season and on the solar activity. Observations above this wavelength are only possible outside the Earth's atmosphere and until the wavelength limit of about 10000 m, beyond which the interaction with the interstellar matter becomes important. Besides the aforementioned natural limitations, further disturbances are produced by civil and military radio signals, the so-called RFI (Radio Frequency Interference). This is a serious issue, as the faint astronomical signal is only a drop in the ocean compared to the human-related ones. For this reason, international agreements have been reached in order to reserve certain ranges of frequencies for the exclusive use of the radioastronomy community.

3.2 Antenna basics

Unlike optical and X-ray telescopes, radio telescopes can not detect radiation through the photoelectric effect. At radio frequencies photons do not have enough energy to ionize atoms, and photon counting is not an option. The measured quantity in a radio antenna, most commonly consisting of a parabolic dish, is the electromagnetic field of the incoming radiation. After impacting the dish, the electromagnetic waves are focused in a device called the *feed* and converted in electric signal with amplified intensity by a system of transducers.

In order to fully sample the field, which is a 2D vector, a dual polarization feed is in effect necessary. The astronomical signal detected is extremely faint, and avoiding signal losses in the feed as well as during the signal transmission is of fundamental importance. Therefore any electronic manipulation is not performed at the observing radio frequency, but at an intermediate frequency IF between 150 or 400 MHz. The down-conversion is operated by an *heterodyne system* by mixing the signal with a pure frequency tone provided by a *local oscillator* LO. The LO frequency must be very close to the observing one.

Below I explain how, after an appropriate calibration, the signal is converted in a temperature and then in a flux density. But before that it is first of all necessary to understand what the telescope is actually measuring. It can be said that when a radio telescope points towards a portion of the sky it measures its temperature distribution. The measured distribution is however not isotropic, because both the surface brightness I_ν of the sky and the telescope response are characterized by a certain directionality. The *beam pattern* describes the directionality properties of an antenna, i.e. the distribution of the power received from a point source as a function of the angular distance θ from the antenna axis. The beam pattern results from incoherent phase summation at the focus as a consequence of Fraunhofer diffraction. In two dimensions, the normalized beam in polar coordinates can be written as:

$$P_n(\theta, \phi) = \frac{P(\theta, \phi)}{P_{\max}(\theta, \phi)} \quad (3.2.1)$$

and it consists of a main lobe centered around the antennas axis and of some sidelobes (Fig. 4.1). For a circular aperture of diameter D , the first null is located at $\theta = 1.22\lambda/D$, while the main lobe has a FWHM of $1.02\lambda/D$, which represents the angular resolution of the antenna. Ultimately, the antenna will measure a temperature T_A named *antenna temperature* resulting from the convolution of the sky brightness with the beam pattern, which can be expressed at a given frequency as:

$$T_A = \frac{A_e}{2k} \int_{4\pi} I_\nu(\theta, \phi) P_n(\theta, \phi) d\Omega \quad (3.2.2)$$

where k is the Boltzmann constant, Ω is the solid angle subtended by the telescope and A_e is the effective area of the telescope, differing from the geometrical area $A_g = \pi D^2/4$ by a factor of the aperture efficiency η . The efficiency is reduced in a real antenna due to a number of reasons, the main being the physical blockage caused by the focus and by the structure supporting it and the inaccuracies in the dish surface. The impact of the latter is very large at high frequencies. For example a surface with accuracy $\sigma = \lambda/16$ results in an

efficiency $\eta_s = \exp(-4\pi\sigma/\lambda)^2 = 0.5$. To quantify the efficiency as precisely as possible is important for deriving the flux density S_ν , which is the physical parameter one wishes to measure. In fact, this is related to T_A as:

$$S_\nu = \frac{2k}{A_e} T_A \quad (3.2.3)$$

Assuming that A_e is known, the scaling factor between temperature in Kelvin and flux density in Jansky, also known as the *antenna gain g*, can be obtained by observing a calibrator of known flux. It is important to note here that the actual output of the telescope is a temperature T_{sys} which include not only the sky signal T_A , but also the noise of the instrument generated by the electronics, with the latter actually contributing the most to the total. Therefore the sky contribution usually appears as a small amplitude signal superimposed on a noisy and large amplitude baseline. The signal to noise ratio (S/N) of the two can be increased by averaging over a large number of samples, due to the fact that the source signal will be correlated, while the noise will not. The number of samples N is limited by the bandwidth $\Delta\nu$. In fact the *Nyquist sampling theorem* states that samples taken over time intervals $\Delta\tau$ shorter than $1/\Delta\nu$ are not independent. This implies that the number of samples $N = \tau/\Delta\tau = \tau\Delta\nu$ can be increased by either increasing the bandwidth $\Delta\nu$ or the on-source time τ . Assuming that the noise is Gaussian, the error over N samples is reduced by a factor $1/\sqrt{N}$ compared to that on a single sample, from which we infer the *radiometer equation*

$$S/N = \frac{T_A}{T_{sys}} \sqrt{\tau\Delta\nu} \quad (3.2.4)$$

The above description implies that the main parameters of an antenna, its resolution and its sensitivity, both improve by increasing the dish diameter. However, increasing the dimensions of an antenna comes with considerable issues. Apart from the high costs, important technical problems arise. For example, a large and therefore heavy dish would distort under its own weight, leading to important deviations from the parabolic shape. Even when the technical challenges are pushed to the limit, like in the case of the largest telescopes Effelsberg (100 m), GBT (100 m) or Arecibo (300 m), the typical angular resolution varies between tens and hundreds of arcseconds. The angular dimensions of many interesting astronomical targets, like AGN, are far smaller than this. The next sections will show how interferometric techniques meet the scientific demands for high resolution observations.

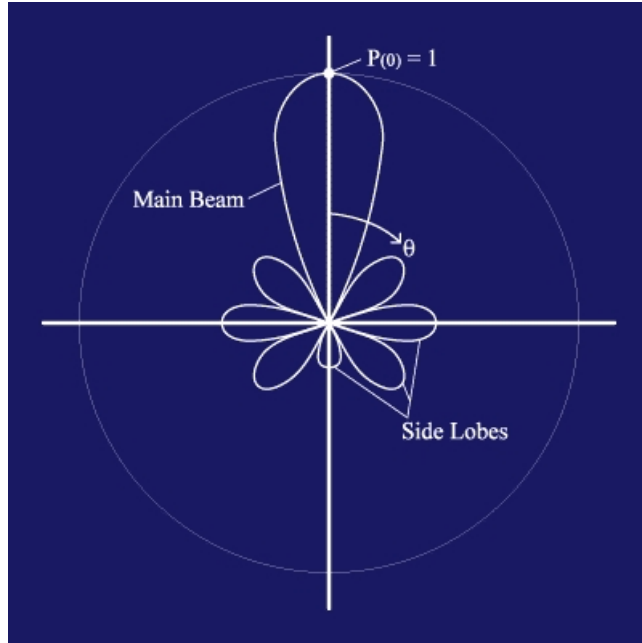


Figure 3.1: A 2D representation of a hypothetical antenna pattern. (Credit <http://www.ras.ucalgary.ca/radiotels/calibration.html>)

3.3 Interferometry

The basic unit of an interferometer is a pair of telescopes working as double slits of Fraunhofer diffraction, and separated by a distance b called *baseline* (Fig. 3.2). The two telescopes point simultaneously towards an astronomical source, in a direction defined by the vector s . Due to the difference in the path length, the radiation wave front with frequency ν impacts on the farthest interferometer element with a time delay $\tau_g = b \cdot s/c$, which translates into a phase shift $\phi = 2\pi\nu\tau_g$. The time dependence of the two signals can be written, in terms of voltages, as:

$$V_1 = V \cos[\omega(t - \tau_g)] \quad (3.3.1)$$

$$V_2 = V \cos(\omega t) \quad (3.3.2)$$

where V is the maximum amplitude and $\omega = 2\pi\nu$. The task of the *correlator* is at this point to coherently combine the signals, after an appropriate determination and correction of the time-variable phase shift. The first basic operations involved in this process are the multiplication and the averaging of the signals. For simplicity, let us assume that the correlator works at the sky frequency, although in reality the signal is usually down-converted to an intermediate frequency (IF) through the local oscillator (Sect. 3.2). The

operation of multiplication of 3.3.1 and 3.3.2 yields:

$$V_1 V_2 = \left(\frac{V^2}{2} \right) [\cos(2\omega t - \omega\tau_g) + \cos(\omega\tau_g)] \quad (3.3.3)$$

The time-dependent and rapidly varying term $\cos(2\omega t - \omega\tau_g)$ can be made negligible by averaging over a sufficiently large time interval, typically of 1 or few seconds. Therefore, after averaging, the combined signal assumes the simple cosinusoidal form:

$$R_{\cos} = \langle V_1 V_2 \rangle = \left(\frac{V^2}{2} \right) \cos(\omega\tau_g) = \left(\frac{V^2}{2} \right) \cos \left(2\pi \frac{\mathbf{b} \cdot \mathbf{s}}{\lambda} \right) \quad (3.3.4)$$

The latter equation expresses, in essence, what a correlator does. By combining the signals, the correlator casts a cosinusoidal coherence pattern on the sky, it multiplies this pattern by the source brightness and it integrates over the sky. However, it should be already noticed that the interferometer is only sensitive to a limited range of orientations and spatial scales, depending on the geometry of the array. This fact can be clearly seen in the simplest case of a single baseline. The resulting fringe pattern is oriented perpendicularly to the baseline direction, therefore the interferometer is only sensitive along the direction of the baseline. Also, since the fringes will be spaced by an angular distance given by λ/b , the two-elements interferometer is sensitive only to a certain spatial scale, depending on the length of the baseline. Long baselines provide information on the small scale structures of the source, while the short baselines sample the large scale ones. The work of the correlator is however not over at this point. In fact the cosinusoidal response R_{\cos} is not sufficient for recovering the source function. Being the cosine an even function, the response is zero for the odd part of the source brightness distribution. If instead a sinusoidal response is also available, the source function can be completely recovered. The sinusoidal pattern can be generated by simply introducing a 90° phase shift in one of the signals. After multiplying and averaging as described above, one obtains similarly:

$$R_{\sin} = \langle V_1 V_2 \rangle = \left(\frac{V^2}{2} \right) \sin(\omega\tau_g) \quad (3.3.5)$$

Once the two outputs R_{\cos} and R_{\sin} have been produced, all that remains is to combine them in the form of *complex visibilities*. This function is defined as:

$$\mathcal{V} = R_{\cos} - iR_{\sin} = A e^{-i\Phi} \quad (3.3.6)$$

where $A = \sqrt{R_{\cos}^2 + R_{\sin}^2}$ is the complex visibility amplitude and $\Phi = \tan^{-1}(R_{\sin}/R_{\cos})$ is the visibility phase. It can be easily shown that the complex visibility function allows

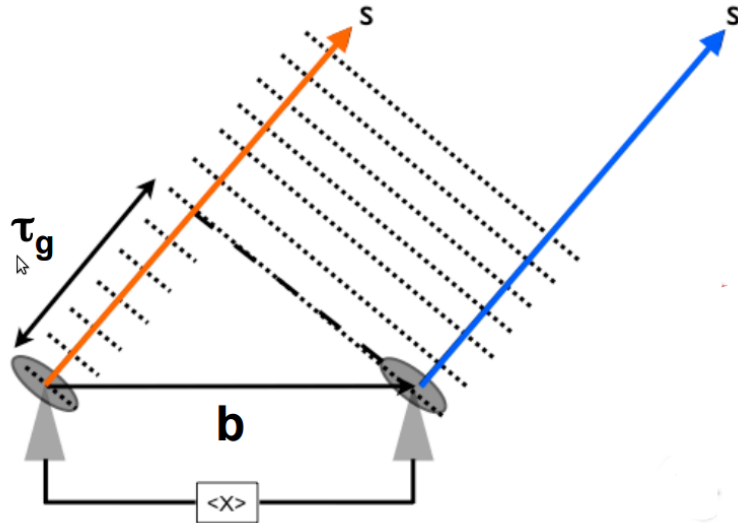


Figure 3.2: Two-elements interferometer. The separation \mathbf{b} is the baseline length. The radiation wave front, propagating from a direction \mathbf{s} , arrives at the telescope on the left with a time delay τ_g . (Image credit: IMPRS Blackboard Lectures 2014, Hans-Rainer Kloeckner).

to finally link the source brightness $I_\nu(\mathbf{s})$ (in a solid angle $d\Omega$) to the response of the interferometer with the elegant expression:

$$\mathcal{V}_\nu(\mathbf{b}) = \int \int I_\nu(\mathbf{s}) e^{-2\pi i \nu \mathbf{b} \cdot \mathbf{s} / c} d\Omega \quad (3.3.7)$$

Equation 3.3.7 means that source brightness is related to the measured quantities, i.e. the complex visibilities, by a Fourier transform integration. In 3D, the visibility function is more commonly expressed in the reference system defined by the direction cosines (l, m, n) , described in Fig. 3.3. In this system, the w axis points towards the source and it tracks it over time, the v axis points towards the north celestial pole and the u axis towards east. Therefore the plane formed by u and v is always perpendicular to the direction of the source. In this reference, the visibility function becomes:

$$\mathcal{V}_\nu(u, v, w) = \int \int \frac{I_\nu(l, m)}{\sqrt{1 - l^2 - m^2}} e^{-2\pi(u l + v m + w n)} dl dm \quad (3.3.8)$$

which is usually simplified by setting the w coordinate to 0. It is apparent that the more locations the interferometer can sample, the more reliable the reconstruction of the source function will be. The 2D space defined by the u and v coordinates expressed in units of wavelength is called *uv-plane*, and it simply describes whether or not a visibility measurement exists in a certain point. The filling of the uv-plane, the so-called *uv-coverage*

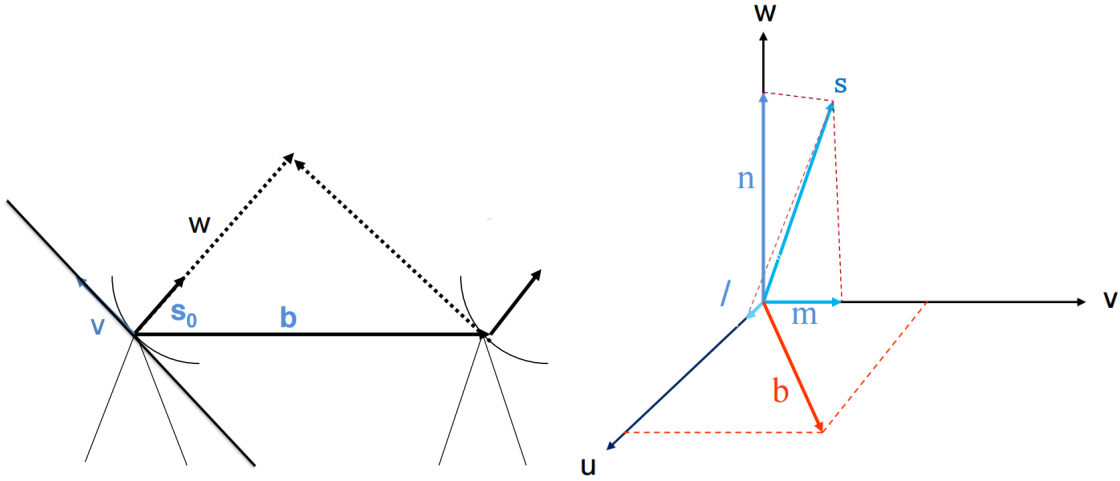


Figure 3.3: The direction cosines (l, m, n) reference system. The w axis points towards the source, the v towards the north celestial pole and the u to the east. (Image credit: IMPRS Blackboard Lectures 2014, Hans-Rainer Kloeckner)

is by definition incomplete in interferometry, and anyhow limited by the positions and number of the currently existing radio telescopes. Given a certain array, the uv-coverage can be improved by increasing the total on-source time up to 12 hours, due to the fact the Earth rotation allows a single baseline to sample a full track in the uv-plane. The above description applies in the simplified case of a perfectly mono-chromatic wave. However, real interferometers are characterized by a finite bandwidth $\Delta\nu$, which can represent both an advantage and a disadvantage for the observer, depending on the science case. Starting with a drawback, the correlator computes a delay which is exactly correct only for the central frequency and respect to the phase center, i.e the source position. Averaging over a bandwidth introduces an attenuation of the fringes, known as *bandwidth smearing*, which can be described by a *sinc* function of the kind $\text{sinc}(\tau_g \Delta\nu)$. For the longest baselines and for wide bandwidths one can have a very strong attenuation, and even a complete de-correlation. In the uv-plane, this effect can be seen as an averaging over a short radial cut, which may result in a distortion of the image in that range of spatial scales.

On the other hand, as seen in the case of single dish radio-telescopes, having a wide bandwidth increases the sensitivity of the array. For an array made of N elements, the sensitivity σ_S is given by

$$\sigma_S = \frac{2kT_{\text{sys}}}{A_{\text{eff}}[N(N-1)\Delta\nu\tau]^{1/2}} \quad (3.3.9)$$

One way for reducing the smearing but still having a sufficient total bandwidth, it to divide $\Delta\nu$ in sub-bands, in turn chunk them into an high number of channels, and then average over the bandwidth of a single channel. This method is, among other things, also effective

for better isolating and removing RFI signals.

3.4 VLBI arrays

The Very Long Baseline Interferometry (VLBI) is the most advanced and complex interferometric technique. Its peculiarity consists in synthesizing an effective aperture as large as the Earth size by combining non-connected array elements located in different continents. To date, VLBI observations provide the highest possible resolution in astronomy, down to the level of \sim tens of micro-arcseconds. This resolution comes however at the price of a remarkable technical effort. The previous section has shown how interferometry is all about keeping the signal coherence, therefore dealing with 10000 Km or more baseline length is an obvious challenge. Additional difficulties are related to the fact that antennas taking part in VLBI experiments were, with few exceptions, not conceived for this purpose, and each of them comes with its own specifications, from the dish diameters to the frequency standards. In VLBI mode, the radio signals are digitized and recorded at each telescope on high-capacity magnetic disks, with recording rates reaching several Gbit/s in the most advanced systems. At the same time, extremely precise time stamps, generally provided by atomic clocks (i.e. H-masers), are also registered. The data are then sent to a center for off-line correlation, which will have to deal with a very detailed model for delay compensation.

Standard VLBI arrays, like the VLBA (Very Long Baseline Array) in the United States or the EVN (European VLBI Network) in Europe, have represented in the last years and still represent and invaluable tool for investigating the nature of compact radio sources, and significantly boosted our knowledge of extragalactic jets. The quest for a deeper comprehension of these fascinating objects is, however, not over, as we are one step from the direct imaging of the very surroundings of supermassive black holes. Therefore in the past decade the VLBI community has been working for pushing forward the technical limitations and achieving even higher angular resolutions. This can be done by following two different approaches: increasing further the baseline length, i.e. moving to space, or increasing the observing frequency. The *RadioAstron* mission is a recent and successful example of space-VLBI technology. Ground arrays, on the other hand, can achieve a comparable resolution if observing at millimeter wavelengths. Observing at high radio frequencies gives the additional advantage of penetrating the opacity barrier at the base of relativistic jets, allowing a deep imaging of the nuclear regions to be obtained. Currently the highest frequency observations are provided by the *Global Millimeter VLBI Array* (GMVA) (Fig. 3.4), operating at 86 GHz. This array comprises 8 of the 10 antennas forming the VLBA,

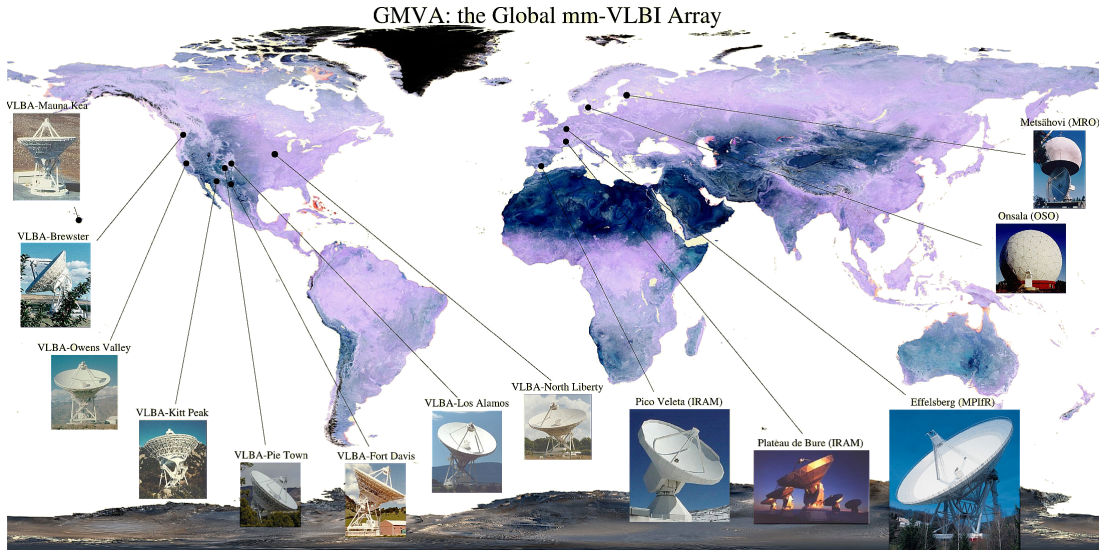


Figure 3.4: Global Millimeter VLBI Array (<http://www3.mpifr-bonn.mpg.de/div/vlbi/globalmm/>).

5 telescopes located in Europe (Effelsberg, Onsala, Pico-Veleta, Yebes, Metsahovi) and the phased array Plateau de Bure in France. The angular resolution achieved by the GMVA is of $\sim 50 \mu\text{as}$, which for the nearest sources translates into a linear scale of only few tens of Schwarzschild radii. At even higher radio-frequencies, the ongoing project of the *Event Horizon Telescope* (EHT) aims at achieving resolutions comparable with the event horizon by observing at 230 GHz. In the nearby source M87, EHT observations have already probed to be successful (Doeleman et al. 2012).

3.5 The calibration of VLBI data at mm-wavelengths

In Section 3.3 I explained how the correlator delivers a set of complex visibilities, and how these are related to the actual physical quantity one would like to measure, i.e. the brightness distribution of the astronomical source. In a real experiment, however, using directly the –inverse of– equation 3.3.8 for producing the final image of the source would usually not give good results. In fact, the visibility function provided by the correlator includes all the different kind of corruption terms introduced by the atmosphere and by instrumentation. Given a baseline formed by the antennas i and j , the real and the observed visibilities, $\mathcal{V}_{\text{true}}^{ij}$ and $\mathcal{V}_{\text{obs}}^{ij}$, will be related as:

$$\mathcal{V}_{\text{obs}}^{ij} = \mathcal{V}_{\text{true}}^{ij} G^i G^j \quad (3.5.1)$$

where G^i, G^j are called *complex gains*, and as the visibilities they have an amplitude and a phase. The calibration consists in determining the amplitude and the phase of the corrupting terms. In the following, I describe the fundamental steps necessary for the calibration of VLBI data at millimeter wavelength. The procedure does not differ substantially from the standard cm-wave data reduction. However, special care is required at certain steps, for example during the phase calibration. In fact, despite the efforts put in the correlation process for computing the time delays as precisely as possible, uncertainties in the models (e.g. related to time stamps, antennas or source positions, atmospheric models etc.) and other unpredictable factors have a strong impact at high frequencies. Therefore some residual offsets are common when the data are delivered. Also the amplitude calibration can present some issues and, depending on the weather conditions during observations, an accurate opacity correction is often crucial.

3.5.1 Inspecting the data in AIPS

Although some newer softwares for the calibration of interferometric data have been developed (e.g. CASA), the old program AIPS (Astronomical Image Processing System) ([Greisen 1990](#)) is still the most used in the VLBI community, mainly because it only implements a procedure named *fringe fitting* which is fundamental in many cases and especially at high frequencies. The data reduction in AIPS is based on a precise philosophy: data is sacred and it should not be altered, if not at the very end. For this reason the corrections calculated in each step of the calibration are not directly applied, but are stored in calibration tables named *CL tables*. In the same way, the flagging of data does not modify the data set but it simply creates *FG tables* which can be applied in the following tasks. When a data set is first loaded in AIPS, through the task FITLD, it usually already has some extension tables attached. One of this is the *TY table*, which stores the T_{sys} measurements recorded at each antenna and that are necessary for the amplitude calibration. However, the *TY table* is often missing when dealing with observations from non-standard arrays. In this case, a data file collecting the T_{sys} values for all antennas must be loaded through the separate task ANTAB. This file usually contains also the gain-elevation curves of each station, describing in a polynomial form the dependence of the effective area with elevation, which are stored by ANTAB in a GC table. At the beginning of the calibration it is good habit to take a look at the data through the task POSSM. After indexing the data with INDXR, it should also be checked, in the header, if the data were previously sorted chronologically, and if not run the task UVSRT. The task LISTR allows the list of scans and observed targets to be visualized, which also gives an insight on whether *sub-arraying* took place during

observations. The latter means that the array of antennas can be divided in sub-groups observing different sources at different times. This condition is often verified in Global VLBI observations, since the visibility times of the targets can be very different between continents. In this case, one can either try to flag some unneeded data in order to get rid of the sub-arraying, or proceed with it, implying that the amplitude calibration will have to be performed once per each sub-array.

3.5.2 Phase calibration

The aim of the phase calibration is to compute and correct for the residual delays $\Delta\tau$ so that visibilities can, in the end, be coherently integrated. Having residual delays also means having residual *delay rates*, i.e. the time derivatives of the delays $\Delta\dot{\tau}$. If t_0 is an initial reference time, together these will cause a frequency and time-dependent phase shift:

$$\Delta\phi = 2\pi\nu[\Delta\tau_0\Delta\dot{\tau}(t - t_0)] \quad (3.5.2)$$

The procedure through which the delays and rates are corrected is known as *fringe fitting* (see [Cotton 1995](#), for a review). There is not a single approach for developing a fringe fitting algorithm, and the choice depends on whether one prefers to deal with the delay-rate domain or with the time-frequency domain. In the first case, one can think to the residuals as “attenuator factors” of the amplitude of the signal, which is instead maximized if they are properly corrected before integration. This concept can be visualized in the $(\Delta\tau, \Delta\dot{\tau})$ domain as shown in Fig. 3.5. Each point in this space is characterized by a certain amplitude or, equivalently, correlation coefficient, and determining the correct $\Delta\tau, \Delta\dot{\tau}$ corresponds to finding the peak with highest *S/N*. This is known as *fringe search*. After finding the peak, data are averaged through the Fourier transform. In the original method ([Moran 1976](#)), the fringe search is performed on a baseline base, which however does not allow to calibrate those baselines showing non-detections. This problem was solved by [Alef & Porcas \(1986\)](#) by decomposing the residuals in antenna-based components. In the other approach considering the time-frequency domain ([Schwab & Cotton 1983](#)), the solutions are found collectively for the whole data and on an antenna-base by performing a linear fit to the phase variation as a function of time and frequency. The considered time interval, known as *solution interval* is specified by the user and it should be chosen as to ensure an approximately linear behavior of the phase variation. The advantage of the second method, called *global fringe fitting* is that it can increase the number of detections for weak sources. In AIPS the fringe fitting is run through the task FRING, which is quite complex and includes a large number of parameters allowing to fine-tune as much as possible the task for the

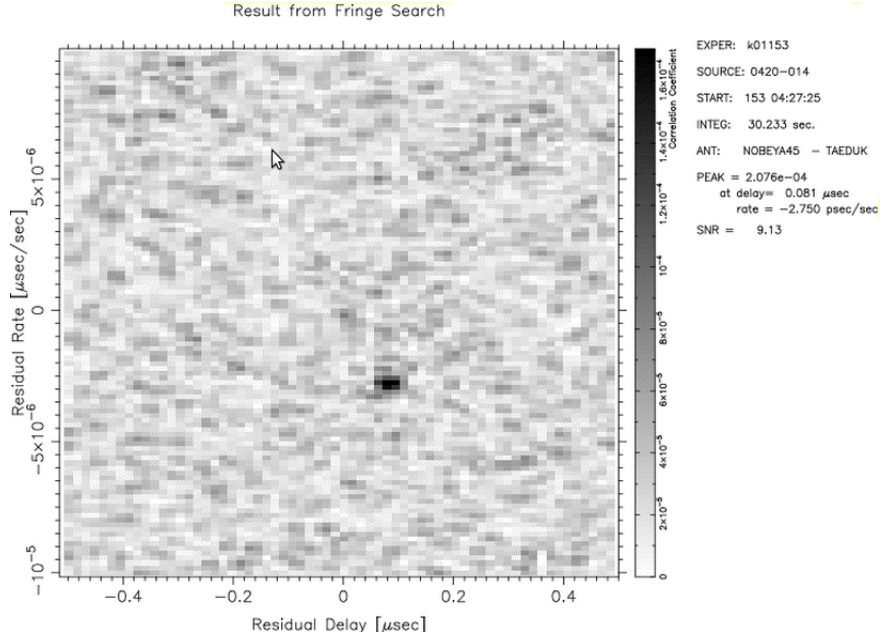


Figure 3.5: Fringe search in the delay-rate domain. (Image credit: <http://veraserver.mtk.nao.ac.jp/VERA/kurayama/WinterSchool/aips5.htm>).

specific needs of the experiment. In a GMVA or Global VLBI experiments, it is advisable to run FRING at least twice during the calibration. The first iteration is known as *manual fringe fitting*, and it is aimed at correcting for the “first order” residuals delays. Substantially, this first fringe should be performed on a limited time-range, even a single scan, in which fringes are clearly detected at all baselines, and on a single sideband base. The procedure may be divided in steps, e.g. first establishing the fringes for the American array, then for a good, inter-continental single baseline and finally for the European array. Between each step, the solutions found in the previous fringe need to be applied with CLCAL. During the fringe fitting it is important to carefully choose the reference antennas (the REFANT parameter in FRING), typically one for each continent, to which the algorithm assigns zero residuals. They should be antennas with good performances and possibly centrally located compared to the rest of the array. After the main residuals delays have been corrected, the probabilities of having detections also for the faintest sources and longest baselines are increased, and one can proceed with a second fringe run on the whole data-set.

3.5.3 Amplitude calibration

The raw amplitude visibilities, as delivered by the correlator, represent the amount of correlated noise, which comes quantified in arbitrary correlator units. These need to be converted to a meaningful unit, namely the Jansky. The antenna gain g , already introduced

in Sect. 3.2, defines at each station a quantity called the System Equivalent Flux Density (*SEFD*), which for an antenna A can be written as

$$SEFD^A = \frac{2kT_{\text{sys}}^A}{A_{\text{eff}}^A} \quad (3.5.3)$$

This relation implies that the correlated flux between two antennas A and B expressed in Janskys $S[\text{Jy}]$ is related to flux in arbitrary units $S[\text{x}]$ as:

$$S[\text{Jy}] = S[\text{x}] \frac{1}{y_c} \frac{\sqrt{SEFD^A \cdot SEFD^B}}{2\Delta\nu\Delta\tau} \quad (3.5.4)$$

where y_c is a parameter quantifying the data loss as a function of the digital sampling, $\Delta\nu$ is the bandwidth and $\Delta\tau$ is the integration time. Therefore by using the available information on the T_{sys} and A_{eff} values, stored in the TY and GC tables, one can perform the conversion using the task APCAL. However, it was already mentioned that, at high radio frequencies, the astronomical signal can be severely attenuated as it passes through the atmosphere. The atmospheric opacity τ_{atm} , attenuating the incoming signal by a factor of $e^{-\tau_{\text{atm}}}$, is a function of the source elevation. By indicating with τ_{zen} the zenith opacity and with χ the airmass, function of zenith angle z , this dependence is expressed as

$$\tau_{\text{atm}} = \tau_{\text{zen}}\chi(z) = \tau_{\text{zen}}\sec(z) \quad (3.5.5)$$

The task APCAL allows to perform the *opacity correction* if information on the weather conditions at each stations are provided. These are collected in a WX file, which can be loaded directly while running the task or stored in a WX table. The corrections are computed based on the available T_{sys} values after specifying initial guesses for the zenith opacity (TAU0) and the receiver temperature (TRECVR) at each station. When dealing with data at 43 or 86 GHz, the opacity correction step is crucial for recovering the correct flux information.

A final, important step of the amplitude calibration is the *bandpass correction*, applied by the task BPASS. This correction is made necessary due to the frequency-dependency of the response of the electronic system, which is usually attenuated at the edges of the bandwidth, i.e. in the first and last frequency channels. The bandpass response can be better inferred for scans showing clear detections, possibly of a strong calibrator source. BPASS computes this response and records it in a BP table, which can be applied before averaging the data in frequency.

3.6 Imaging and self-calibration

After calibration, the visibility data-set is finally ready to be imaged. The imaging of VLBI data can be more easily handled through the program DIFMAP ([Shepherd et al. 1994](#)), although similar functions are available in AIPS as well. It has been shown that the source brightness distribution can be obtained through an inverse Fourier transform of the visibility function. In DIFMAP this is done by applying a Fast Fourier Transform algorithm, which requires the data to be binned in a grid with the total pixels number set to an integer power of two. When this is first done, the obtained map is a *dirty map*, because it is convolved with the synthesized beam of the interferometer. The *dirty beam* is nothing but the Fourier transform of the uv-plane, which truly determines the response of the interferometer. The beam contamination can be eliminated by running de-convolution cycles, for example using the algorithm CLEAN ([Högbom 1974](#)). This algorithm finds the peak in the map, it subtracts the dirty beam at the peak position and it adds some model delta components, assigning a flux density and a position to each of them. This operation should be repeated until a significant peak flux is left in the residual map. When a satisfactory model has been obtained, a *clean map* can be produced by restoring it with a *clean beam*, i.e. a Gaussian function (circular or elliptical) obtained from fitting the central lobe of the dirty beam.

In principle, this procedure may be sufficient for obtaining a final map. In practice though, the quality of the image can still be greatly improved by further, higher order calibration steps which can be performed during the de-convolution cycles. This is the so-called *self-calibration*, with “*self*” indicating that the corrections are calculated based on an initial guess or model of the source itself. The model is exactly build during the de-convolution, therefore an appropriate, iterative use of CLEAN and self-calibration cycles should lead to an increasingly detailed and correct image. Self-calibration is based on the concept of *closure phases* and *closure amplitudes* which, in simple words, mean that when considering a sufficient number of antennas (3 for the phases and 4 for the amplitudes), the combined phase or amplitude is corruption-free, because the corruption terms relative to the single stations are canceled out. This can be easily verified in the two cases by remembering that the phase terms are additive while the amplitude terms are multiplicative. Starting from the model visibilities, the self-calibration algorithm computes the antenna gains by performing a least square fit consistent with the observed closure quantities. The higher the number of antennas, the higher the number of independent closure quantities, the more solid the self-calibration will be. Dealing with bright sources, self-calibration is certainly a valuable tool for improving the image quality, but it should be reminded that it is

a dangerous practice when imaging faint objects, particularly when missing a good starting model or when the number of antennas is small. This applies especially for amplitude self-calibration, which should be performed only with sufficient S/N and avoiding very short integration times.

Chapter 4

The stratified two-sided jet of Cygnus A: acceleration and collimation

This Chapter is partially published in the journal Astronomy & Astrophysics, and is reproduced with the permission of the Editor-in-Chief. Credit: Boccardi et al., A&A, 585, A33 (2016), reproduced with permission ©ESO.

The present thesis is entirely dedicated to the study of the radio galaxy Cygnus A using high resolution VLBI observations. For those readers who are familiar with radio astronomy, this is certainly a well known source, having been intensively studied since the very beginning of this science in the 1940's. At the redshift $z=0.056$, Cygnus A is by far the most luminous radio galaxy in the local Universe, comparable to the most luminous quasars at redshift 1 ([Carilli & Barthel 1996](#)). Due to its prominent double radio structure it is considered a prototype object of the Fanaroff-Ryley II class, and therefore an optimal target in studies aimed at testing the Unified Scheme for AGN (Sect. 1.2). A multi-band image of Cygnus A from Chandra, VLA and HST observations is shown in Figure 4.1. In the optical, the host galaxy appears as a cD elliptical galaxy with a poorly understood double nucleus ([Matthews et al. 1964](#)), located in a rich merging cluster ([Owen et al. 1997](#)). As in classical type II objects, the central AGN is heavily obscured, which is clearly proven by the detection of broad lines like MgII ([Antonucci et al. 1994](#)) in polarized light. An interesting characteristic of this source is that, even when correcting for the extinction, the central AGN is unusually faint if compared to the radio emission associated with the jet. The jet power is in the range $(0.7\text{--}4)\times10^{46}$ erg/s ([Ito et al. 2008](#)), while the bolometric luminosity of the accretion disk is an order of magnitude smaller ([Privon et al. 2012](#)), implying an Eddington ratio of ~ 0.01 , more typical of low luminosity radio sources. Therefore the radio loudness of Cygnus A is really striking and poses even more the problem of what makes the jet production so efficient in certain sources which look otherwise entirely similar to

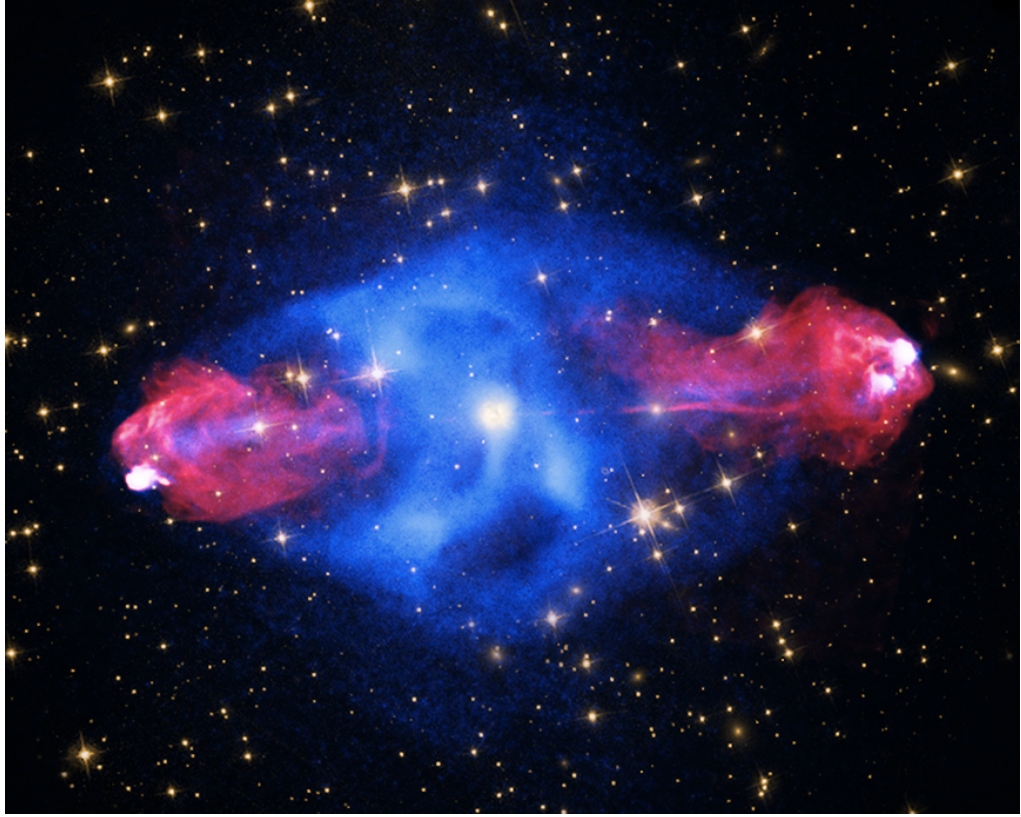


Figure 4.1: Multi-band image of the radio galaxy Cygnus A. **Blue:** X-ray from Chandra - **Red:** radio from VLA - **Yellow:** optical from HST and DSS. Image Credit: X-ray: NASA/CXC/SAO; Optical: NASA/STScI; Radio: NSF/NRAO/AUI/VLA.

the radio-quiet or radio-weak ones. In X-rays, besides a thermal component generated in the intra-cluster gas ([Carilli et al. 1994](#)), emission associated with the hot-spots in the radio lobes has been detected ([Harris et al. 1994](#)). The high energy emission is thought to result from Synchrotron-Self Compton or Inverse Compton scattering, indicating that a population of relativistic electrons still exists on kilo-parsec scales. The radio lobes, constantly replenished by the powerful and collimated relativistic jets, store huge amounts of energy of the order of $\sim 10^{60} - 10^{61}$ ergs, and extend for ~ 130 kpc. The radio jets are thought to be oriented at a large angle relative to the line of sight, most likely in the range $50^\circ - 85^\circ$ ([Bartel et al. 1995](#), and references therein). In presenting the results of this work it will be clear that the inclination close to the plane of the sky represents a fundamental advantage in the study of a relativistic jet, as it reduces the uncertainties in the determination of the intrinsic parameters of the flow. Indeed, the aim of this thesis work is exactly to provide observational constraints for the parameters of the flow on scales which are relevant for the mechanism of launching, acceleration and collimation of the jet. The scales probed in this work are enormously small, about one part in a million, compared to

the total extent of the radio structure observed with the VLA (Fig. 4.1). In this Chapter and in the rest of the thesis I shall use “we” in the discussion of the results, since they are the output of a collaboration.

4.1 Introduction

In Chapter 2 the currently most favored theoretical models for the launching, acceleration and collimation of relativistic jets were presented. In the discussion it emerged that if, on the one hand, the total jet power depends on the intensity of the magnetic field and on the black hole spin (see eq. 2.2.1), the kinetic power is strongly influenced by other parameters. Indeed, the possibility of reaching a certain terminal Lorentz factor depends strictly on the details of the process which converts the initially magnetically dominated jet into a kinetically dominated one. In theoretical models describing the conversion of Poynting flux, the mechanisms of acceleration and collimation of the flow show a strong interplay. In fact, as it was described in Sect. 2.3, the jet stops accelerating very early unless it is collimating at the same time. In jets missing a large scale (poloidal) magnetic field, i.e. featuring a purely toroidal field (Lynden-Bell 1996), an efficient magnetic self-collimation seems unlikely (Spruit et al. 1997), and confinement from an external medium appears to be the only possibility. The pressure from a poloidal magnetic field, on the other hand, can effectively confine the flow. However, an additional contribution from the external medium is anyhow necessary for preventing the terminal speed and collimation of the flow to be reached on unreasonably large scales (Tomimatsu 1994; Beskin et al. 1998).

Exact analytic solutions for these problems are difficult to obtain if one takes adequately into account the high degree of complexity of the system. While numerical simulations can considerably improve our knowledge, direct observations of the fundamental parameters of the flow on small scales are equally decisive. With the development of VLBI techniques at millimeter wavelengths and of space-VLBI, the spatial resolution achievable in observations of radio loud AGN has dramatically improved over the last few years, allowing us to zoom into the innermost regions of extra-galactic jets. Besides the possibility of obtaining explicit measurements of speeds, scale of the acceleration and shape of the flow, high resolution VLBI observations also allow the internal structure of the flow to be examined. Recent parsec and sub-parsec scale imaging has revealed that relativistic jets are far from the simple assumption of homogeneous conical outflows, and show instead a complicated transverse structure. Among other characteristics, limb brightening was observed both in some nearby FRI radiogalaxies, like M 87 (Kovalev et al. 2007) and 3C 84 (Nagai et al. 2014), and in blazars, as in the case of Mrk 501 (Giroletti et al. 2004) and 3C 273 (Lobanov & Zensus 2001). Limb

brightening has often been interpreted as the result of a spine-sheath structure of the jet, i.e. made of a fast and light ultra-relativistic spine embedded in a cylindrical flow of slower and denser material (Sol et al. 1989). Such a scenario provides a good explanation for some inconsistencies between observations and the standard unified model for AGN (Barthel 1989), as for example the lower Lorentz factors and lower intrinsic jet powers derived in FRI galaxies (sheath-dominated) with respect to BL Lac objects (spine-dominated) (Hovatta et al. 2009; Xu et al. 2000). Also, a spine-sheath interaction seems to be an essential ingredient for Spectral Energy Distribution (SED) modeling of TeV BL Lacs, where the high energy emission can hardly be reconciled with the low Lorentz factors deduced from VLBI studies (Ghisellini et al. 2005). The origin of such stratification is however unclear. A two-component jet with the described properties could directly arise (Hardee et al. 2007; Xie et al. 2012) from a jet launching process in which the external sheath is ejected from the accretion disk, while the central spine is fueled from the ergosphere. Alternatively, as shown in Lobanov & Zensus (2001) for 3C 273, a double-rail structure can also be effectively created by helical Kelvin-Helmholtz instabilities. In this case, if the emission is dominated by the pressure-enhanced regions of the instability, the observed motions will be those of the instability patterns, typically propagating at much lower speeds (0.1–0.5 c) compared to the flow or the shocks in the jet. In this chapter, a study of the jet transverse structure and kinematics of Cygnus A is presented, based on Global VLBI observations at 43 GHz. At the source redshift, 1 mas corresponds to ~ 1.084 pc, therefore these observations provide an angular resolution of ~ 400 Schwarzschild radii for $M_{\text{BH}} = 2.5 \times 10^9 M_{\odot}$ (Tadhunter et al. 2003), and allow the immediate surroundings of the central engine to be imaged. Due to the large viewing angle, both geometrical and relativistic effects are much reduced, implying respectively that the intrinsic morphology and speed of the flow can be more easily inferred and that a counter-jet can be detected. Moreover, both the main jet and the counter-jet can be transversally resolved on sub-parsec scales, which is fundamental for studying the collimation. Ultimately, while more such studies have been carried out on FRI radiogalaxies (e.g M87, 3C84, CenA), few observational constraints have been provided for strong FR II objects, mainly because their jets are generally fainter on parsec scales. Cygnus A is in this respect a unique target.

4.2 Observations and data reduction

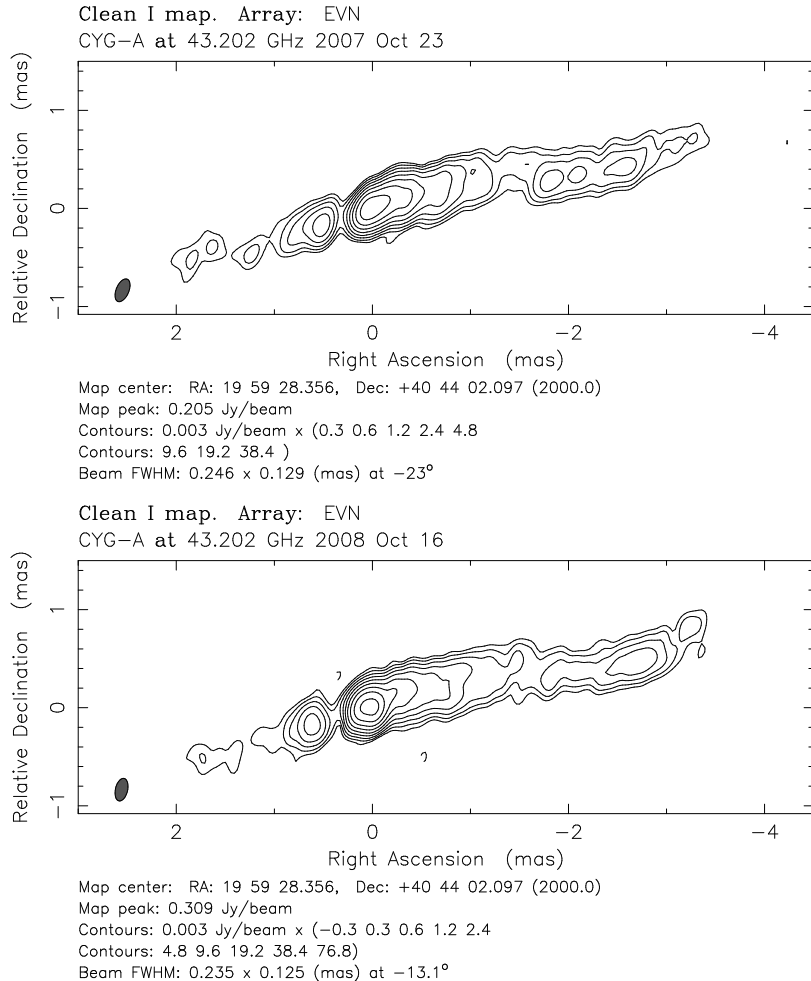
The data set comprises 4 epochs at 7 mm (43 GHz) from Global VLBI observations made between 2007 and 2009 (Tab. 4.2.1). The long total on-source time of ~ 8 hours, spanned over a ~ 16 hour track, and the large number of antennas (varying between 13 and 15)

Table 4.2.1: Log of observations at 7 mm (43 GHz) and characteristics of the clean maps (Fig. 4.2). Col. 1: Day of observation. Col. 2: Array. VLBA - Very Long Baseline Array; GBT - Green Bank Telescope; On - Onsala; Nt - Noto; Eb - Effelsberg; Ys - Yebes. Col. 3: Correlator. Col. 4: Beam FWHM and position angle. Col. 5: Peak flux density. Col. 6: Noise. All values are for untapered data with uniform weighting.

Date	Antennas	Correlator	Beam [mas, deg]	S_p [mJy/beam]	rms [mJy/beam]
23/10/2007	VLBA*, GBT, On, Eb, Ys	JIVE MKIV	$0.23 \times 0.11, -21.9^\circ$	197	0.13
16/10/2008	VLBA*, GBT, On, Nt, Eb, Ys	JIVE MKIV	$0.22 \times 0.10, -11.0^\circ$	264	0.11
19/03/2009	VLBA, GBT, On, Nt, Eb, Ys	Bonn MKIV	$0.23 \times 0.09, -12.5^\circ$	269	0.14
11/11/2009	VLBA, GBT, On, Nt, Eb	Bonn MKIV	$0.19 \times 0.10, -20.1^\circ$	226	0.32

*Saint Croix data not available.

produced a good uv-coverage. During observations, antennas were frequently switched between the target and the nearby calibrator J2015+3710, in order to reduce pointing errors at the biggest dishes and to later use this source as a fringe delay calibrator. For the first three epochs, data were recorded in dual polarization mode using 4 sub-bands (IFs) with a total bandwidth of 64 MHz per polarization (512 Mb/s recording rate). The last epoch,



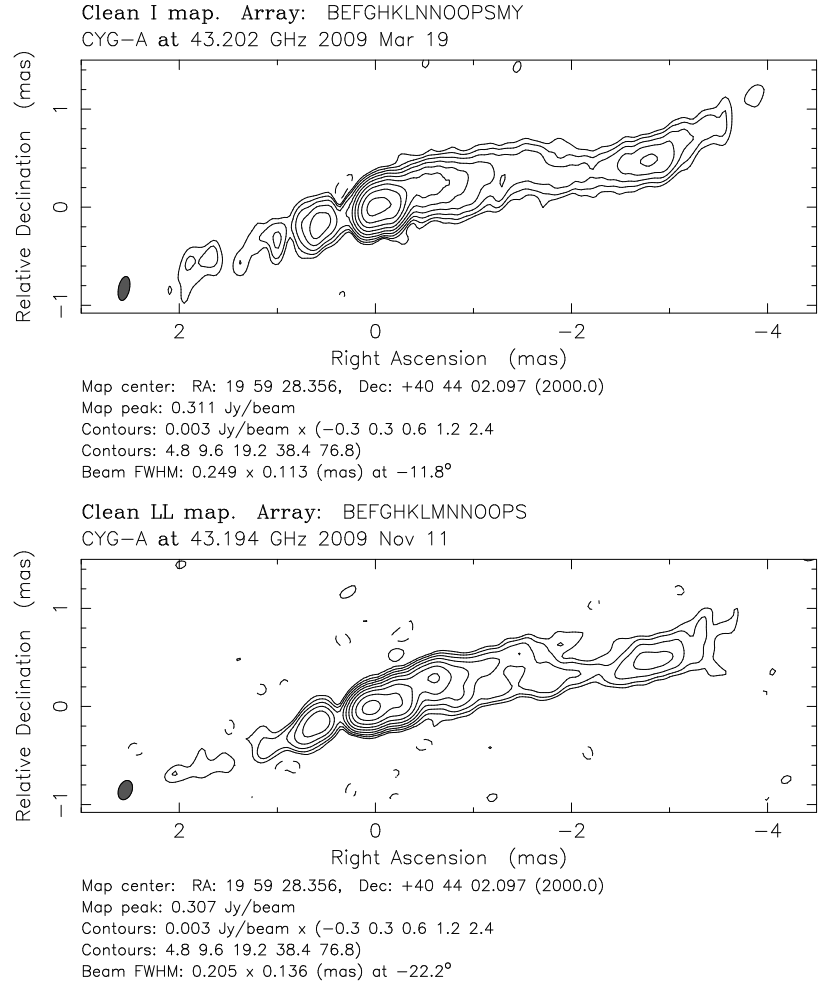


Figure 4.2: Clean maps of CygA from Global VLBI observations at 43 GHz. A taper of 0.1 at a uv-radius of $1400 M\lambda$ was applied, therefore the beams differ slightly from the values reported in Tab. 4.2.1.

instead, was observed in single polarization, with 16 sub-bands and a total bandwidth of 128 MHz. Data were calibrated in AIPS following the standard procedures, including fringe fitting, opacity correction for atmospheric attenuation and bandpass calibration. The imaging and self-calibration of amplitude and phase were performed in DIFMAP (Difference Mapping). The clean maps are shown in Fig. 4.2.

4.3 Data analysis

4.3.1 Model fitting and alignment of the images

Since the absolute position information is lost during phase self-calibration of VLBI data, one of the main difficulties in multi-epoch studies is image registration. This can be

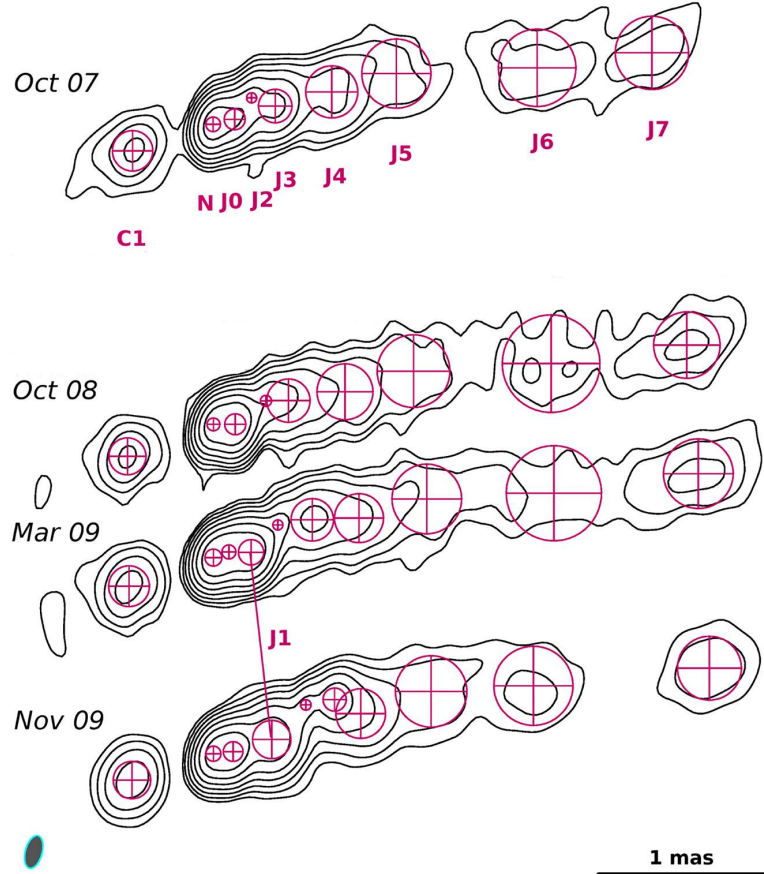


Figure 4.3: 43 GHz modelfit maps of CygA. Images were tapered and convolved with a common beam with FWHM of 0.2×0.1 mas, $pa = -15^\circ$. Contours represent isophotes at 1.8, 3.6, 7.2, 14.4, 28.8, 57.6, 115.2 mJy/beam. The reference point for the alignment is component N, assumed to be stationary.

particularly challenging in the case of radio galaxies because, unlike in blazars, a prominent VLBI core to be taken as the stationary reference point is usually missing. In order to obtain a simplified model of brightness distribution of the source, we have fitted circular Gaussian components to the complex visibilities using the MODELFIT subroutine in DIFMAP. The components were then cross-identified in the 4 epochs, taking into account their size, flux density and the morphology of the region (Fig. 4.3 & Tab. 4.3.1). The images were finally shifted and aligned on the position of component N, assumed to be stationary. This feature, although it may not coincide with the true jet base, is the most compact and describes a region with negligible morphological changes. The same choice was made in Krichbaum et al. (1998) (there named J0), based on a spectral and kinematic analysis. Note that, by applying the aforementioned shift, the positions of a sharp gap of emission at ~ 0.25 mas to the east of component N also become aligned. The nature of this feature, already noticed in Bach et al. (2008), is discussed in Sec. 5.6.

Table 4.3.1: Properties of the MODELFIT gaussian components in epoch 1 (2007.81), 2 (2008.79), 3 (2009.21) and 4 (2009.86). Col. 1: Component label. Col. 2: Epoch. Col. 3: Radial separation from the core N. Col. 4: Integrated flux density. Col. 5: Transverse size (FWHM). Col.6: Proper motion. Col. 7: Apparent speed.

ID	Ep.	z [mas]	S_ν [Jy]	r [mas]	μ [mas/year]	β_{app} [c]
C1	1	-0.504±0.043	68±14	0.240±0.043		
	2	-0.545±0.063	61±16	0.220±0.063		
	3	-0.529±0.041	78±15	0.243±0.041		
	4	-0.508±0.046	79±17	0.222±0.046	-0.00±0.02	0.00±0.06
N	1	0	254±20	0.087±0.002		
	2	0	223±24	0.076±0.003		
	3	0	313±31	0.101±0.003		
	4	0	212±14	0.090±0.002		
J0	1	0.131±0.002	212±15	0.124±0.002		
	2	0.130±0.003	473±39	0.125±0.003		
	3	0.098±0.004	201±25	0.083±0.004		
	4	0.118±0.003	341±27	0.117±0.003	-0.01±0.01	-0.03±0.03
J1	1		
	2		
	3	0.226±0.005	446±40	0.151±0.005		
	4	0.357±0.026	359±55	0.228±0.026	0.20	0.75±0.04
J2	1	0.278±0.004	53±7	0.060±0.004		
	2	0.342±0.028	44±11	0.066±0.028		
	3	0.429±0.039	31±9	0.060±0.039		
	4	0.621±0.013	34±6	0.062±0.013	0.26±0.01*	0.96±0.05*
J3	1	0.385±0.005	212±17	0.199±0.005		
	2	0.467±0.040	143±27	0.257±0.040		
	3	0.629±0.026	140±21	0.252±0.026		
	4	0.789±0.014	84±13	0.138±0.014	0.31±0.01*	1.15±0.04*
J4	1	0.731±0.051	108±21	0.310±0.051		
	2	0.805±0.121	92±26	0.332±0.121		
	3	0.896±0.048	90±17	0.291±0.048		
	4	0.907±0.078	94±22	0.395±0.078	0.10±0.02	0.37±0.07
J5	1	1.129±0.113	50±12	0.411±0.113		
	2	1.230±0.245	59±21	0.432±0.245		
	3	1.315±0.170	66±20	0.414±0.170		
	4	1.345±0.248	64±23	0.425±0.248	0.12±0.01	0.44±0.05
J6	1	1.954±0.171	71±20	0.461±0.171		
	2	2.038±0.461	59±25	0.580±0.461		
	3	2.058±0.438	64±27	0.566±0.438		
	4	1.943±0.209	53±17	0.470±0.209	0.00±0.03	0.00±0.10
J7	1	2.641±0.152	57±16	0.436±0.152		
	2	2.851±0.270	71±20	0.395±0.270		
	3	2.923±0.127	89±23	0.414±0.127		
	4	2.990±0.176	56±17	0.379±0.176	0.18±0.02	0.67±0.07

*Since J2 and J3 are accelerating, their proper motion and apparent speed depend on time.

The values in Table refer to the last epoch, November 2009.

According to the cross-identification described, a new component (J1) was ejected from N towards west between October 2007 and March 2009, accompanied by a brightening by about 50% of the core and inner-jet region. The kinematics resulting from this alignment will be presented in Sect. 4.4.1. Concerning the error bars associated with the each parameter of the gaussian components, reported in Tab. 4.3.1, a rigorous method taking into account the local signal to noise in the image around each feature was applied (see [Lobanov 2005](#); [Schinzel et al. 2012](#), for the details of the method). Since the formal positional errors obtained are quite small compared to the beam size, conservative values equal to 10σ for the radial separation (Col. 3) and 5σ for the transverse size (Col. 5) were assumed.

4.3.2 Transverse structure

For analyzing the transverse structure of the jets in Cygnus A, the four CLEAN images were convolved with a common circular beam of 0.15 mas, which is approximately intermediate between the major and minor axes of the natural beams (Tab. 4.2.1). Therefore, a slight super-resolution in the transverse direction was applied. The analysis was performed both on the single epoch maps and on a stacked image (Fig. 4.4), created after aligning the four maps as described in Sect. 4.3.1. In order to facilitate the study, the images were first rotated by 16 degrees clockwise, so that the mean jet axis was parallel to the x axis, and sliced pixel-by-pixel (1 px=0.03 mas) using the AIPS task SLICE in the transverse direction. Then, the transverse intensity distributions of each slice were fitted with Gaussian profiles using the task SLFIT. This task was ran twice for the entire length of the jets, first fitting a single Gaussian and then fitting two Gaussian profiles.

4.4 Results

4.4.1 Kinematic analysis and components light-curves

The proper motions μ of the features described in Fig. 4.3 were calculated by fitting their radial separations z (Tab. 4.3.1, Col. 3) from component N with time t , as shown in Fig. 4.5. The motion of components J2 and J3 is best described by 2nd order polynomials, indicating an acceleration. An estimate of the kinematic parameters was obtained by fitting a simple parabola of the form $z(t) = at^2 + c$. The motion of the remaining features, instead, appears more uniform and a linear fit was performed. The apparent speed $\beta_{\text{app}} = v_{\text{app}}/c$ can be calculated as $\beta_{\text{app}} = (\mu D_L)/(c(1 + Z))$, where D_L the luminosity distance, c is the speed of light and Z is the redshift. The values obtained for proper motion and for the apparent speed of each component are reported in Tab. 4.3.1, Col. 6. In the case of the accelerating

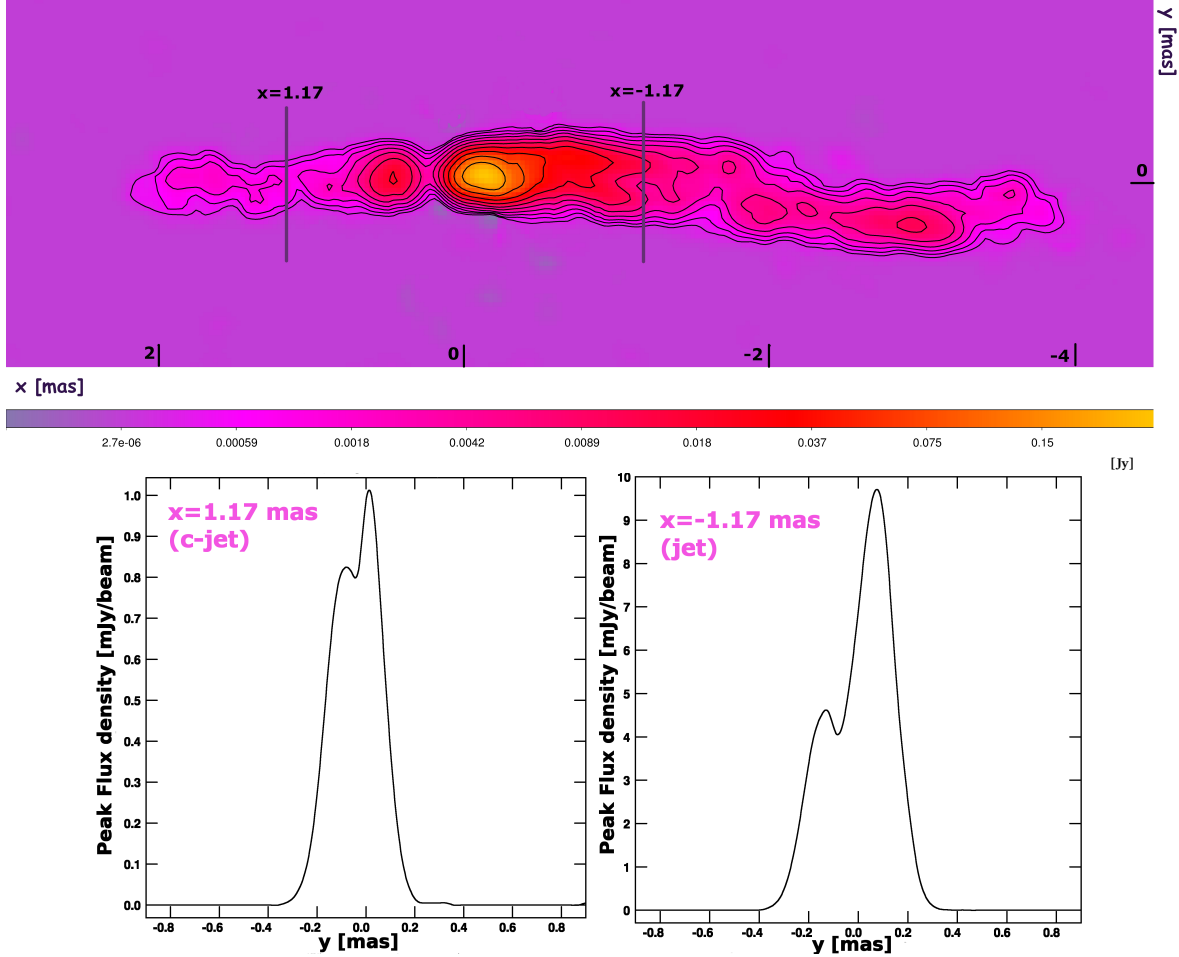


Figure 4.4: **Top** - Stacked 43 GHz image from observations in 2007-2009, rotated by 16° clockwise. It is convolved with a circular beam of 0.15 mas. Contours represent isophotes at 0.3, 0.6, 1.2, 2.4, 4.8, 9.6, 19.2, 38.4, 76.8, 153.6 mJy/beam. The four maps were aligned to the position of component N, as shown in Fig. 4.3. **Bottom** - Double peaked intensity profiles at the location of the cuts indicated in the top image.

features, J2 and J3, these parameters are time-dependent, and the values reported in Table refer to the last epoch, November 2009. In the approaching jet we observe an acceleration from $\beta_{\text{app}} \sim 0$ to $\beta_{\text{app}} = 1.15 \pm 0.04$ within ~ 0.8 mas from the core. Then the speed drops significantly, and increases again in the outer-jet, but remaining largely sub-luminal. Three components do not show a significant proper motion: C1 ($\beta_{\text{app}} = 0.00 \pm 0.06$), J0 ($\beta_{\text{app}} = -0.03 \pm 0.03$) and J6 ($\beta_{\text{app}} = 0.00 \pm 0.10$). Given the fact that the entire nuclear region, represented by component N and by the adjacent J0 and C1, appears stationary, a slightly different choice of the reference point for the kinematic study would not change the results; therefore the exact core registration is in this case not crucial. The hypothesis that the inner-jet components are crossing an acceleration region is supported by their light-curves (Fig. 4.6). The flux densities of J1, J2 and J3 are decreasing with time, while

those of the outer features (J4-J7) are approximately constant, or increasing in some cases. As the jet expands, a decrease of the emission by the traveling features may be expected because of adiabatic losses. However, we argue that this effect has little impact in our case. The distance traveled by each component during the period of the monitoring is in fact small enough that they do not experience significant changes of the jet width. As shown in Tab. 4.3.1 (Col. 5), the sizes of the components are either approximately constant in time or they vary slightly without showing a clear trend. Instead, differential Doppler (de)-boosting may better explain the observed properties. It is important to keep in mind that the Doppler factor δ is a monotonically increasing function of speed β only for a tiny range of viewing angles, approximately between 0 and 2 degrees. At larger angles, higher speeds often imply a lower boosting, or even a de-boosting ($\delta < 1$). The latter means that the narrow boosting cone of the emission can point away from the observer not only in the counter-jet, but also in the approaching side, at a sufficiently high speed exceeding the critical speed $\beta_{\delta=1}$:

$$\beta_{\delta=1} = \frac{2 \cos \theta}{1 + \cos^2 \theta} \quad (4.4.1)$$

Flows featuring Lorentz factors as high as 50 are already de-boosted if oriented at an angle of $\geq 11^\circ$, while a Lorentz factor of ~ 1.1 ($\beta \sim 0.49$) is sufficient at an angle of 75° . Since the viewing angle of Cygnus A is certainly large, we find it plausible that the quick and strong decrease in flux density of the inner-jet components is rather due to a decrease of their Doppler factors caused by an increase of the bulk Lorentz factor. This is, on the other hand, in agreement with the scenario suggested by the kinematic analysis. In this framework, the detection of the new feature J1 in March 2009 gives us the opportunity to calculate the Doppler factor of the flow at the position occupied by J1 in November 2009, $z = 0.36$ mas, and therefore to obtain an estimate for the jet viewing angle θ . Assuming that the flux density of J1 is close to the intrinsic one in March 2009 (due to the low intrinsic speed we expect at that position) the decrease of flux density constrains δ according to:

$$\delta = \left(\frac{S_{\text{obs}}}{S_{\text{int}}} \right)^{\frac{1}{2-\alpha}}, \quad (4.4.2)$$

where α is the spectral index, S_{obs} is the flux density of J1 in November 2009 and S_{int} is that in March 2009. With a classical synchrotron spectral index $\alpha = -0.7$ ($S \propto \nu^\alpha$), we obtain $\delta = 0.92$. A second constraint on the apparent speed $\beta_{\text{app}} = 0.75$ of J1 in November 2009 allows us to solve a system of 2 equations for deriving the viewing angle θ and the intrinsic

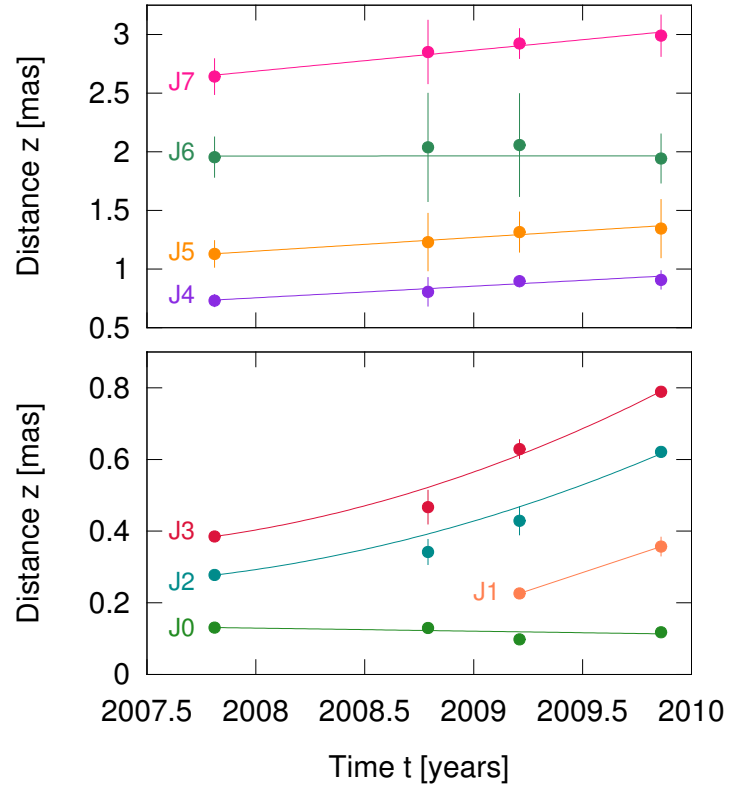


Figure 4.5: Radial distance from core z versus time t for the components in the outer-jet (top) and those in the inner-jet (bottom).

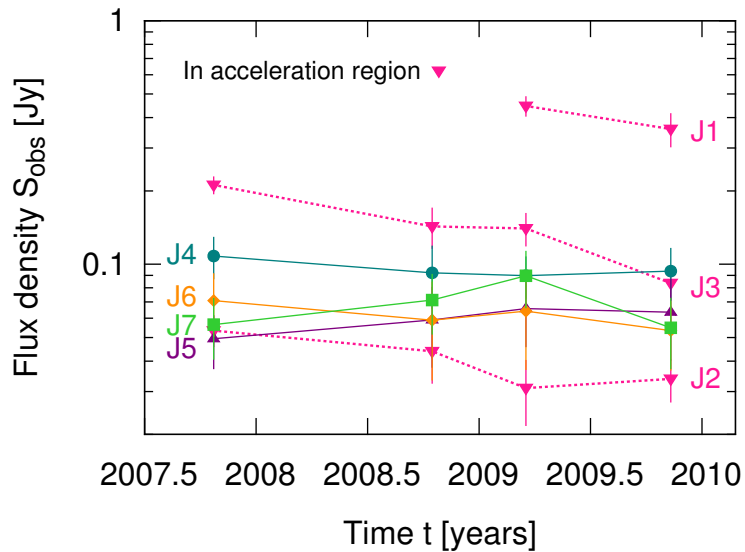


Figure 4.6: Light-curves of the jet components. The accelerating inner-jet components (dashed-magenta lines) are characterized by a decreasing flux density with time, while the outer ones (continuous lines-other colors), moving at constant speed, feature a more constant flux.

speed β at $z=0.36$ mas:

$$\beta_{\text{app}} = \frac{\beta \sin \theta}{1 - \beta \cos \theta}, \quad \delta = \frac{\sqrt{1 - \beta^2}}{1 - \beta \cos \theta} \quad (4.4.3)$$

obtaining $\beta(z = 0.36) = 0.65$ and $\theta = 74.5^\circ$. Strictly speaking, this viewing angle refers to component J1 and not to the entire jet. However, given the straight morphology of the jet from parsec to kilo-parsec scales, a substantial deviation from the calculated value is unlikely. Also, the viewing angle obtained can be considered an upper limit, because if the change of Doppler factor is not the only cause for the decrease of flux, a smaller viewing angle is required.

4.4.2 Ridge-line

The pixel-based analysis of the transverse intensity profiles shows that they are double peaked for most of the length of the source (Fig. 4.7). The limb brightening is most pronounced in the inner-jet, while a single ridge is visible further out, at a separation from the core between 2 and 4 mas. In the counter-jet we also find evidence for a limb brightened structure: the two ridge lines are closer to each other compared to the main jet, but still well separated after accounting for positional errors, assumed equal to one fifth of each FWHM. An error bar which also takes account of the SNR of the profile (as described in [Fomalont 1989](#)) was calculated for comparison. The latter yields unreasonably small errors in the brightest regions, while in the faint regions the errors are anyhow smaller compared to the first method of calculation. Therefore the most conservative error bars were chosen. In the central ~ 0.5 mas, the poor resolution does not allow a double profile to be clearly traced, and results from a single Gaussian fit are plotted. The same is done in the other regions of the jet where a well defined double ridge is missing (error bars of the two peaks overlapping or bad fit). The disappearance of the double profile in the main jet (at $z \gtrsim 2$ mas) is accompanied by an apparent bending of the jet axis towards the south and by a narrowing of the jet width, with the two ridges smoothly approaching each other. Interestingly, this position coincides with the location of the stationary component J6. While additional interpretations of this feature are proposed in Sect. 4.5.3, a more detailed analysis is necessary to establish if the observed structure can be ascribed to helical Kelvin-Helmoltz or to current-driven instabilities developing in the jet. However, following the previous discussion on relativistic effects in flows seen at large viewing angle (in summary: “the faster, the dimmer”), a natural explanation for the observed limb brightening would be the presence of a transverse gradient of the bulk Lorentz factor of a spine-sheath kind, i.e.

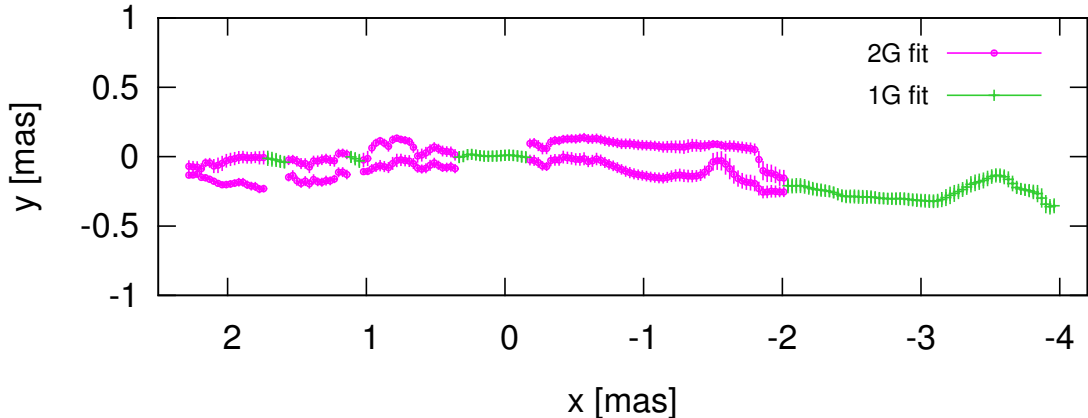


Figure 4.7: Ridge line structure of Cygnus A at 7 mm. The magenta color is used in those regions where a well defined double ridge line is present, while green points describe the remaining single-peaked regions. The error bars on the peak positions are set to one fifth of the de-convolved FWHM.

with Γ decreasing from the jet axis towards the edges.

4.5 Discussion

4.5.1 Two-layers acceleration

The kinematic and light-curves analysis of the VLBI maps at 7 mm has revealed the existence of an acceleration region in the inner-jet extending up to a de-projected distance of ~ 0.9 pc, assuming the viewing angle $\theta = 74.5^\circ$ derived in Sect. 4.4.1. In the outer-jet, lower speeds are determined, in agreement with findings from VLBI at lower frequencies (Bach et al. 2003). The observed fading of the fast flow (Fig. 4.6) suggests that these lower speeds do not represent an intrinsic deceleration, but are simply the signature that the contribution to the emission from the slower external layers has become dominant in that region. If we identify the two regions as representing the “fast” and the “slow” layers of the flow respectively, we can study separately their kinematic properties. In Fig. 4.8 (top) we plot the calculated intrinsic speeds β versus the de-projected distance from the core expressed in units of Schwarzschild radii R_S . We then note that the slow flow is also accelerating, but with a milder gradient compared to the fast one. In this case though, the range of speeds is such that the Doppler factor remains approximately constant, so we do not observe strong variations of the flux density. Both sections are accelerating over a large distance, at least of the order of $\sim 10^3 - 10^4 R_S$. This is a characteristic signature of relativistic magnetically driven outflows (Begelman & Li 1994; Contopoulos 1995; Vlahakis & Königl 2004), in which the conversion from Poynting to kinetic flux is expected to proceed

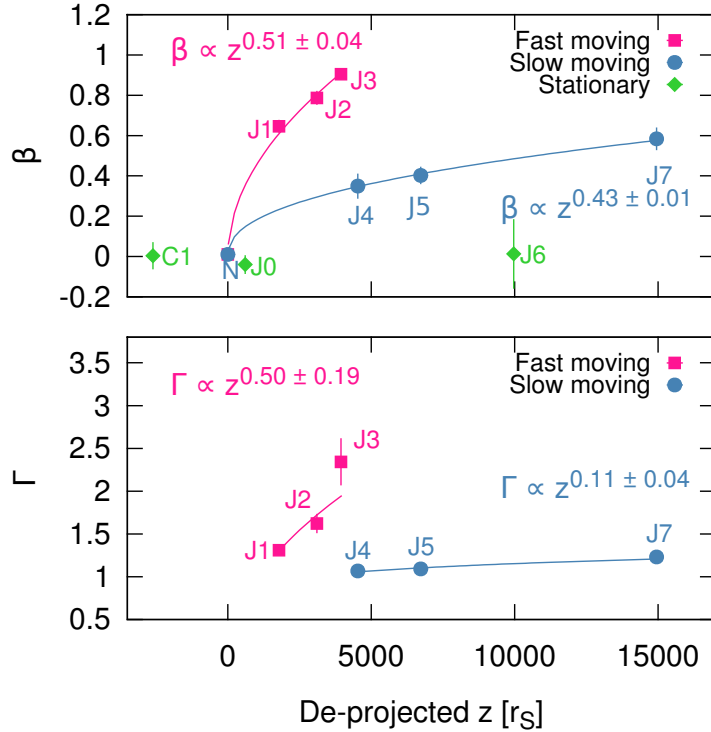


Figure 4.8: **Top** - Intrinsic speed as a function of de-projected core separation. A fast and a slow component with different acceleration gradients can be identified. **Bottom** - Corresponding Lorentz factor versus de-projected core-separation.

quite slowly. The steeper gradient of speed which we measure for the fast flow (central spine) compared to the slow one (sheath) indicates that the conversion to kinetic energy proceeds faster for sections of the flow which are closer to the jet axis. By fitting a power law (Fig. 4.8, top) we find $\beta \propto z^{0.51 \pm 0.04}$ for the former, and $\beta \propto z^{0.43 \pm 0.01}$ for the latter. This translates into a quite different behavior of the Lorentz factor (Fig. 4.8, bottom), whose dependence on the core separation is $\Gamma \propto z^{0.50 \pm 0.19}$ and $\Gamma \propto z^{0.11 \pm 0.04}$ for the fast and slow flow respectively.

4.5.2 Mean opening angle

From our study, other important physical parameters of the flow, like the shape and opening angle, can be estimated. From the analysis of the transverse structure (Sect. 4.3.2), we can infer the dependence of the jet width on the core separation. It is preferable in this case to take into account not the stacked map but the single images, as this prevents the temporal evolution of the ridge line from affecting the results. Here we present our findings for the last epoch, November 2009, which is the one showing most prominently the double ridge

line structure. The jet width was calculated for each slice as the separation between the edges of the two (de-convolved) FWHM. The results are shown in Fig. 4.9, where the de-convolved widths obtained from a single-Gaussian slice fit are plotted for comparison, and show good agreement. This indicates that the expansion of the two ridge lines coincides well with the overall expansion of the jet. We also plot the widths obtained from the modelfit analysis of all the four observing epochs. With some exceptions (discussed below) there is again a substantial overlap. The jet width is clearly increasing both in jet and counter-jet up to approximately 2 mas from component N (at $z = 0$ in the plot). By performing a linear fit in this region ($|z| < 2$) we can calculate the mean apparent full opening angle ϕ_{app} , increased relative to the intrinsic one ϕ by a factor $1/\sin \theta$ due to projection. In jet and counter-jet we obtain respectively:

$$\phi_j^{\text{app}} = 10.2^\circ \pm 0.3^\circ, \quad \phi_{cj}^{\text{app}} = 4.8^\circ \pm 0.4^\circ \quad (4.5.1)$$

which for $\theta = 74.5^\circ$ correspond to intrinsic opening angles:

$$\phi_j = 9.8^\circ \pm 0.3^\circ, \quad \phi_{cj} = 4.7^\circ \pm 0.4^\circ \quad (4.5.2)$$

As found also in [Krichbaum et al. \(1998\)](#) at 22 GHz, the jet appears about two times broader than the counter-jet. Following the classical assumption of intrinsic symmetry, the apparent opening angle should in principle be the same in jet and counter-jet, unless they are strongly misaligned. Although a small misalignment is present both on pc and kpc scales, this is not enough to justify the observed difference. A possible explanation could be the different SNRs of the approaching and receding sides, with the counter-jet being considerably dimmer than the jet at the same core separation and thus detectable over a narrower section. Also, we note that there is, in this case, a certain discrepancy between the modelfit size of C1 and the corresponding width of the intensity profile, with the first being larger and closer to the width of the jet side. This is probably an effect from the smaller beam used in the slicing and it suggests that the counter-jet emission is less compact than the jet emission. However the hypothesis of intrinsic asymmetry, indeed possible (e.g [Fendt & Sheiknezami 2013](#)), cannot be excluded.

As was also found in other radio galaxies on parsec-scale, the opening angles in Cygnus A are anyhow considerably larger than in blazars, in which intrinsic opening angles of $\sim (1 - 2)^\circ$ are typically measured ([Pushkarev et al. 2009](#)). This result represents another piece of evidence for the spine-sheath scenario, in which sources seen at larger viewing angles become more and more sheath-dominated, and therefore broader, while the emission from blazars mostly comes from the strongly boosted, thin spine.

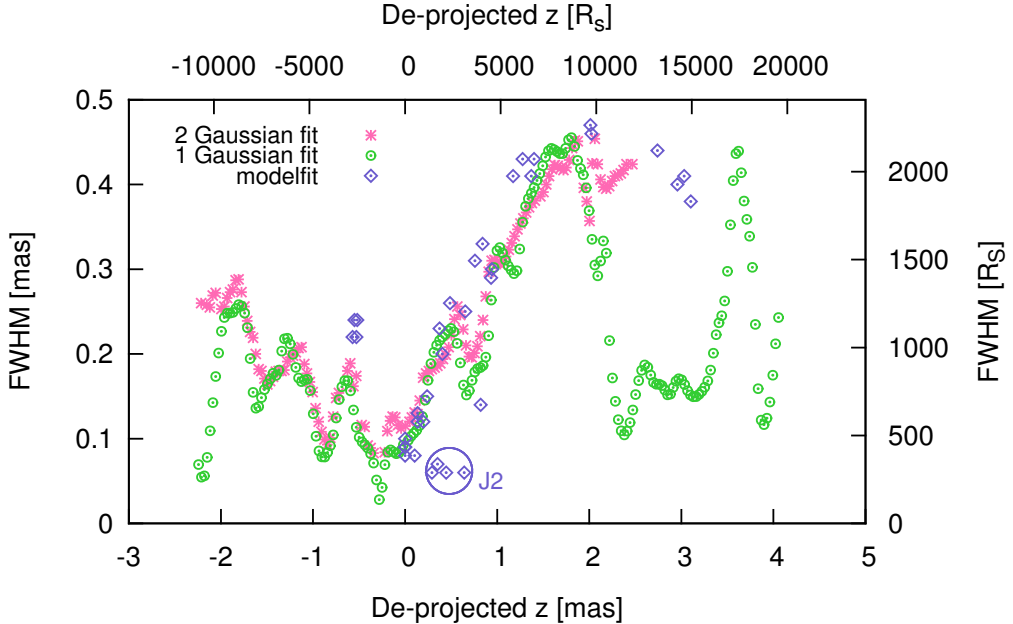


Figure 4.9: Jet aperture versus core separation in November 2009 from the double ridge line analysis (magenta), from a single Gaussian fit (green). Overplotted in blue are the sizes of the modelfit components from all epochs. Note that component J2 occupies only a portion of the jet in the transverse direction.

4.5.3 Narrowing of the jet at $z \sim 2$ mas

The increase of the jet width is not always smooth, but is characterized by some oscillations. Although an oscillating expansion can occur in jets (Daly & Marscher 1988), we cannot exclude that this is an image artifact, especially in the faint regions of the counter-jet. The narrowing at ~ 2 mas in the main jet, and perhaps in the counter-jet too is, however, very prominent and coincides with the location of the stationary feature J6. Stationary features in jets can be related to instability patterns, as mentioned in Sect. 4.4.2, or may result from re-collimation mechanisms. In the purely hydrodynamic case, recollimations naturally occur when the expanding flow becomes under-pressured compared to the medium (Daly & Marscher 1988). In MHD flows, collimation features can also appear when the jet ceases to be strongly magnetized and causally connected to the central engine (Meier 2012). The transition to the new regime is possibly accompanied by a saturation of the acceleration, which is nevertheless not observed in this region. Kinematic VLBI studies at lower frequencies (Bach et al. 2003, and references therein) have shown that the acceleration in the main jet extends at least to ~ 5 mas, where another prominent narrowing appears (Krichbaum et al. 1998). The nature of this collimation feature is ultimately not clear. It is interesting though that the narrowing is not present if we look at the modelfit widths (Fig. 4.9). In other words, the larger beam used in the modelfit analysis does not “see” the feature,

indicating that whatever process is taking place, it must involve the flow on smaller scales.

4.5.4 Collimation regime

Theoretical models and simulations describing the conversion from Poynting flux to kinetic flux in magnetically-driven jets have shown that the characteristics of the external medium represent a fundamental parameter (Komissarov et al. 2007; Tchekhovskoy et al. 2008; Lyubarsky 2009). Specifically, the gradient of the external pressure along the jet largely determines the shape of the jet and the acceleration rate, which are intimately connected. In an analytical study of the asymptotic structure of magnetically-driven flows, Lyubarsky (2009) predicts the existence of two main regimes. In the first, the equilibrium regime, the pressure of the external medium p decreases slowly, as $p \propto z^{-k}$ with $k < 2$. In these conditions the magnetic field in the flow succeeds in keeping a strong poloidal component. The jet radius r as a function of distance from the core is then given by a power law with index smaller than 0.5, the Lorentz factor increases as the radius ($\Gamma \propto r$) and the asymptotic shape of the jet is cylindrical. If the pressure gradient is steeper, with index $k > 2$, the poloidal magnetic field becomes negligible, while the toroidal component cannot provide strong confinement to the flow, which then gets broader, accelerates more slowly ($\Gamma \propto z/r$), and eventually reaches a conical shape. This is the non-equilibrium regime. The transition state between the two regimes occurs for $k = 2$. In this case, the asymptotic behavior of the flow is determined by the intensity of the magnetic field B_0 and by the external pressure p_0 at the base of the flow. Specifically, if the ratio $(6\pi p_0)/B_0^2$ is larger than 0.25, the flow has characteristics similar to the first regime, and has a perfectly parabolic shape, i.e. with a radius r increasing as $z^{0.5}$. A smaller ratio instead leads the flow to a state similar to the second regime. In the following, we show that Cygnus A resembles the properties expected in the transition state ($p \propto z^{-2}$) and that the asymptotic regime is that of equilibrium. Let us consider the shape of the jet. Because of the higher SNR, we focus our analysis on the approaching side. In order to reduce the impact of small scale oscillations and to study the overall expansion of the jet, we consider the jet width as derived from the model fitting in the four epochs up to the narrowing at ~ 2 mas. We exclude component J2 because, as shown in Fig. 4.10, this is clearly a feature occupying, transversally, only a portion of the jet. Results are shown in Fig. 4.10. The expansion can be described by a single power law of the form $r \propto z^{0.55 \pm 0.07}$ up to $\sim 10^4 R_S$, i.e. the jet has a parabolic shape. Two elements suggest that the flow collimates in the equilibrium regime. Firstly, the Lorentz factor gradient of the fast component calculated in Sect. 4.5.1 ($\Gamma \propto z^{0.50 \pm 0.19}$) is compatible with the prediction that Γ grows as r , at least in the central body of the jet. Secondly, VLBI studies at 5 GHz

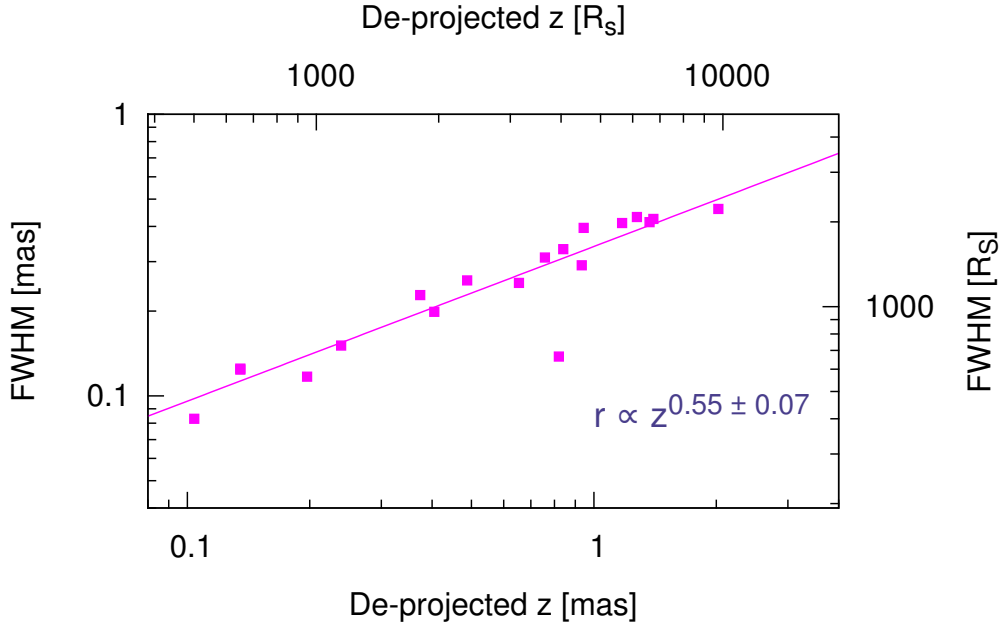


Figure 4.10: Power-law fit of the jet width ($\text{FWHM}=2^*\text{radius } r$) versus de-projected distance from the core, as inferred from MODELFIT.

(Carilli et al. 1991) showed that the jet has a cylindrical shape between 4 and 20 mas, which is the asymptotic state in the equilibrium regime. Interestingly, 4–5 mas ($\sim 2.5 \times 10^4 R_S$) is also the maximum scale on which acceleration has been observed in this source (Bach et al. 2003), and where a second, prominent recollimation occurs (Krichbaum et al. 1998). Therefore this location can be identified as a good candidate for a region where the jet of Cygnus A ceases to be strongly magnetized and becomes causally disconnected from the central engine.

4.5.5 Comparison with M87

In the previous section we have shown that the prototypical FRII radio galaxy Cygnus A is collimated and accelerated on a scale of $\sim 2.5 \times 10^4 R_S$, with the jet being parabolic in this region and cylindrical further downstream. It is interesting to compare these properties with those inferred for M87, the most studied FRI object. Asada & Nakamura (2012) have shown that the jet of M87 is also parabolic up to a scale of $\sim 10^5 R_S$, with $r \propto z^{0.59}$, thus with a power law index very close to that we measure for Cygnus A. However, after the HST-1 feature, the jet becomes conical rather than cylindrical, just as expected in the non-equilibrium regime. An important difference between the equilibrium and non-equilibrium regimes resides in the efficiency of conversion of Poynting flux. While in the former case the Poynting flux will be mostly converted into kinetic flux, until equipartition is reached, a

jet in non-equilibrium will remain magnetized up to large distances without reaching very high Lorentz factors. The high power, thin jets of the FRII sources and the lower power, broader jets of the FRIs appear to fit well into the two categories respectively, indicating that the FRI/FRII dichotomy might result from different environmental conditions. The discovery of sources with hybrid morphologies ([Gopal-Krishna & Wiita 2002](#)), the so called HYMORS, supports the same scenario.

4.5.6 Nature of the gap of emission

Finally, we comment on the nature of the sharp gap of emission situated at ~ 0.25 mas east of component N and of ~ 0.1 mas in size. Figure 7 shows that, although the origin of the x axis is set to coincide with the location of component N, this is not the most narrow region of the jet. Instead, both jet and counter-jet appear to emanate exactly from the gap of emission, which features the absolute minimum width. It is then likely that the gap marks the true location of the central engine, which would then be located $\sim 1000 R_S$ upstream of the jet base, represented by component N. Given the amount of evidence for the jet being magnetically driven, it is interesting to wonder how the jet would appear when it is still completely magnetically dominated, i.e. with a magnetization parameter much larger than 1. Due to the very low speed the flow would have, it would also be faint and may appear as a gap. Other explanations are of course possible. The gap could alternatively result from strong absorption by a molecular torus, which is certainly present and obscures part of the counter-jet ([Struve & Conway 2010](#)). Another possibility is that this is simply a self-absorbed region. A detailed spectral analysis aimed at clarifying the nature of this feature is presented in Chapter 6.

4.6 Conclusions

We have performed a high resolution VLBI study at 7 mm of the kinematic properties and transverse structure of the two-sided jet in Cygnus A. Results can be summarized as follows.

- We detect an acceleration of the flow up to superluminal speeds ($\beta_{\text{app}}^{\max} = 1.15 \pm 0.04$) in the first parsec of the jet. The outer jet exhibits lower speeds, in agreement with studies at lower frequencies. We suggest that a fast and a slow component exist in the flow, and interpret the slower speeds in the outer jet as an effect from the de-boosting of the fast component, naturally occurring at large viewing angle.
- The acceleration region of both the fast and slow component is extended ($\sim 10^3 - 10^4 R_S$), as characteristically predicted for magnetically-driven outflows.

- Both jet and counter-jet are limb brightened. In the presence of a transverse gradient of the bulk Lorentz factor, the limb brightening is evidence for a spine-sheath structure of the jet, as any fast flow appears faint at large viewing angle.
- The mean opening angles in the two sides are large (the full angle in the jet is $\sim 10^\circ$) compared to typical values inferred for blazars ($1^\circ - 2^\circ$). This can be explained by the possibility, in radio galaxies, to observe not only the thin inner spine but also the outer sheath.
- The shape of the flow is parabolic ($r \propto z^{0.55 \pm 0.07}$). The acceleration gradients and the collimation regime can be well reproduced by assuming an external pressure p which scales with distance from the central engine z as $p \propto z^{-2}$, and the ratio $(6\pi p_0)/B_0^2$ to be larger than 0.25 at the base of the flow, as described in [Lyubarsky \(2009\)](#).
- The jet stops being strongly magnetized possibly on a scale of $\sim 2.5 \times 10^4 R_S$, where it enters the asymptotic cylindrical shape ([Carilli et al. 1991](#)), the bulk of the acceleration saturates ([Bach et al. 2003](#)) and a recollimation occurs ([Krichbaum et al. 1998](#)).

Chapter 5

GMVA observations

The study of Cygnus A at the frequency of 43 GHz (Chapter 4) has revealed interesting properties of the jets on sub-parsec and parsec scales: the flow is accelerating and collimating and it is prominently stratified. The nuclear region is however still unresolved at 43 GHz, which prevents us from answering important questions related to the physical properties of the central engine. Where is the central engine located in Cygnus A and what is its size? Is the observed limb-brightening a direct consequence of the jet formation mechanism or it is a feature the jet develops after some distance? In the present Chapter we are going to zoom in further into the very core of Cygnus A through the analysis of maps at 86 GHz obtained from GMVA observations. The data set is presented in Sect 5.1. GMVA observations allow an angular resolution down to $\sim 45\mu\text{as}$ to be achieved, which for Cygnus A translates into a linear scale of only ~ 200 Schwarzschild radii. With this enhanced resolution, we would first of all like to confirm the jet structure observed at 43 GHz, and especially verify if the “gap of emission” from which the jets appear to emanate is also visible at this higher frequency. In the previous Chapter indeed, the hypothesis that the gap actually marks the location of the central engine has been proposed. In the following, this scenario is tested through a pixel-based study of lateral intensity profiles (Sect. 5.2), of the the jet transverse size (Sect. 5.4) and of the ridge line (Sect. 5.6). Besides, this analysis provides tools for verifying the acceleration and collimation properties inferred at lower resolution (Chapt. 4). The study of the nuclear regions will be complemented by a spectral analysis, presented in Chapter 6.

5.1 Data set and analysis

In this section, the GMVA data set and the methods adopted for its analysis are presented. The data set comprises 3 epochs from observations in 2009/2010 with a cadence of approximately 6 months. The duration of the observations was of 15-16 hours, of which ~ 8 were spent on the source. This, together with the large number of antennas employed (Tab. 5.1.1) enabled to achieve a good uv-coverage. As done during the observations at 43 GHz, the nearby calibrator J2015+3710 was frequently observed, with the main purpose of carrying out pointing scans at the largest dishes in order to reduce pointing errors. Data were recorded in single polarization mode with a recording rate of 512 Mb/s. The calibration was performed in AIPS following the standard procedures, including fringe fitting, opacity correction for atmospheric attenuation, and bandpass calibration. The imaging and self-calibration of amplitude and phase were performed in DIFMAP. The clean maps obtained are presented in Figure 5.1. In order to more easily compare them, the maps were restored with a common circular beam of 0.1 mas. The images restored with the natural beams are presented in Appendix A. The nuclear region is detected with a high signal to noise (between ~ 600 -900), with a core flux of at least 180 mJy/beam and showing a prominent variability over the monitoring period. The counter-jet is also detected in all the three epochs, with a maximum SNR of ~ 60 . The total flux density varies between ~ 0.7 and 0.9 Jy and it is consistent with the measurement of ~ 1 Jy provided by 86 GHz single-dish observations at IRAM ([Agudo et al. 2010](#)). The variation of the flux density during the self-calibration procedure was not larger than $\sim 20\%$, therefore this percentage can be assumed as the uncertainty associated with the flux density measurements. The

Table 5.1.1: Log of observations at 86 GHz (3 mm) and characteristics of the clean maps. Col. 1: Day of observation. Col. 2: Array. VLBA_3mm indicates the part of the Very Long Baseline Array (all but Hancock and St. Croix) which is equipped with 86 GHz receivers; On - Onsala; Eb - Effelsberg; PdB - Plateau de Bure; PV - Pico Veleta. Col. 3: Beam FWHM and position angle. Col. 5: Peak flux density. Col. 6: Noise. All values are for untapered data with uniform weighting.

Date	Array	Beam FWHM [mas, deg]	Recording rate [Mbit/s]	S_{peak} [mJy/beam]	rms [mJy/beam]
08/05/2009	VLBA_3mm, On, Eb, PdB, PV	$0.11 \times 0.05, -2.1^\circ$	512	280	0.3
10/10/2009	VLBA_3mm, On, Eb, PdB, PV	$0.11 \times 0.04, -4.3^\circ$	512	185	0.3
07/05/2010	VLBA_3mm, On, Eb, PdB, PV	$0.11 \times 0.04, -6.5^\circ$	512	268	0.3

map from observations in October 2009 clearly shows the gap of emission at ~ 0.2 mas east of the core, while this is less prominent in the other two epochs. The limb brightening

observed at 43 GHz is also seen at 86 GHz, as it can be already noticed after a visual inspection. It is also apparent, however, that due to the reduced SNR the jets are in some regions not detected over the full cross section. In Figure 5.2, the stacked image of the three epochs is shown, and it is compared with the stacked image at 43 GHz. Apart from some discrepancies in the faint, outer counter-jet, the morphology of the source appears similar at the two frequencies. In the next chapter, the problem of correctly aligning maps at different frequencies is discussed, and different methods are implemented for achieving this goal. Figure 5.2, however, already indicates that at 43 and 86 GHz the images appear already well aligned and no significant shift is necessary. This is particularly evident if looking at the core-gap structure which, although less prominently, is also visible in the stacked image at 86 GHz. In order to study the 86 GHz jet in detail, a pixel-based analysis of the transverse intensity profiles was performed also at this higher frequency, following the same method described in Sect. 4.3.2. The study was repeated with two different circular beam sizes of 0.15 mas and 0.1 mas, choosing a pixel size of 0.03 mas and 0.02 mas respectively, in the first case for better comparing the results with those at 43 GHz, and in the second for enhancing the resolution in the analysis of the nuclear regions.

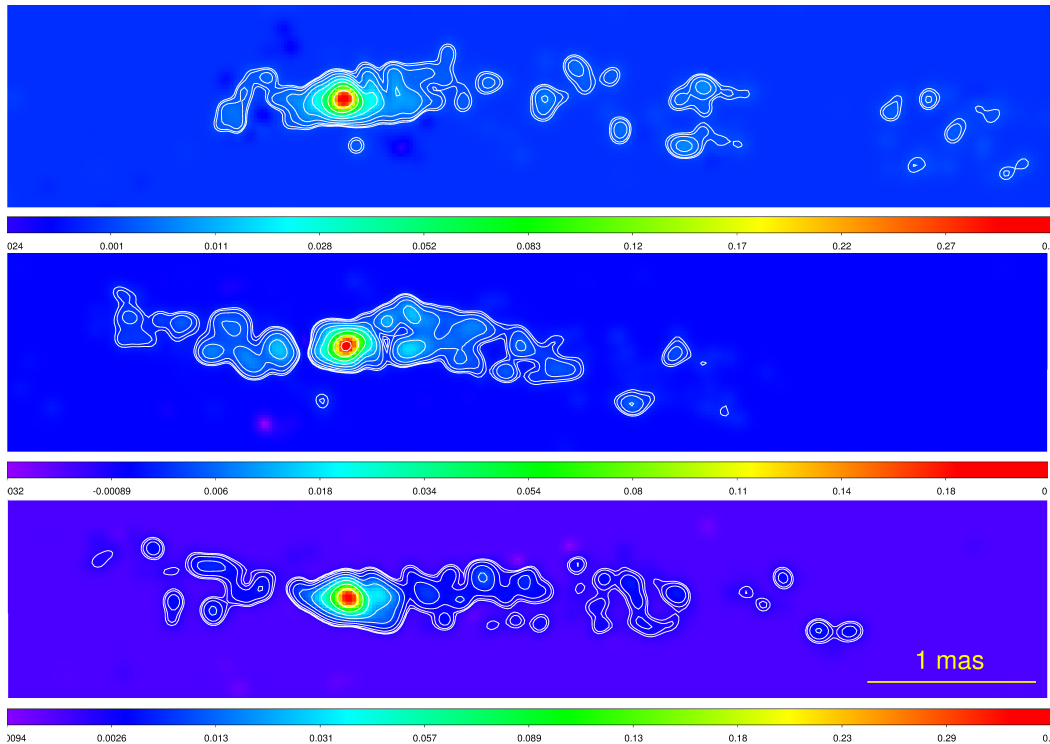


Figure 5.1: Clean maps at 86 GHz from observations in May 2009, October 2009 and May 2010. The alignment is based on the position of the peak of intensity. The maps were restored with a circular beam of 0.1 mas. Contours represent isophotes at 1.5, 4.6, 9.0, 13.4, 17.9, 22.2, 26.7, 31.1, 35.6 mJy/beam. The peak fluxes and the natural beam sizes are reported in Tab. 5.1.1

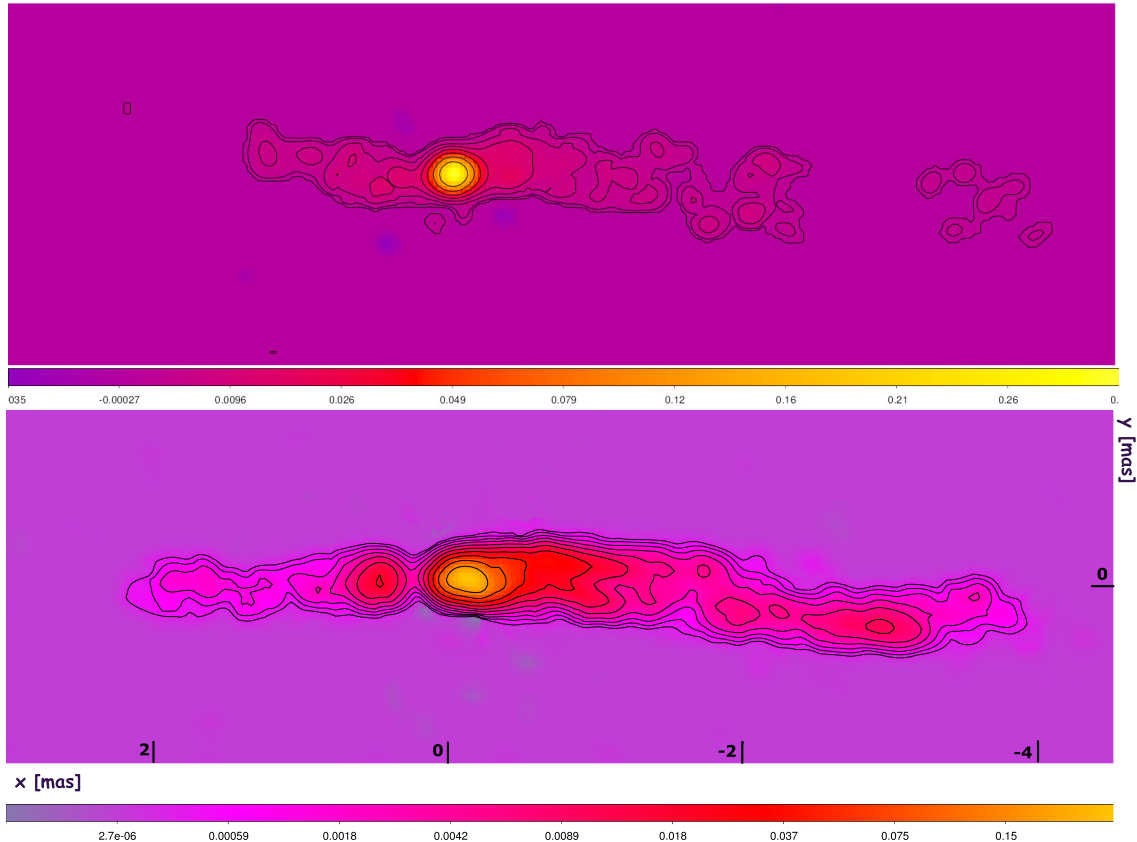


Figure 5.2: Stacked image of Cygnus A at 86 GHz (top) and at 43 GHz (bottom) from observations in 2008-2010. The maps were restored with a common circular beam of 0.15 mas. Contours represent isophotes at 1.2, 2.4, 4.8, 9.6, 19.2, 38.4, 76.8 and 153.6 mJy/beam and at 0.3, 0.6, 1.2, 2.4, 4.8, 9.6, 19.2, 38.4, 76.8 and 153.6 mJy/beam respectively.

5.2 Intensity profiles

The lateral intensity profiles obtained through the analysis of the transverse structure are compared in Fig. 5.2 for the three epochs. The total intensity is clearly dominated by the core emission. The core flux varies significantly during the monitoring, being higher in the first and last epoch, while the rest of the jet and counter-jet are brighter in the middle epoch. As already noticed in the map, the gap of emission at ~ 0.25 mas appears prominently only in October 2009 in the intensity profile. In the hypothesis that the gap hosts the actual central engine, an increased emission at this location may then be interpreted as the result of an ongoing nuclear activity taking place in May 2009 and May 2010. In the following, it is shown that this scenario is in agreement with the observed variability in jet and counter-jet. It should be remembered that a double ejection in the jet and counter-jet side would

not result in a simultaneous brightening of the two sides, due to the difference of the light travel time. In fact, light from the counter-jet has to travel an additional path for reaching the observer, which can be easily estimated. Given two points A and B in jet and counter-jet respectively, the additional path ΔX the light has to travel from point A for reaching the observer is given by:

$$\Delta X \sim \frac{AB}{\sin \theta} \cdot \cos \theta \quad (5.2.1)$$

where $AB / \sin \theta$ is the de-projected separation between A and B and θ is the jet viewing angle. The light travel time difference δt is then $\Delta X/c$. If we take into account the core and the first counter-jet component in October 2009, approximately equidistant with respect to the gap, we estimate a distance AB of ~ 0.43 parsec. By assuming $\theta = 74.5^\circ$, we infer $\Delta x \sim 0.12$ parsec and $\delta t \sim 4.8$ months. Therefore, the radiation from two components emitted simultaneously from the gap region in the two sides and traveling at the same speed would be seen in the jet first and 4.8 months later in the counter-jet. This is very consistent with what we observe. In May 2009 a new component has reached the core location at $x = 0$, which makes the core brighter. In October 2009, i.e. 5 months after, the new counter-jet component becomes visible at $x = 0.4$ mas. The jet component instead has already moved away from the core (which is now dimmer) and it is clearly seen in the last epoch, May 2010, at a separation of ~ 0.2 mas from the core. Ultimately, the analysis of the intensity profiles supports the idea that the flow emanates in the two sides from the gap location.

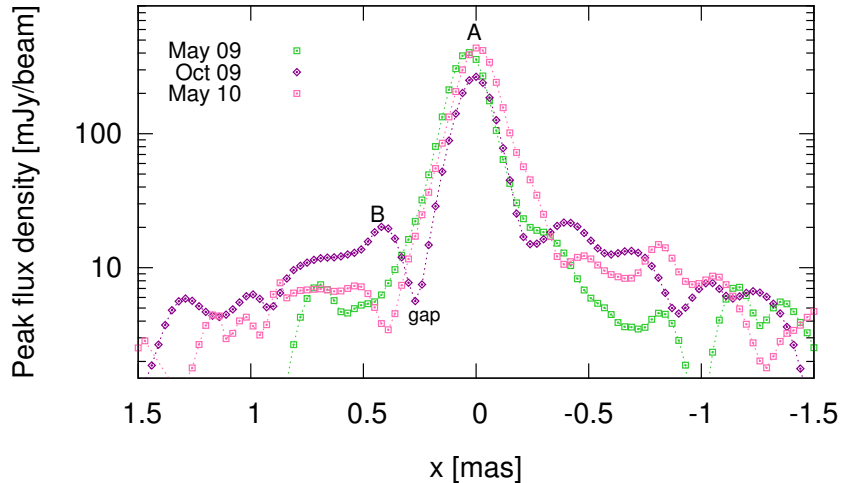


Figure 5.3: Lateral intensity profiles at 86 GHz for May 2009 (green), October 2009 (violet) and May 2010 (magenta). A double ejection from the location of the gap would be visible first in A and 4.8 months later in B due to the difference in the light travel time. This is in agreement with the variability of the core flux and of the first counter-jet component in May 2009 and October 2009.

5.3 Alignment and proper motion

Given the complex and smooth structure of the jets at 86 GHz, the model fitting and the kinematic study at this frequency are difficult. An estimate of the speed of the flow on this scales can be better obtained by examining the intensity profiles, trying to identify a peak and calculating its displacement during the monitoring. The peak position can be determined by fitting a Gaussian profile to each feature. Before doing that, it is however necessary to confirm the maps alignment, in order to refer positions to some point assumed as stationary. At this frequency, the alignment is somewhat easier than at lower frequency because of the higher core dominance. In other words, the core identification is less ambiguous and aligning the maps on the brightest feature appears in this case the most obvious choice. As shown in Fig. 5.2, the maps are already aligned on the brightest pixel in October 2009 and May 2010, while in May 2009 a shift of a single pixel is necessary. The aligned profiles are reported separately in Fig. 5.3. Besides the core, two features in the jet side, labeled as J1 and J2 in figure, appear well defined and show a clear displacement. J1 is visible in all epochs, while J2 is less prominent in the first epoch and well defined in the last two. On the counter-jet side, the intensity profiles indicate that the brightness distribution is changing with time, but the lower SNR does not allow to unambiguously identify any moving feature. Also at 43 GHz only one well defined component could be identified and it appears stationary (Sect. 4.4.1). By performing a linear fit of the distance from the core as a function of time, we obtain an apparent speed β_{app} of 0.66 ± 0.14 for J1 and of 0.97 ± 0.21 for J2 (Tab. 4.3.2). These results are in agreement with the findings from the kinematic analysis at 43 GHz for two components crossing approximately the same region, i.e. J1, moving with a β_{app} of 0.75 ± 0.04 , and J2, traveling at speed 0.96 ± 0.05 (Sect. 4.3.1). Therefore the presence of a parsec scale acceleration of the flow is confirmed at 86 GHz.

Table 5.3.1: Properties of the intensity peaks, as derived from a gaussian fit, and their displacement. Col. 1: Component label. Col. 2: Epoch. Col. 3: Separation from the core. The error is taken equal to one pixel size. Col. 4: Displacement. Col. 5: Apparent speed in units of c .

Comp. ID	Epoch	x [mas]	μ [mas/year]	β_{app}
J1	2009.35	0.29 ± 0.03		
	2009.77	0.40 ± 0.03		
	2010.35	0.47 ± 0.03	0.18 ± 0.04	0.66 ± 0.14
J2	2009.35	-		
	2009.77	0.67 ± 0.03		
	2010.35	0.82 ± 0.03	0.26 ± 0.06	0.97 ± 0.21

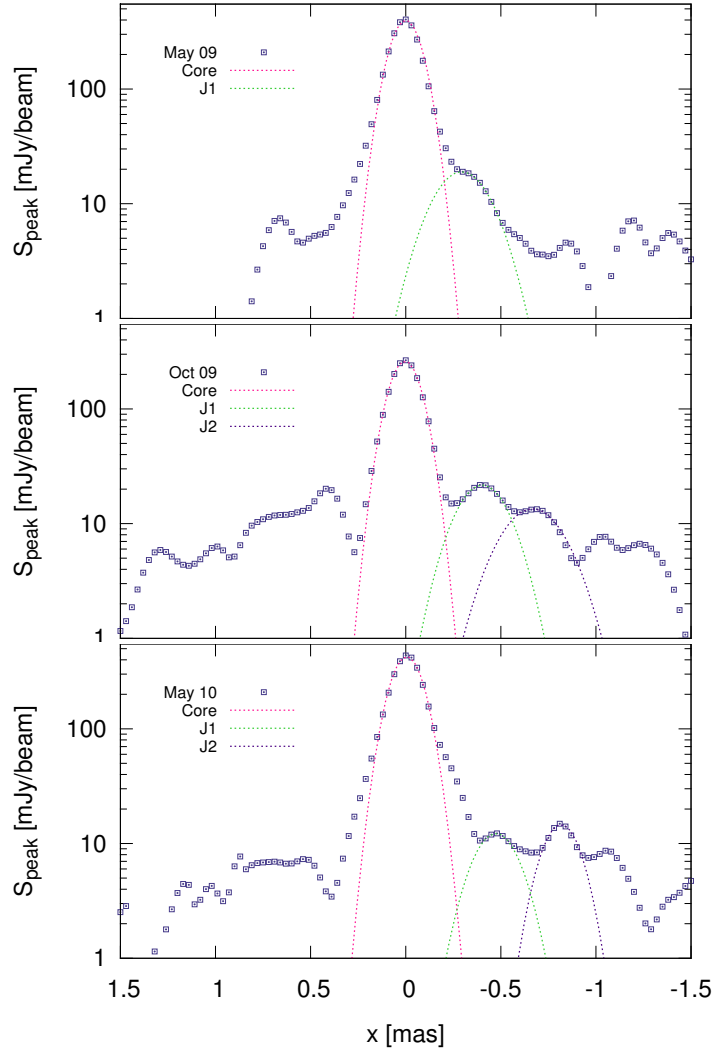


Figure 5.4: Intensity profiles for May 2009 (top), October 2009 (middle) and May 2010 (bottom). A Gaussian fit was performed for describing the main and well defined peaks.

5.4 Width profile and jet origin

The pixel-based study of the jet width constitutes, among other things, an important tool for locating the central engine, and it is especially effective if a counter-jet is detected. Indeed, while in blazars the location of the launching region can only be back-extrapolated based on certain assumptions, e.g. that the jet is conical down to the very base, in radio galaxies one often has the chance to study the symmetry of the source in the two sides, trying to identify “the center of symmetry”, i.e. the central engine as interpreted in the classical unified scheme. Already the study at 43 GHz has shown that the most narrow point of the jet is the gap of emission at 0.2 mas east of the core (Fig. 4.7), from which the

two jets seem to emanate. Observations at 86 GHz allow now to penetrate further into the nuclear regions and to repeat the pixel-based study at higher resolution. It should be noted here that the gap does not feature a zero flux density, it is just much fainter compared to the surroundings. Its flux density of a few milliJanskys is anyhow sufficient for performing a Gaussian fit and determining a transverse width. Figure 5.4 shows, for the three epochs, the dependence of the jets width on the distance from the core in the central ~ 1.5 mas of the source. For clarity, the error bars for each width measurement are not reported in figure, but they can be reasonably assumed equal to 1/5 of each FWHM. Both jet and counter-jet show an oscillating expansion, with a good agreement between different epochs. The lower-resolution analysis using a beam of 0.15 mas (left panel) shows that only the image from May 2010 presents an absolute minimum at the location of the gap, while in the other two this coincides with the core. However, the study at higher resolution (right panel) with a beam of 0.1 mas reveals, although with an higher noise level, that a minimum in the gap location is also present in October 2009, while the profile for May 2009 appears still smooth in this region. Therefore, on the one hand we again find evidence that the jets may be

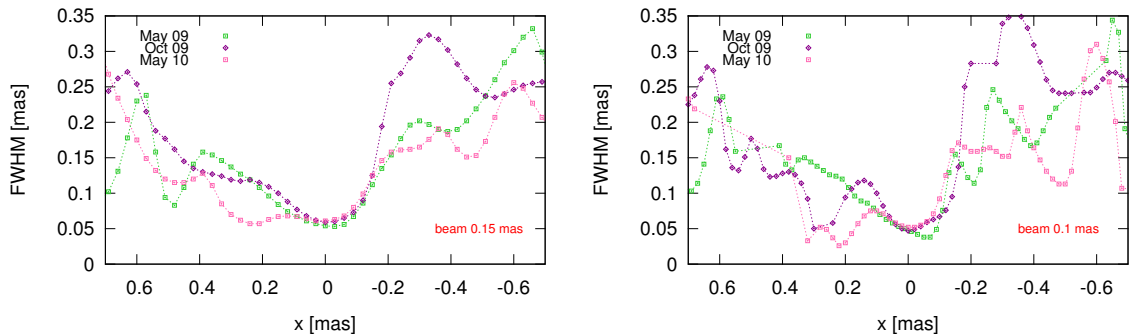


Figure 5.5: Width profiles at 86 GHz for May 2009 (green), October 2009 (violet) and May 2010 (magenta). Error bars for the width measurements, not shown for clarity, are assumed equal to 1/5 of each FWHM.

launched from the gap region, but also we infer that this feature is less pronounced and it manifests only on very small scales at 86 GHz.

Concerning the outer regions of the jets, the results for the width profile are in good agreement with those at 43 GHz. In Figure 5.6 we compare the results for the best maps at the two frequencies, from November 2009 and May 2010 respectively. The morphology of the profile appears remarkably similar, including the prominent narrowing at ~ 2 mas in the approaching jet, which is therefore a persistent feature. The 86 GHz jet looks narrower, especially in the outer region, indicating that part of the emission has been missed in the imaging due to the low signal to noise. The counter-jet instead appears broader than at 43 GHz between ~ 0.5 and 1 mas. The counter-jet in this region is of course very faint, and

errors developed in the imaging process cannot be excluded. We note however that the morphology of this region appears similar in all the three epochs (Fig. 5.1), indicating that a wider section of the counter-jet may actually be visible at 86 GHz.

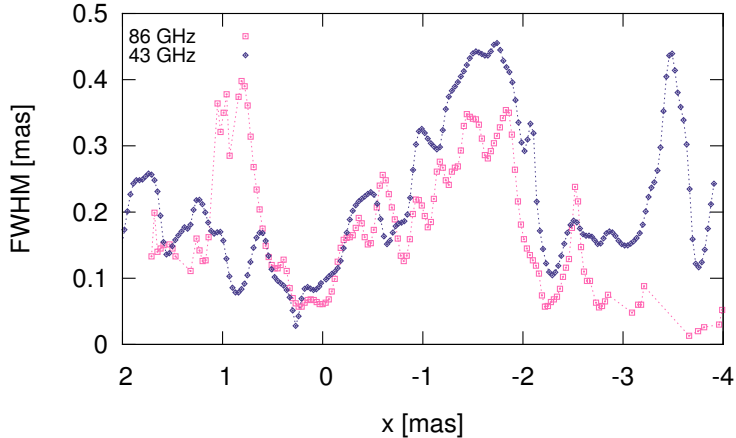


Figure 5.6: Width profiles at 43 GHz for November 2009 (dark blue) and at 86 GHz for May 2010 (magenta).

5.5 Size and structure of the jet base

The discussion in Chapter 2 made clear that magnetic launching, either involving the extraction of rotational energy from the accretion disk ([Blandford & Payne 1982](#), BP) or from the black hole itself ([Blandford & Znajek 1977](#), BZ), is currently favored for explaining the observed properties of relativistic jets. The very results already presented in Chapter 4 for Cygnus A indicate that these jets are magnetically driven. The nature of the launching process can be further investigated through the high resolution study of the nuclear regions at 86 GHz. Specifically, the determination of the size of the jet base is fundamental in the context of discriminating between different jet formation models. This kind of study has been rarely performed in literature, due to fact the jet base is usually not resolved. Even if it is, the location of the VLBI core does not coincide with the true jet base, as the core is often located far away (thousands or millions of Schwarzschild radii) from the black hole. One exception is represented by M87, for which a distance of only $14\text{--}23 R_S$ has been inferred for the 43 GHz core ([Hada et al. 2011](#)). In the same source, experimental VLBI observations at 1.3 mm (with the Event Horizon Telescope) have determined a core size of only $5.5 R_S$ ([Doeleman et al. 2012](#)), meaning that the size of the jet apex is equal to, or smaller than this. The implications of this measurement are important, as they allow the number of possible launching models to be decisively restrained. In Section 1.1.2 the properties of the

Innermost Stable Circular Orbit (ISCO) in accretion disks were presented. Depending on the BH spin, the ISCO radius varies between 1 and $6R_S$ in the case of a prograde motion of the disk and between 7.35 and $9R_S$ for a retrograde motion. For M87, this means that 1) the jet must be anchored close to the ISCO and 2) that retrograde orbits are excluded. In Cygnus A, Fig. 5.5 and 5.6 show that the jet width is nowhere smaller than $\sim 0.028 \pm 0.006$ mas, which is the transverse size of the gap at 43 GHz. The three measurements of the core size at 86 GHz are very consistent, varying between (0.053 ± 0.011) mas, (0.059 ± 0.012) mas and (0.061 ± 0.012) mas. Wherever the central engine is situated, either in the gap or closer to the 86 GHz core, the jet width is nowhere smaller than $135 \pm 27R_S$. The implication is that, no matter what is the BH spin or what kind of orbit the BH+accretion disk system features, the diameter of the ISCO is smaller than the minimum width we measure. The conclusion is that the jet launching region appears to involve the outer part of the accretion disk, i.e. that the [Blandford & Payne \(1982\)](#) mechanism is at play. Note that this fact does not lead to exclude the rotational energy of the black hole from the possible power sources of the jets in Cygnus A. Different studies (e.g. [Hardee et al. 2007](#); [Xie et al. 2012](#)) have suggested that both the BP and BZ mechanism may act simultaneously in relativistic jets, with the external sheath being ejected from the accretion disk and the central spine being fueled from the ergosphere. In a jet seen at large viewing angle, like the one of Cygnus A, it is not surprising that the slower disk wind would dominate the emission, as it was discussed in depth in the previous chapter. If this scenario is correct, the transverse gradient of the bulk Lorentz factor deduced from the kinematic analysis would be an intrinsic property of the jet since its birth, and also the limb-brightened structure would develop very soon. At 43 GHz, the transverse resolution was not sufficient for clearly detecting a double ridge line in the nuclear region. The ridge line analysis was then repeated at 86 GHz and the results are shown in Figure 5.7 for October 2009. Using a beam of 0.1 mas, the ridge line is now detected along almost the entire source and also in the nuclear region, with few exception likely due to the low SNR of either one of the two rails. It seems then unlikely that limb brightening is related to Kelvin-Helmholtz instabilities, which would require a certain time (distance) for developing.

5.6 Conclusions

In this Chapter results from a pixel based analysis of three maps at 86 GHz jets were presented. The main findings can be summarized as follows:

- The transverse structure and the kinematic properties deduced from the study at 43 GHz are confirmed. The jet is accelerating on parsec scales and is limb-brightened.

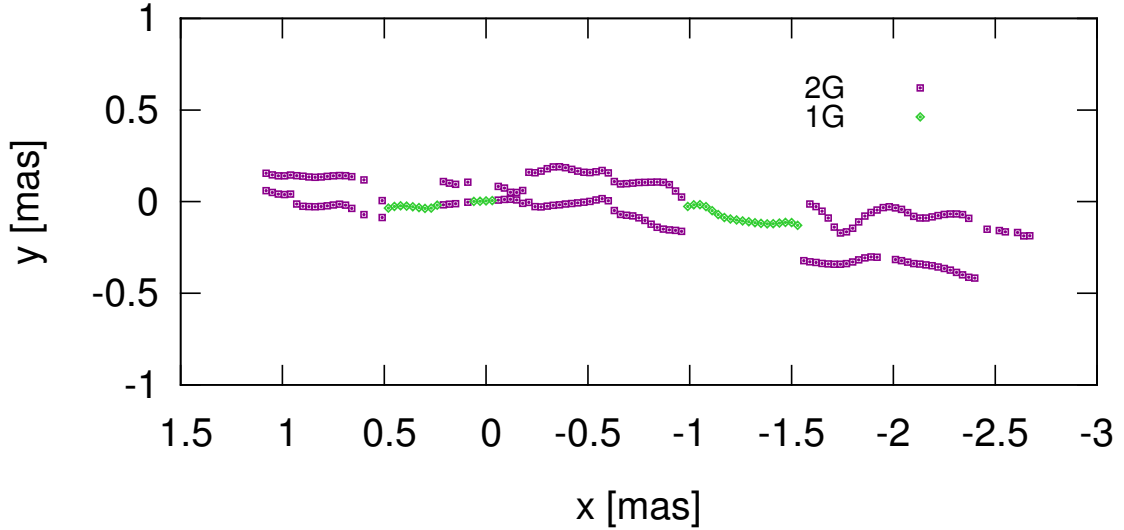


Figure 5.7: Double ridge line at 86 GHz relative to the map from October 2009.

- The observed variability of the lateral intensity profiles is consistent with the two jets emanating from the gap of emission at 0.2–0.3 mas to the east of the core, which would then be the location of the true central engine.
- The gap has a size depending on frequency and on the beam used for restoring the image, and it is less prominent at the higher frequency of 86 GHz.
- The jet width appears nowhere smaller than $135 \pm 27 R_S$. Since this size is larger than any possible ISCO radius, we conclude that the outer accretion disk must be involved in the jet launching. The co-existence of the BP and BZ mechanisms is however not excluded, as a fast spine launched from the ergosphere would be invisible due to Doppler de-boosting.
- The jets appear limb-brightened in most of the nuclear region, suggesting that the jet is intrinsically stratified since its very origin.

Chapter 6

High-resolution spectral study

6.1 Introduction

The last Chapter of this thesis is dedicated to a multi-frequency study of the jets in Cygnus A, using VLBI data in the frequency range 8 GHz - 86 GHz. A first motivation for this work is related to the uncertainty on the location of the true central engine. Although the results in Chapter 4 and 5 have suggested that the “gap of emission” is a good candidate location of the supermassive black hole in Cygnus A, a solid evidence is still missing. The spectral analysis is one of the best tools for testing this hypothesis, especially if high frequency VLBI data are available. Indeed, VLBI at high frequency provides the double advantage of an extremely small observing beam and of an expectedly much reduced synchrotron opacity. Therefore it should be possible to study with great detail the spectral properties at the base of the jets. Secondly, this analysis aims at probing the presence of an absorbing material in the surroundings of the nuclear regions. As explained in Sect. 1.1.4, a torus or an ensemble of clouds with some other geometry are a fundamental ingredient of the unified model for AGN. In type II sources the torus manifests itself by heavily obscuring the activity of the central AGN, also preventing the detection of broad emission lines from the BLR. Although Cygnus A is considered a prototypical type II source for its orientation close to the plane of the sky and for the detection of broad emission lines in polarized light (Antonucci et al. 1994), direct evidence for the presence of a dense obscuring material is still scarce. On parsec scale, previous VLBI studies (e.g. Krichbaum et al. 1998) have revealed a frequency-dependence of the jet-to-counter-jet ratio, pointing towards an absorption of the counter-jet emission at lower frequencies. Recently, VLBI studies of HI absorption (Struve & Conway 2010) have shown the presence of a circumnuclear disk with a radius of ~ 80 pc oriented approximately perpendicular to the jet axis. However, several searches for molecular absorption, tracing more compact regions, have failed, including those for the

CO lines (see e.g. Curran et al. 2011, and references therein). The VLBI spectral analysis at high radio frequencies presented in the following enables to test the existence of the dense component of the absorber on scales which are unreachable by other instruments. A large part of this Chapter (Section 6.3) is dedicated to the methods employed for correctly aligning maps at different frequencies. Indeed, as explained in Sect. 1.3.3, the location where the jet becomes optically thin and therefore bright is frequency-dependent, shifting closer to the jet base as the frequency increases.

6.2 The multi-frequency data set

When comparing images at different frequencies, it is important to take into account data from close in time observations. This is not only true for blazars, which show the most extreme variability, but also for some radio galaxies. Cygnus A represents one example of a variable radiogalaxy. Therefore, a data set formed by pairs of quasi-simultaneous epochs was selected, covering a broad range of frequencies from 8 GHz to 86 GHz with a total of 8 images. The log of observations and the properties of the clean maps are reported in Tab. 6.2.1. The maps at 8 GHz and 15 GHz are part of the Mojave observational campaign, while higher frequencies data were obtained through dedicated proposals. Among these, the proposal for the 43/22 GHz data from the year 2014 was written as a part of this PhD project. In the following, the 8 clean maps of Cygnus A are presented (Fig. 6.1 - 6.8).

Table 6.2.1: Log of observations and characteristics of the clean maps forming the multi-frequency data-set. Col. 1: Epoch reference number. Col. 2: Frequency. Col. 3: Date of observation. Col. 4: Array. VLBA - Very Long Baseline Array; VLBA_3mm indicates the part of the Very Long Baseline Array (8 of the 10 antennas) which is equipped with 86 GHz receivers; GBT - Green Bank Telescope; On - Onsala; Nt - Noto; Eb - Effelsberg; Ys - Yebes; PdB - Plateau de Bure; PV - Pico Veleta. Col. 5: Beam FWHM and position angle. Col. 6: Peak flux density. Col. 7: Noise. All values are for untapered data with uniform weighting.

n.	Freq. [GHz]	Date	Array	Recording rate [Mbit/s]	Beam FWHM [mas, deg]	S_{peak} [mJy/beam]	rms [mJy/beam]
1	8.1	15/06/2006	VLBA	128	$1.61 \times 1.19, 5.1^\circ$	487	0.3
2	15.4	15/06/2006	VLBA	128	$0.74 \times 0.53, -14.7^\circ$	560	0.7
3	15.4	19/11/2008	VLBA	512	$0.69 \times 0.47, -8.0^\circ$	467	0.3
4	43.2	16/10/2008	VLBA*, GBT, On, Nt, Eb, Ys	512	$0.22 \times 0.10, -11.0^\circ$	264	0.1
5	22.2	31/05/2014	VLBA, Eb	2048	$0.40 \times 0.19, -21^\circ$	232	0.1
6	43.1	31/05/2014	VLBA, Eb	2048	$0.23 \times 0.10, -24^\circ$	147	0.1
7	43.1	19/11/2009	VLBA*, GBT, On, Nt, Eb	512	$0.19 \times 0.10, -20.1^\circ$	226	0.3
8	86.2	10/10/2009	VLBA_3mm, On, Eb, PdB, PV	512	$0.11 \times 0.04, -4.3^\circ$	185	0.3

*Saint Croix data not available.

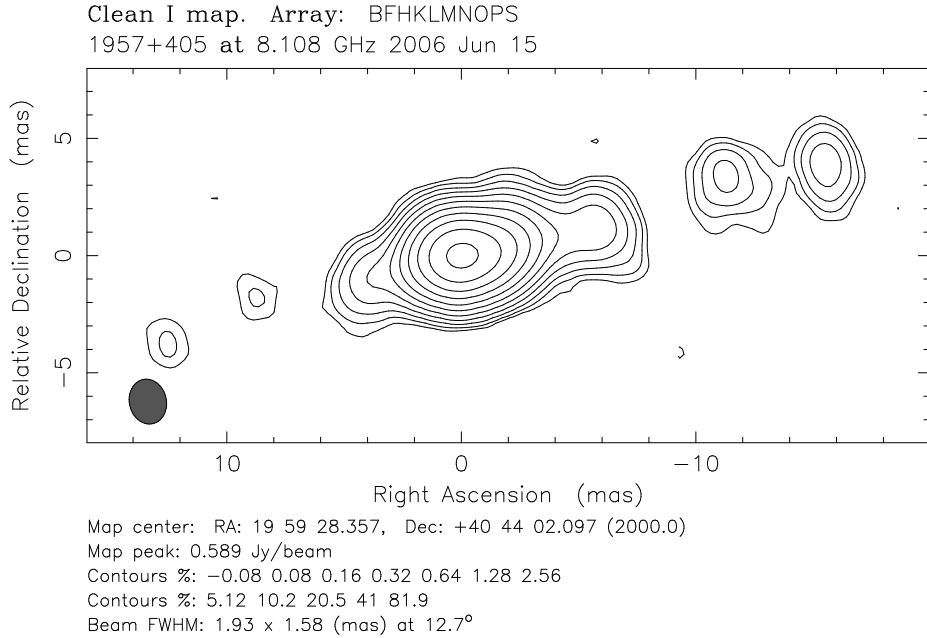


Figure 6.1: Clean map of Cygnus A at 8 GHz from VLBA observations in June 2006 (Mojave survey). A taper of 0.1 at a uv-radius of $200 M\lambda$ was applied. Further information is reported in Tab. 6.2.1 (ref. no. 1).

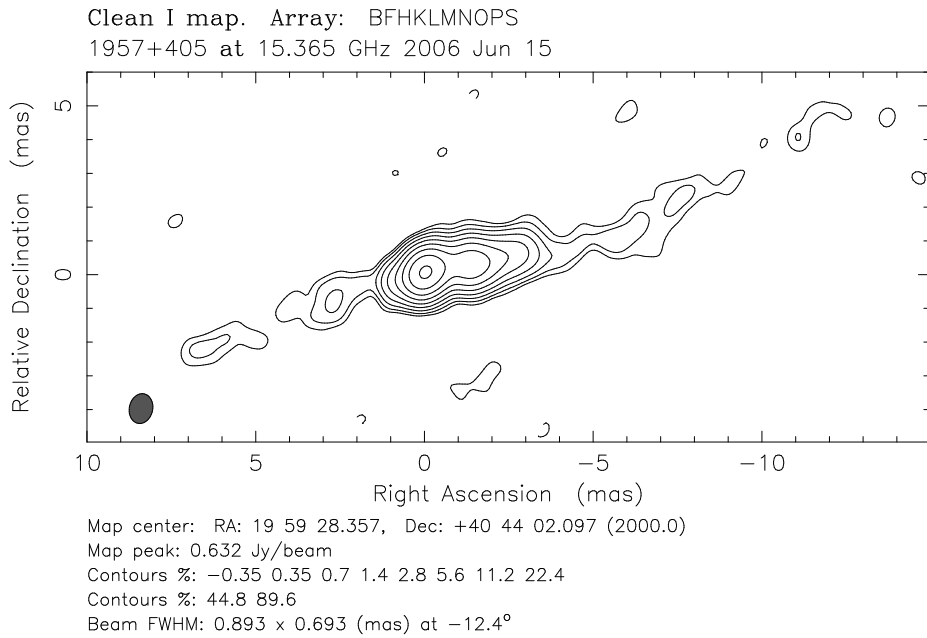


Figure 6.2: Clean map of Cygnus A at 15 GHz from VLBA observations in June 2006 (Mojave survey). A taper of 0.1 at a uv-radius of $400 M\lambda$ was applied. Further information is reported in Tab. 6.2.1 (ref. no. 2).

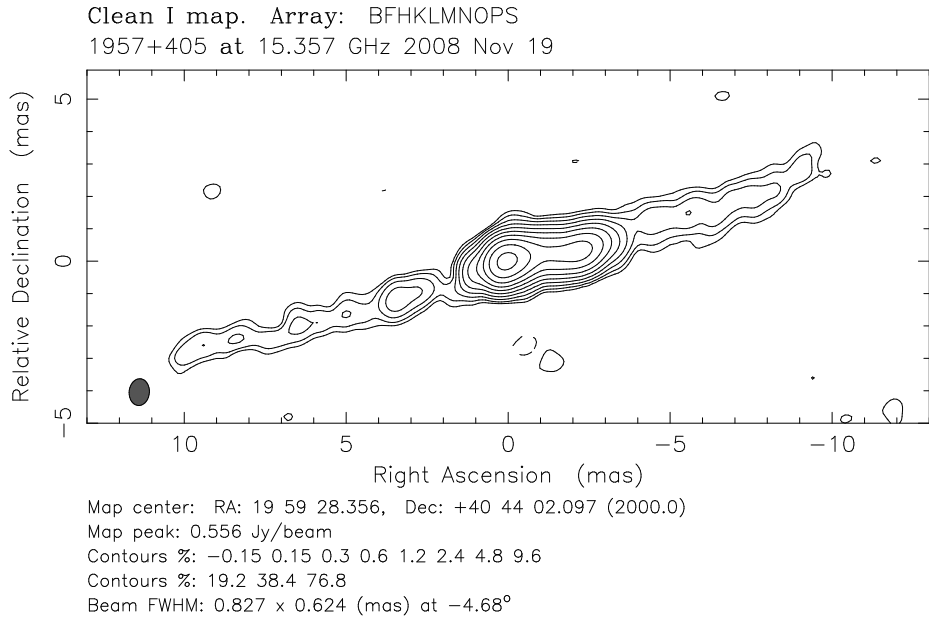


Figure 6.3: Clean map of Cygnus A at 15 GHz from VLBA observations in November 2008 (Mojave survey). A taper of 0.1 at a uv-radius of $400 M\lambda$ was applied. Further information is reported in Tab. 6.2.1 (ref. no. 3).

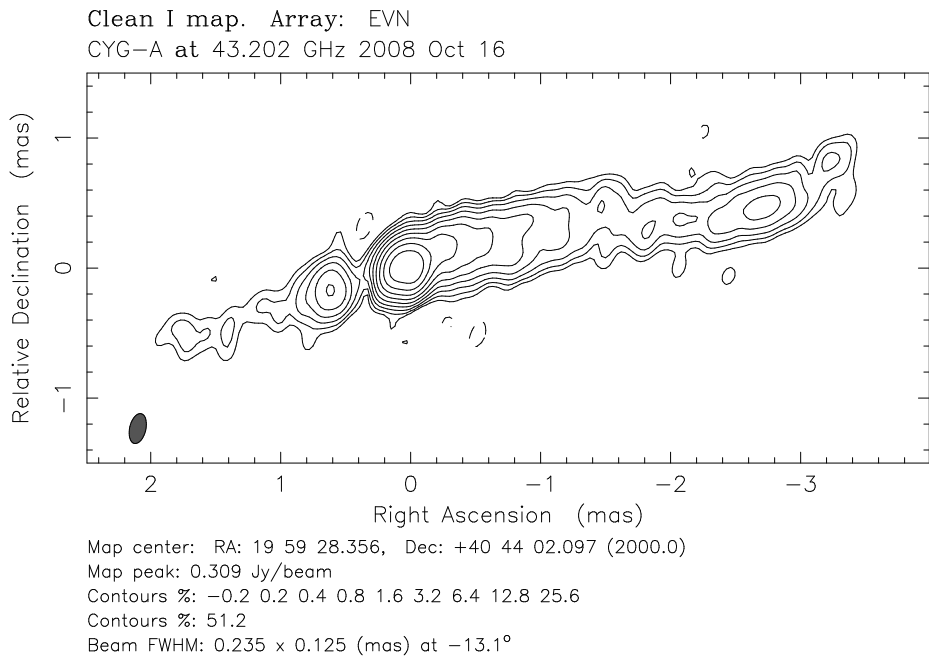


Figure 6.4: Clean map of Cygnus A at 43 GHz from Global VLBI observations in October 2008. A taper of 0.1 at a uv-radius of $1400 M\lambda$ was applied. Further information is reported in Tab. 6.2.1 (ref. no. 4).

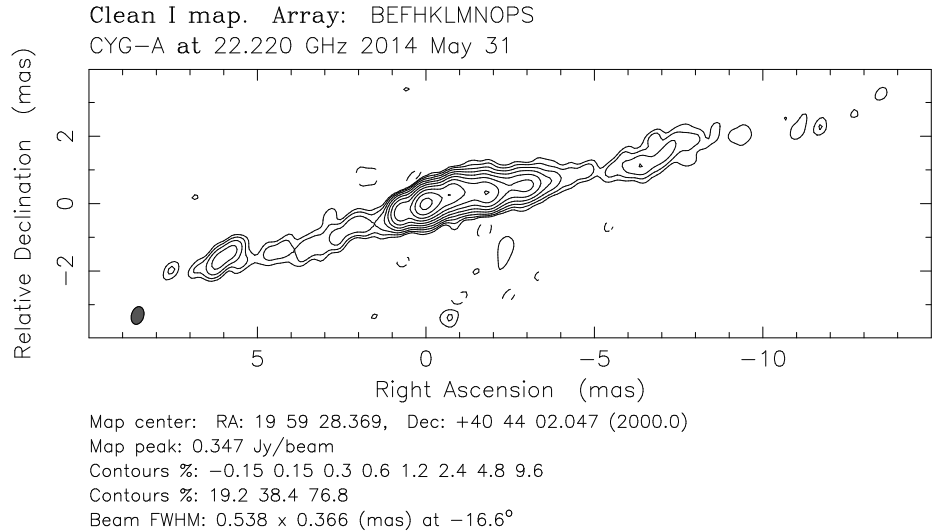


Figure 6.5: Clean map of Cygnus A at 22 GHz from VLBA+Effelsberg observations in May 2014. A taper of 0.1 at a uv-radius of $500 M\lambda$ was applied. Further information is reported in Tab. 6.2.1 (ref. no. 5).

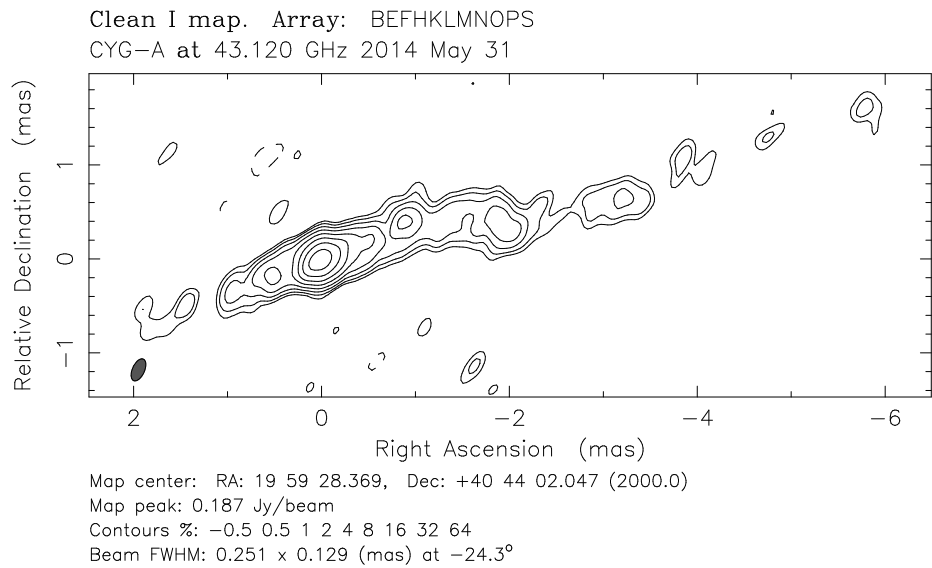


Figure 6.6: Clean map of Cygnus A at 43 GHz from VLBA+Effelsberg observations in May 2014. A taper of 0.1 at a uv-radius of $1400 M\lambda$ was applied. Further information is reported in Tab. 6.2.1 (ref. no. 6).

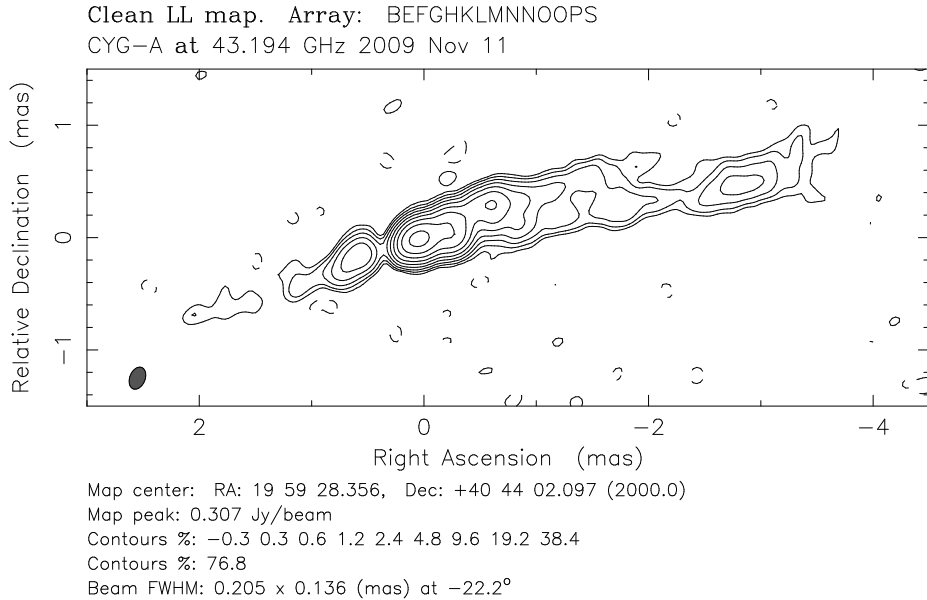


Figure 6.7: Clean map of Cygnus A at 86 GHz from Global VLBI observations in November 2009. A taper of 0.1 at a uv-radius of $1400 M\lambda$ was applied. Further information is reported in Tab. 6.2.1 (ref. no. 7).

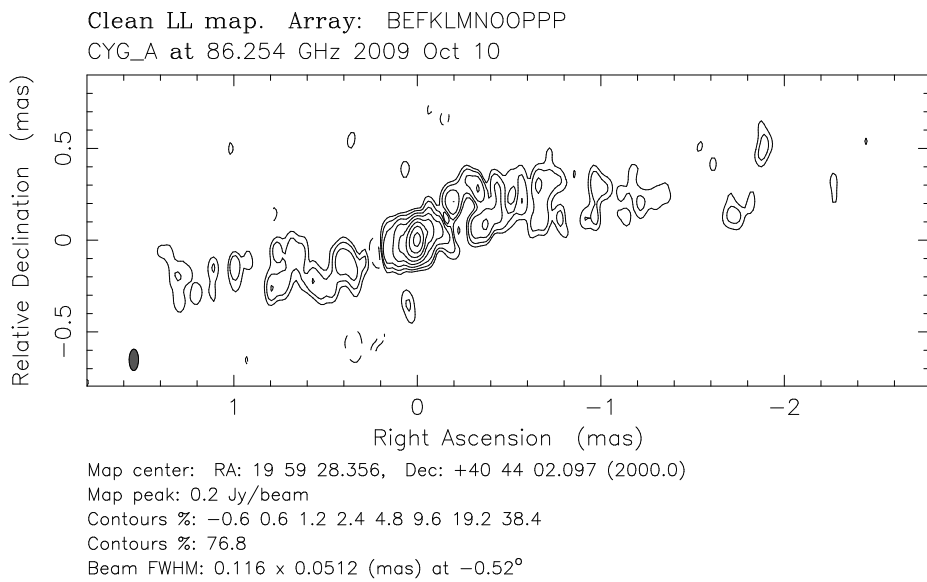


Figure 6.8: Clean map of Cygnus A at 86 GHz from GMVA observations in October 2009. A taper of 0.1 at a uv-radius of $3000 M\lambda$ was applied. Further information is reported in Tab. 6.2.1 (ref. no. 8).

6.3 Alignment of maps at different frequencies

One of the most commonly employed methods for correcting for the core-shift effect in VLBI images relies on the identification of one or more well-defined optically thin features, whose positions are not affected by opacity effects and therefore should coincide in simultaneous images at different frequencies. This procedure is quite successful in the case of blazars, whose jets often show bright knots of emission. However, the alignment is usually far more challenging in the case of radio galaxies. The reason is that the reduced Doppler boosting leads to a much “smoother” view of the jet, with the emission being dominated by the underlying flow and not by single features. Therefore it is not easy to unambiguously cross-identify optically thin components. In order to overcome these difficulties and achieve a reliable alignment of the maps, a method exploiting a pixel-based cross-correlation of various parameters of the jet is applied in this thesis. Besides the more classical analysis of the flux density distributions, two additional parameters related to the jet morphology, i.e. the jet width and the ridge line, were compared. Indeed the morphological profile of the jets in Cygnus A presents some well-defined and persistent characteristics, like the gap of emission or the bending of the jet towards south seen at ~ 2 mas at 43 GHz. In order to compare and confirm the results, a 2-D cross-correlation taking as a reference single features in the jet was also attempted. The alignment was determined between pairs of frequencies (Tab. 6.3.1) formed based on the date of observation, with the maximum time separation being about 1.5 months. Maps at different frequencies are of course characterized by different resolutions, which can affect significantly the appearance of the images. In order to minimize this effect, the maps in each pair were restored with a common circular beam, intermediate between the original beams (see Tab. 6.2.1). The pixel size was set to one fifth of the beam FWHM. Similarly to what was done for the analysis at 43 and 86 GHz, the maps were rotated by 16° clockwise and sliced pixel-by-pixel perpendicularly to the jet axis. Then, a single Gaussian fit was performed on the transverse intensity profiles, which allows to derive the longitudinal intensity profile, the width profile and the ridge line. The cross-correlation was performed with a bin of 2 pixels, while the interval of slices (i.e. the x interval) considered was case-dependent, in the sense that only the less noisy or better defined regions were taken into account. In the case of the intensity profiles, the main peak at $x=0$ was masked, otherwise the cross-correlation would give a zero shift for the best alignment. The main peak of the obtained DCCF (Discrete Cross-Correlation Function) was fitted with a Gaussian profile in order to determine the peak position, which corresponds to the shift one needs to apply for finally aligning the maps. The results of the cross-correlations are shown for each pair of images in the next sections.

A summary is presented in Table 6.3.1, together with the shifts which were actually applied to the maps after averaging the measurements from the four methods.

6.3.1 8 and 15 GHz

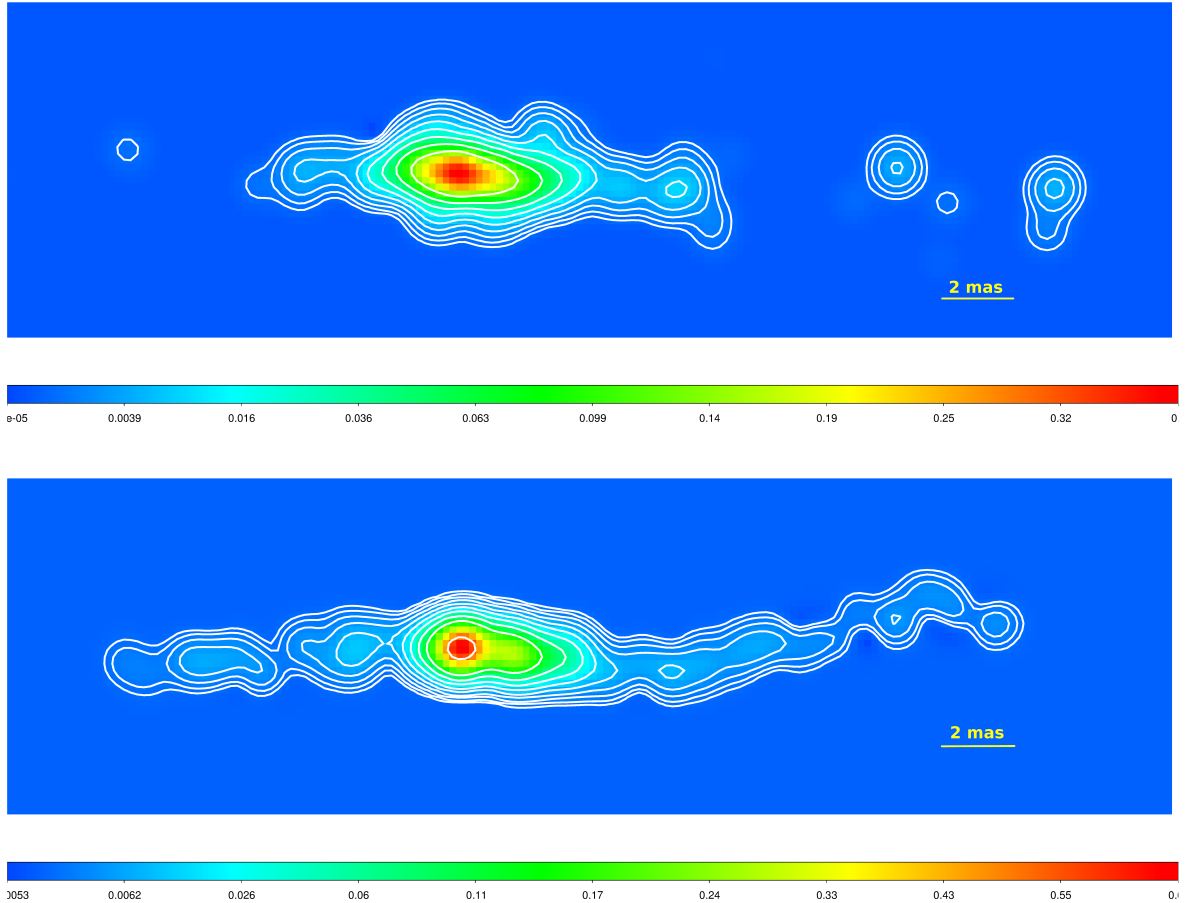


Figure 6.9: Clean maps at 8 and 15 GHz from VLBA observations in Jun 2006 (reference numbers 1&2 in Tab. 6.2.1). The maps were restored with a common circular beam of 0.9 mas. Contours represent isophotes at 0.5, 1, 2, 4, 8, 16, 32, 64, 128, 256, 512 mJy/beam. The peak fluxes and the natural beam sizes are reported in Tab. 6.2.1.

The maps at 8 and 15 GHz from observations in June 2006 (n. 1&2 in Tab. 6.2.1) were convolved with a common circular beam of 0.9 mas, and the pixel size was set to 0.18 mas (Fig. 6.9). The cross-correlation was computed using a bin of 0.36 mas. The results of the three cross-correlations consistently indicate that the maps at these frequencies are displaced by more than 1 mas (Fig. 6.10, 6.11, 6.12). A 2-D cross correlation was also attempted, yielding a shift of (-1.26 ± 0.18) mas in the x direction and of 0 mas in the y direction. The average shift is (-1.32 ± 0.09) mas.

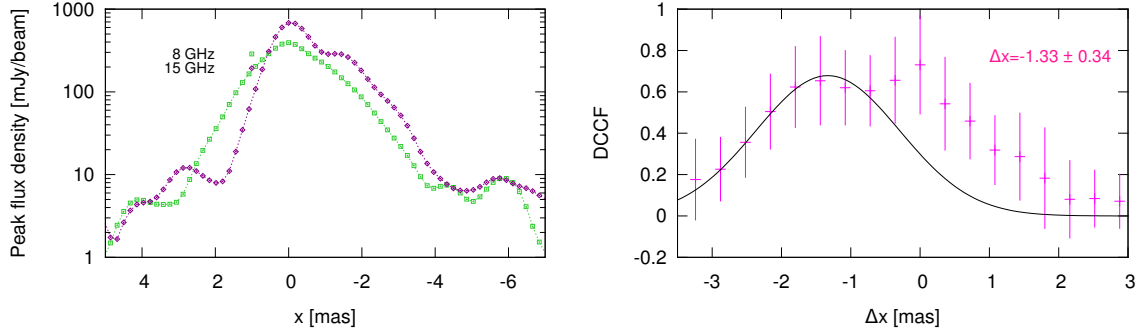


Figure 6.10: **Left-** Intensity profile at 8 GHz (green) and at 15 GHz (purple). **Right-** Derived position shift Δx between maps at 8 and 15 GHz as inferred from the intensity profiles.

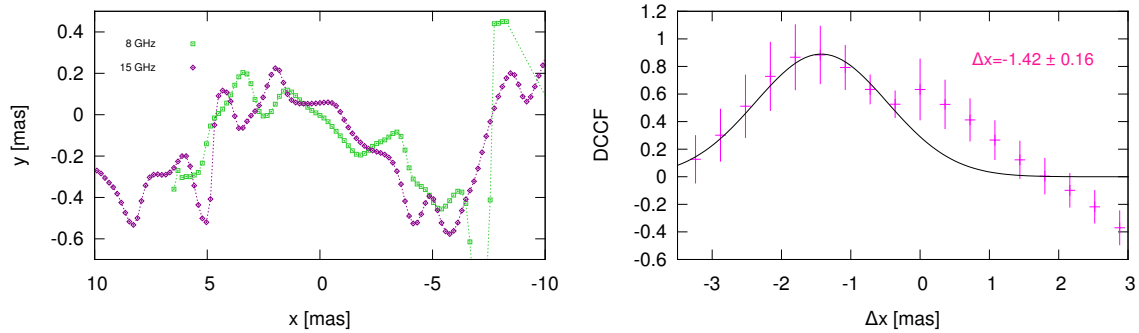


Figure 6.11: **Left-** Ridge line at 8 GHz (green) and at 15 GHz (purple). **Right-** Derived position shift Δx between maps at 8 and 15 GHz as inferred from the ridge lines.

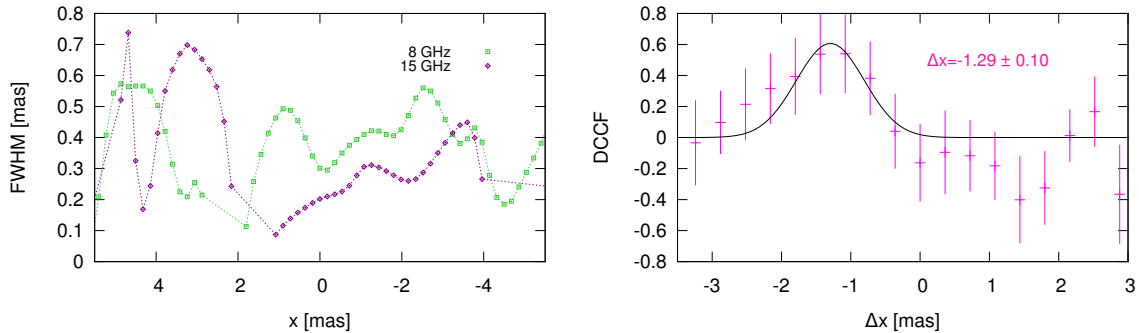


Figure 6.12: **Left-** Width profile at 8 GHz (green) and at 15 GHz (purple). **Right-** Derived position shift Δx between maps at 8 and 15 GHz as inferred from the width profiles.

6.3.2 15 and 43 GHz

The maps at 15 and 43 GHz from observations in October 2008 (n. 3&4 in Tab. 6.2.1) were convolved with a common circular beam of 0.3 mas, and the pixel size was set to 0.06 mas (Fig. 6.13). The cross-correlation was computed using a bin of 0.12 mas. The results of the three cross-correlations are consistent with a shift of the order of 0.5 mas (Fig. 6.14, 6.15,

6.16). A 2-D cross correlation was also attempted, yielding a shift of (-0.48 ± 0.06) mas in the x direction and of 0 mas in the y direction. The average shift is (-0.45 ± 0.02) mas.

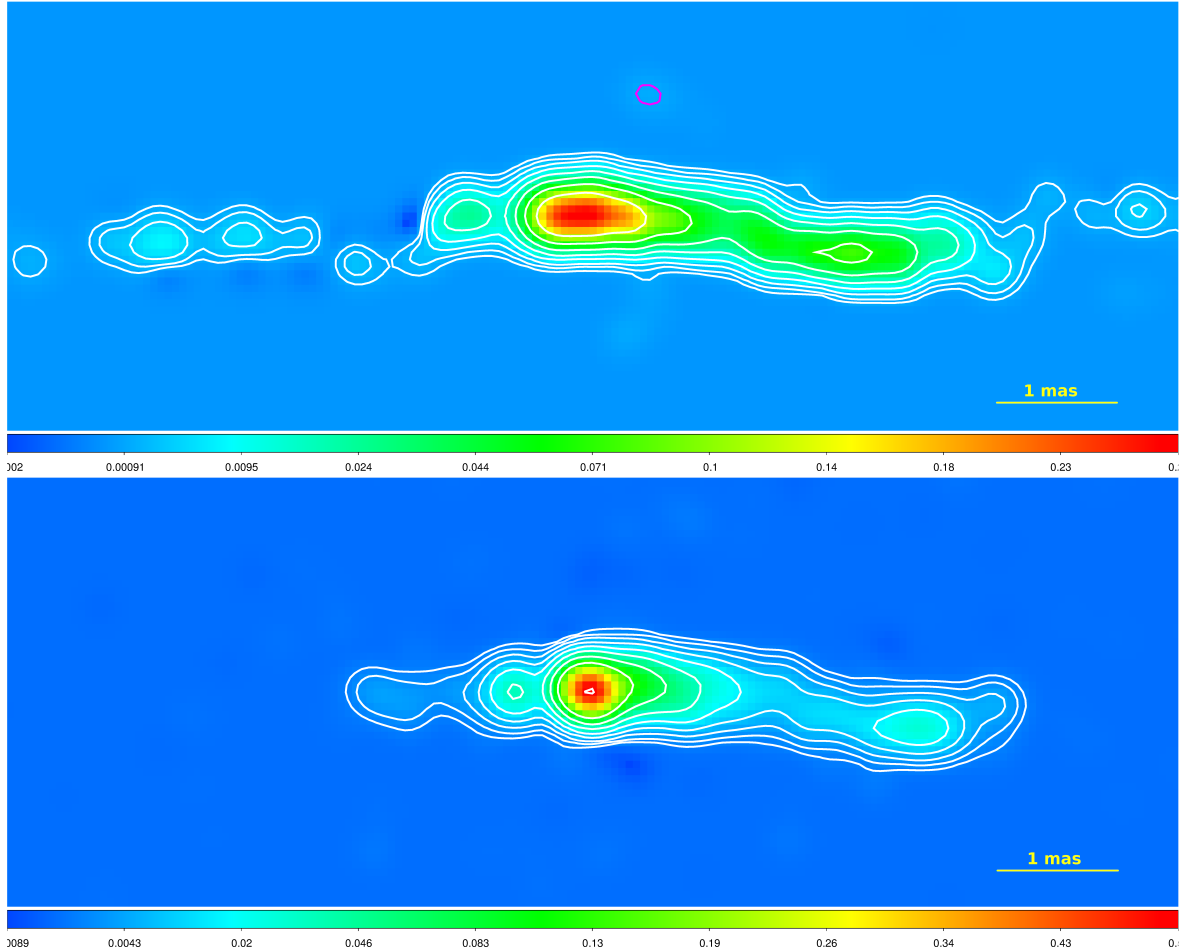


Figure 6.13: Clean maps at 15 and 43 GHz, respectively from VLBA and Global VLBI observations in October 2008 (reference numbers 3&4 in Tab. 6.2.1). The maps were restored with a common circular beam of 0.3 mas. Contours represent isophotes at 1, 2, 4, 8, 16, 32, 64, 128, 256, 512 mJy/beam. The peak fluxes and the natural beam sizes are reported in Tab. 6.2.1.

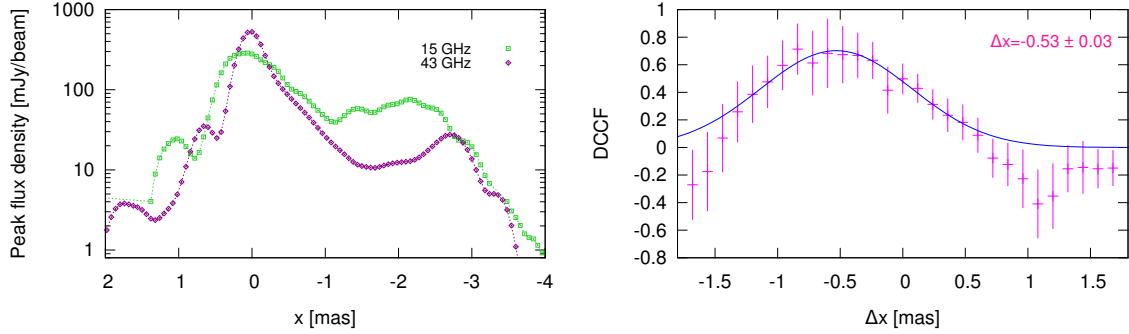


Figure 6.14: **Left-** Intensity profile at 15 GHz (green) and at 43 GHz (purple). **Right-** Derived position shift Δx between maps at 15 and 43 GHz as inferred from the intensity profiles.

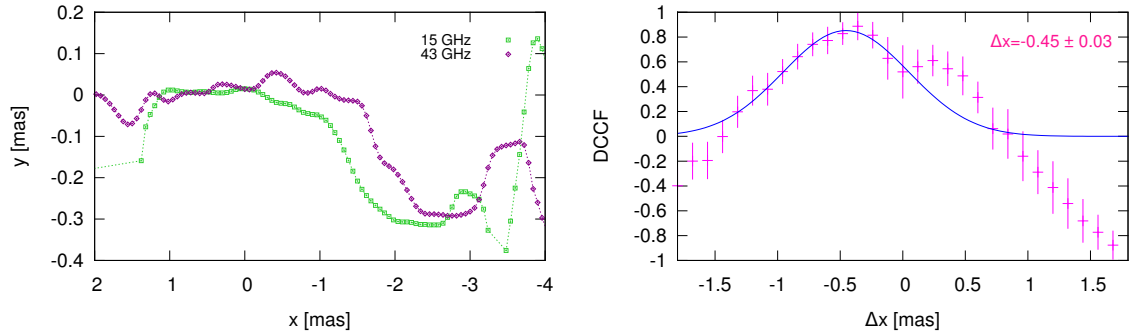


Figure 6.15: **Left-** Ridge line at 15 GHz (green) and at 43 GHz (purple). **Right-** Derived position shift Δx between maps at 15 and 43 GHz as inferred from the ridge lines.

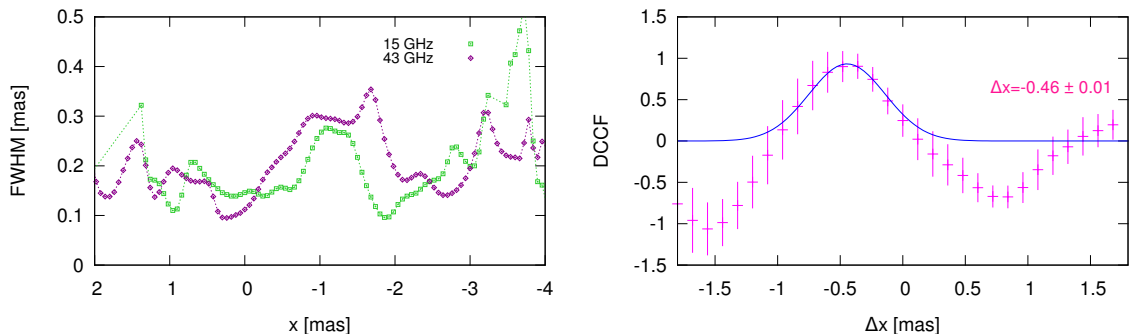


Figure 6.16: **Left-** Width profile at 15 GHz (green) and at 43 GHz (purple). **Right-** Derived position shift Δx between maps at 15 and 43 GHz as inferred from the width profiles.

6.3.3 22 and 43 GHz

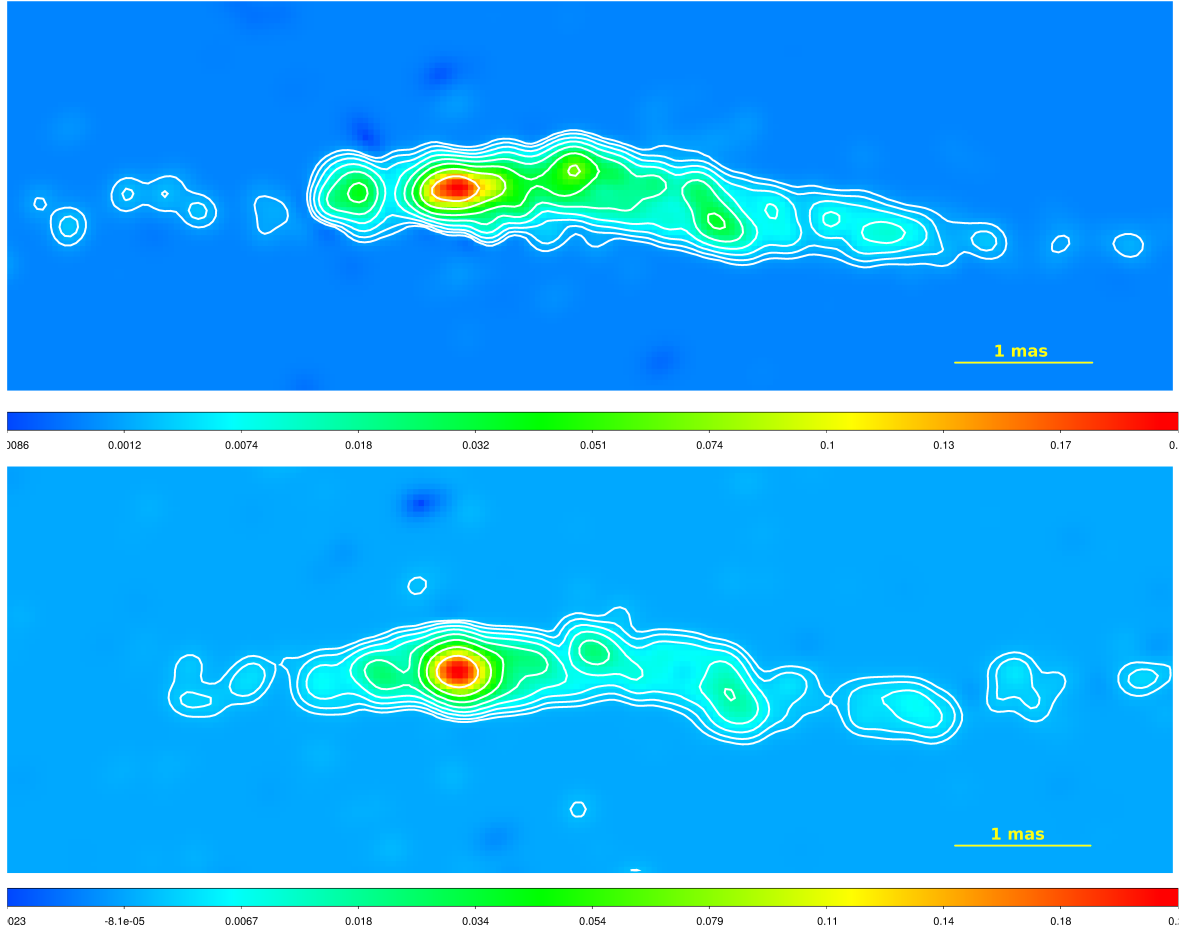


Figure 6.17: Clean maps at 22 and 43 GHz from VLBA+Eb observations in May 2015 (reference numbers 5&6 in Tab. 6.2.1). The maps were restored with a common circular beam of 0.2 mas. Contours represent isophotes at 1, 2, 4, 8, 16, 32, 64, 128, 256, 512 mJy/beam. The peak fluxes and the natural beam sizes are reported in Tab. 6.2.1.

The maps at 22 and 43 GHz from observations in May 2014 (Fig. 6.17) were convolved with a common circular beam of 0.2 mas, and the pixel size was set to 0.04 mas. The cross-correlation was computed using a bin of 0.08 mas. All the three cross-correlations infer exactly the same value of -0.16 mas (Fig. 6.18, 6.19, 6.20). A 2-D cross correlation was also attempted, yielding again a shift of (-0.16 ± 0.04) mas in the x direction and of 0 mas in the y direction. The average shift is (-0.16 ± 0.01) mas.

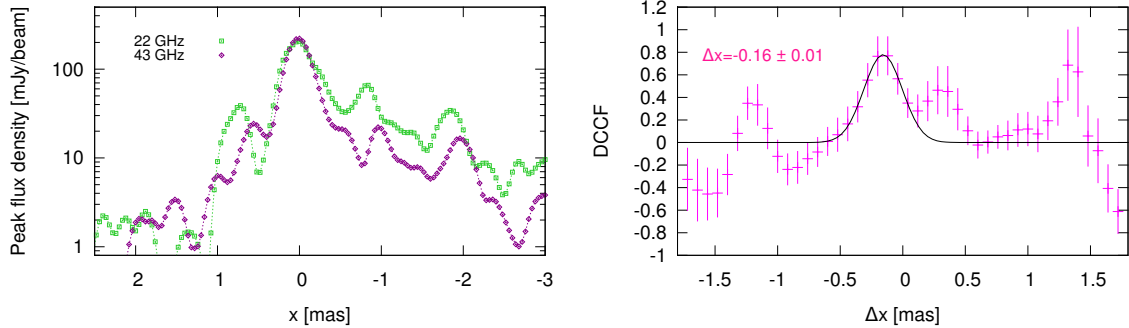


Figure 6.18: **Left-** Intensity profile at 22 GHz (green) and at 43 GHz (purple). **Right-** Derived position shift Δx between maps at 22 and 43 GHz as inferred from the intensity profiles.

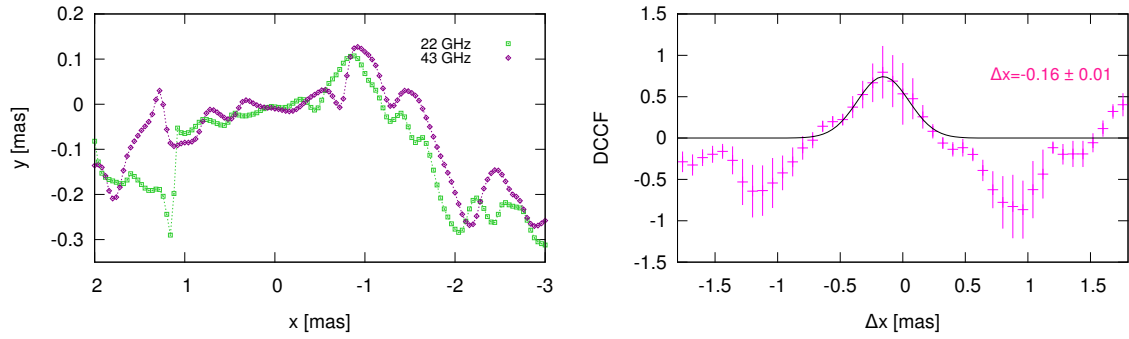


Figure 6.19: **Left-** Ridge line at 22 GHz (green) and at 43 GHz (purple). **Right-** Derived position shift Δx between maps at 22 and 43 GHz as inferred from the ridge lines.

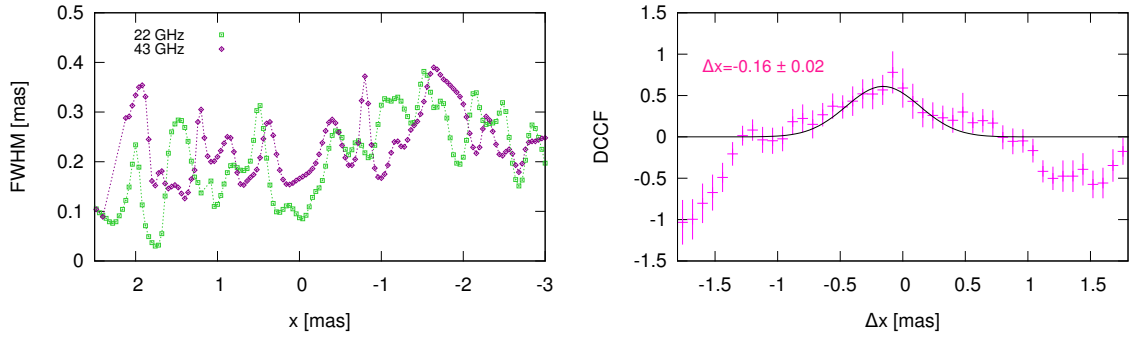


Figure 6.20: **Left-** Width profile at 22 GHz (green) and at 43 GHz (purple). **Right-** Derived position shift Δx between maps at 22 and 43 GHz as inferred from the width profiles.

6.3.4 43 and 86 GHz

The maps at 43 and 86 GHz from observations in Oct/Nov 2009 (Fig. 6.21) were convolved with a common circular beam of 0.15 mas, and the pixel size was set to 0.03 mas. The

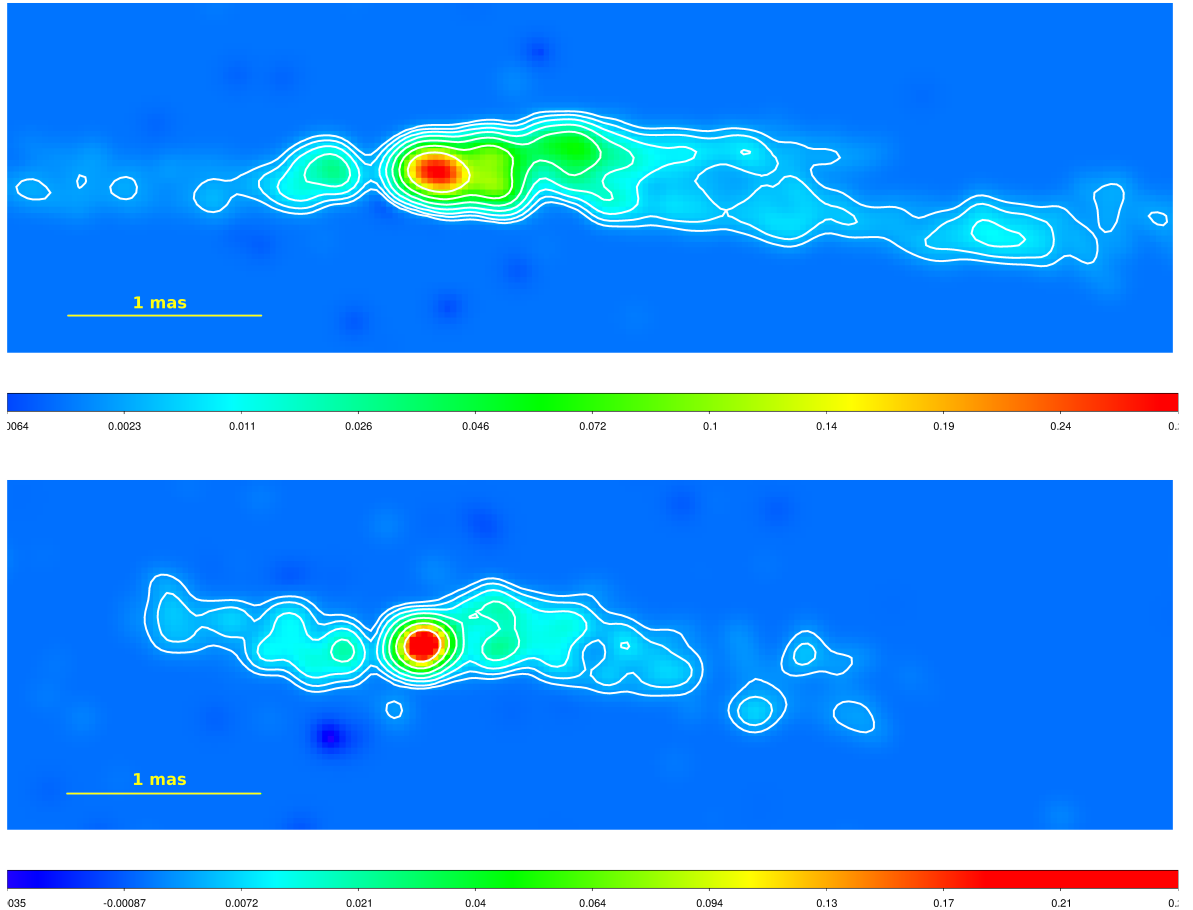


Figure 6.21: Clean maps at 43 and 86 GHz from Global VLBI observations in October/November 2009 (reference numbers 7&8 in Tab. 6.2.1). The maps were restored with a common circular beam of 0.15 mas. Contours represent isophotes at 2, 4, 8, 16, 32, 64, 128, 256, 512 mJy/beam. The peak fluxes and the natural beam sizes are reported in Tab. 6.2.1.

cross-correlation was computed using a bin of 0.06 mas. The results of the three cross-correlations oscillate around zero (Fig. 6.22, 6.23, 6.24). A 2-D cross correlation was also attempted, yielding a shift of (-0.03 ± 0.03) mas in the x direction and of (0.03 ± 0.03) mas in the y direction. The average shift in the x direction is (0.00 ± 0.01) mas, therefore no shift is applied at 43 GHz.

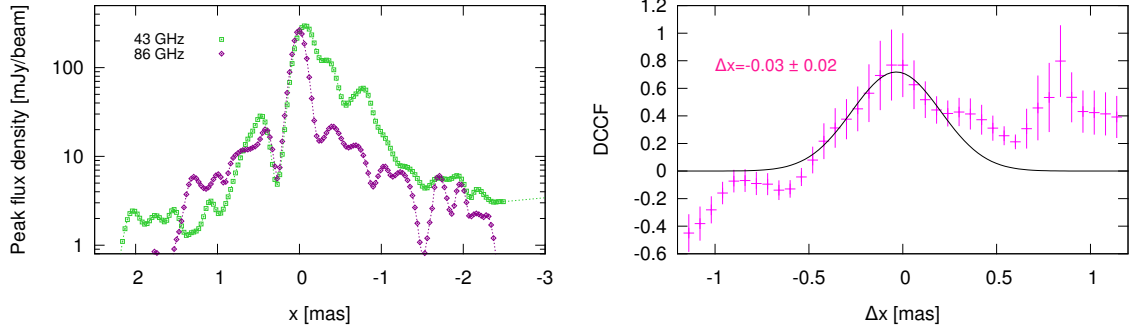


Figure 6.22: **Left-** Intensity profile at 43 GHz (green) and at 86 GHz (purple). **Right-** Derived position shift Δx between maps at 43 and 86 GHz as inferred from the intensity profiles.

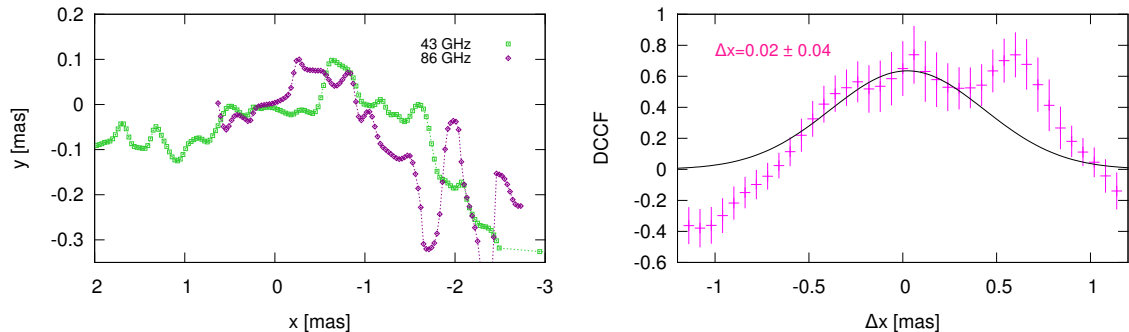


Figure 6.23: **Left-** Ridge line at 43 GHz (green) and at 86 GHz (purple). **Right-** Derived position shift Δx between maps at 43 and 86 GHz as inferred from the ridge lines.

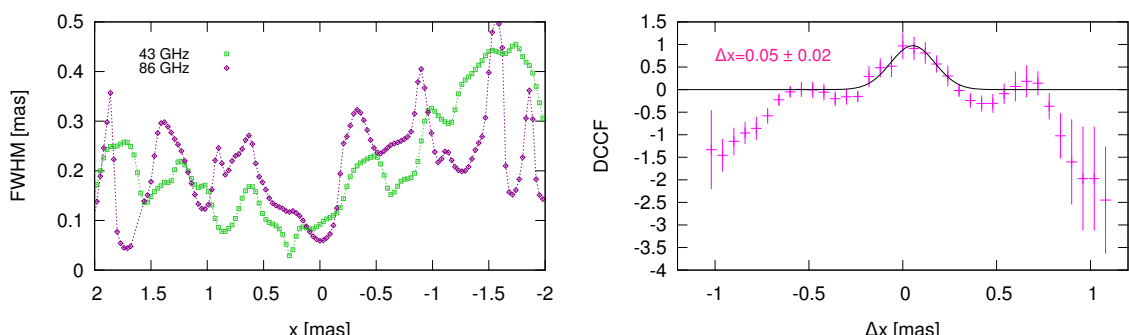


Figure 6.24: **Left-** Width profile at 43 GHz (green) and at 86 GHz (purple). **Right-** Derived position shift Δx between maps at 43 and 86 GHz as inferred from the width profiles.

Table 6.3.1: Opacity shifts in units of mas between each pair of frequencies (Col. 1) derived in Sect. 6.3 using four different methods (Col. 2-5). The values in Col. 6 are the average shifts finally applied to the maps.

Freq. [GHz]	Ridge line	Intensity profile	Width	2-D cross correlation	Average
8.1-15.4	-1.42±0.16	-1.33±0.25	-1.29±0.10	-1.24±0.18	-1.32±0.09
15.4-43.2	-0.45±0.03	-0.53±0.03	-0.46±0.01	-0.48±0.06	-0.48±0.02
22.2-43.2	-0.16±0.01	-0.16±0.01	-0.16±0.02	-0.16±0.04	-0.16±0.01
43.2-86.2	0.02±0.04	-0.03±0.02	0.05±0.02	-0.03±0.03	0.00±0.01

6.4 Spectral analysis

Once a reliable alignment of the images is achieved, a detailed, pixel-based spectral analysis of the jets can be performed. In order to test the hypothesis that the central engine is located in the gap of emission, the total shift of each map was computed taking as a reference the position of the gap, set to $x=0$. As it was shown in the previous Chapter, the gap appears to extend approximately between 0.2 and 0.3 mas to the east of the 43 and 86 GHz cores. At 43 GHz the gap is very sharp and well defined (see Fig. 6.22), and the minimum width occurs at 0.27 mas in all the maps. Therefore we assume this value for the distance between the 43 GHz core and the gap, $\Delta x_{43\text{-gap}}$. Since no significant shift $\Delta x_{86\text{-}43}$ was determined between 43 and 86 GHz, 0.27 mas is also the distance $\Delta x_{86\text{-gap}}$ between the 86 GHz core and the gap. With these assumptions, the total shift Δx_ν at each frequency ν is calculated as:

$$\Delta x_8 = \Delta x_{8\text{-}15} + \Delta x_{15\text{-}43} + \Delta x_{86\text{-}43} + \Delta x_{86\text{-gap}} = 2.07 \text{ mas}$$

$$\Delta x_{15} = \Delta x_{15\text{-}43} + \Delta x_{86\text{-}43} + \Delta x_{86\text{-gap}} = 0.75 \text{ mas}$$

$$\Delta x_{22} = \Delta x_{22\text{-}43} + \Delta x_{86\text{-}43} + \Delta x_{86\text{-gap}} = 0.43 \text{ mas}$$

$$\Delta x_{43} = \Delta x_{86\text{-}43} + \Delta x_{86\text{-gap}} = 0.27 \text{ mas}$$

$$\Delta x_{86} = \Delta x_{86\text{-gap}} = 0.27 \text{ mas}$$

where $\Delta x_{\nu_1\text{-}\nu_2}$ is the average relative shift between pairs of frequencies given in Tab. 6.3.1, Col. 6. After applying the aforementioned shifts to each map, three different approaches were followed for the spectral analysis.

- **1D analysis:** the spectral index was calculated between each pair of frequencies taking into account the flux of the pixels along the ridge line.
- **2D analysis:** spectral index maps were produced. This was done by processing each pair of images at the two frequencies through the AIPS task *COMB*.

- **Spectral fitting:** a model synchrotron spectrum was fitted to the data. Each data set was obtained by dividing the jet in small intervals Δx and calculating the integrated flux in each interval and for each of the 5 frequencies.

6.4.1 Ridge line spectrum

The spectral index α ($S_\nu \propto \nu^\alpha$) along the ridge line is presented in Fig. 6.25 for all pairs of frequencies. Error bars are not shown in the plot for clarity, but they are estimated as follows: assuming an error on the flux density of 5% at 8 and 15 GHz, 10% at 22 and 20% at 43 and 86 GHz, the error on the spectral index $\Delta\alpha$ is of the order of 0.25 between 8 and 15 GHz, 0.25 between 15 and 43 GHz, 0.48 between 22 and 43 GHz and 0.77 between 43 and 86 GHz. With this in mind, let us now analyze the following regions:

- **Gap and inner-jet:** by applying the shifts calculated in the previous sections we note that the spectral index profiles show a central peak aligned remarkably well at $x \sim 0$ mas, i.e at the location of the gap of emission. In fact, the position of the maximum index is displaced from 0 by only 1 pixel or less at 8-15 GHz, 15-43 GHz and 22-43 GHz. This can be considered the most striking evidence that the gap indeed represents the true location of the central engine. The maximum spectral index at $x \sim 0$ decreases with increasing frequency, ranging between $\sim +2.5$ and $+0.5$. Between 8 and 15 GHz, the maximum index of $+3$ is slightly displaced in the jet side by ~ 0.2 mas. Curiously, the spectral index between 86-43 GHz appears double humped, with a local minimum at $x \sim 0$, and two maxima at $\sim \pm 0.1$ mas. However, considering the quite large error bar $\Delta\alpha = 0.77$ it is not possible to say if this structure is real. With an $\alpha_{\max} \sim 3 \pm 0.25$ between 8 GHz and 15 GHz, we can instead state that, at these frequencies, the spectral index in the inner-jet exceeds the limit of $+2.5$ expected for a synchrotron self-absorbed region. This indicates the presence of further opacity, likely due to an absorber which must be optically thick at 8 GHz and at lower frequencies. As explained at the beginning of the Chapter, free-free absorption by a torus is expected on parsec scale in Cygnus A, both from previous studies and in the unified scheme. In the optically thick regime, the spectral index resulting from free absorption is $+2$. Therefore, if the region is self-absorbed and free-free absorbed at the same time, a maximum spectral index up to $+4.5$ can be observed. For frequencies higher than 8 GHz, there is no clear evidence of additional absorption in the gap, as a spectral index close to $+2.5$ can be expected in this region.
- **Counter-jet:** except for the region at $x \sim 0.2 - 0.3$ mas, the counter-jet shows a flat or inverted spectrum, with α oscillating on average between 0 and $+1$ at all frequencies.

Therefore, unlike for the gap of emission, the absorber in this region appears optically thick at least up to 43 GHz. Assuming an intrinsic spectral index of -1 for the optically thin underlying flow, optically thick free-free absorption can give rise to an observed spectral index up to +1, which is indeed observed. These results will be further investigated through the spectral fitting in Sect. 6.4.3.

- **Jet:** the spectrum of the approaching jet appears quite steep for the frequencies 15-43 GHz, 22-43 GHz and 43-86 GHz, with typical values of α between -1 and -1.5. The observed deviation from the canonical optically thin index of -0.7 suggests that the electron population may be characterized by a steeper power law energy distribution in the launching region. Between the highest frequencies of 43 and 86 GHz, even steeper indices are measured in some regions, for example in the inner jet. The latter may be due to uncertainties in the amplitude calibration. The outer jet sometimes exhibits a flatter index, e.g. at a distance of ~ 2 mas. The spectrum between 8 and 15 GHz is flatter, but note that at 8 GHz the VLBI core is located at ~ 2.07 mas, so the emission is still self-absorbed at this frequency.

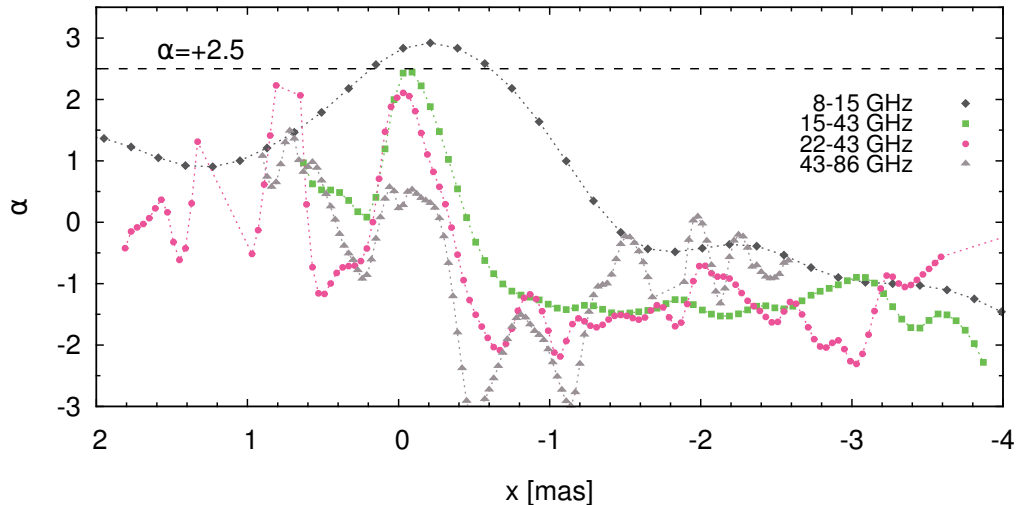


Figure 6.25: Ridge line spectral index at 8-15 GHz (dark grey), 15-43 GHz (green), 22-43 GHz (magenta), 43-86 GHz (light grey).

6.4.2 Spectral index maps

Each pair of images was processed through the AIPS task *COMB* for obtaining a spectral map (Fig. 6.26). In order to reduce the uncertainties, a 3σ cutoff (Tab. 6.1.1, Col. 8) was assumed for filtering out pixels with a flux density lower than this threshold. The maps confirm the results obtained for the ridge line spectrum in the different regions of the

source. In addition, they show more clearly that the highly inverted region at $x = 0$ extends more towards the jet side. Gradients in the transverse direction are observed. For example the maps at 15-43 GHz and at 22-43 GHz exhibit a flatter index at the edge of the jet. This may be due to the compression of the plasma in the interaction with the medium.

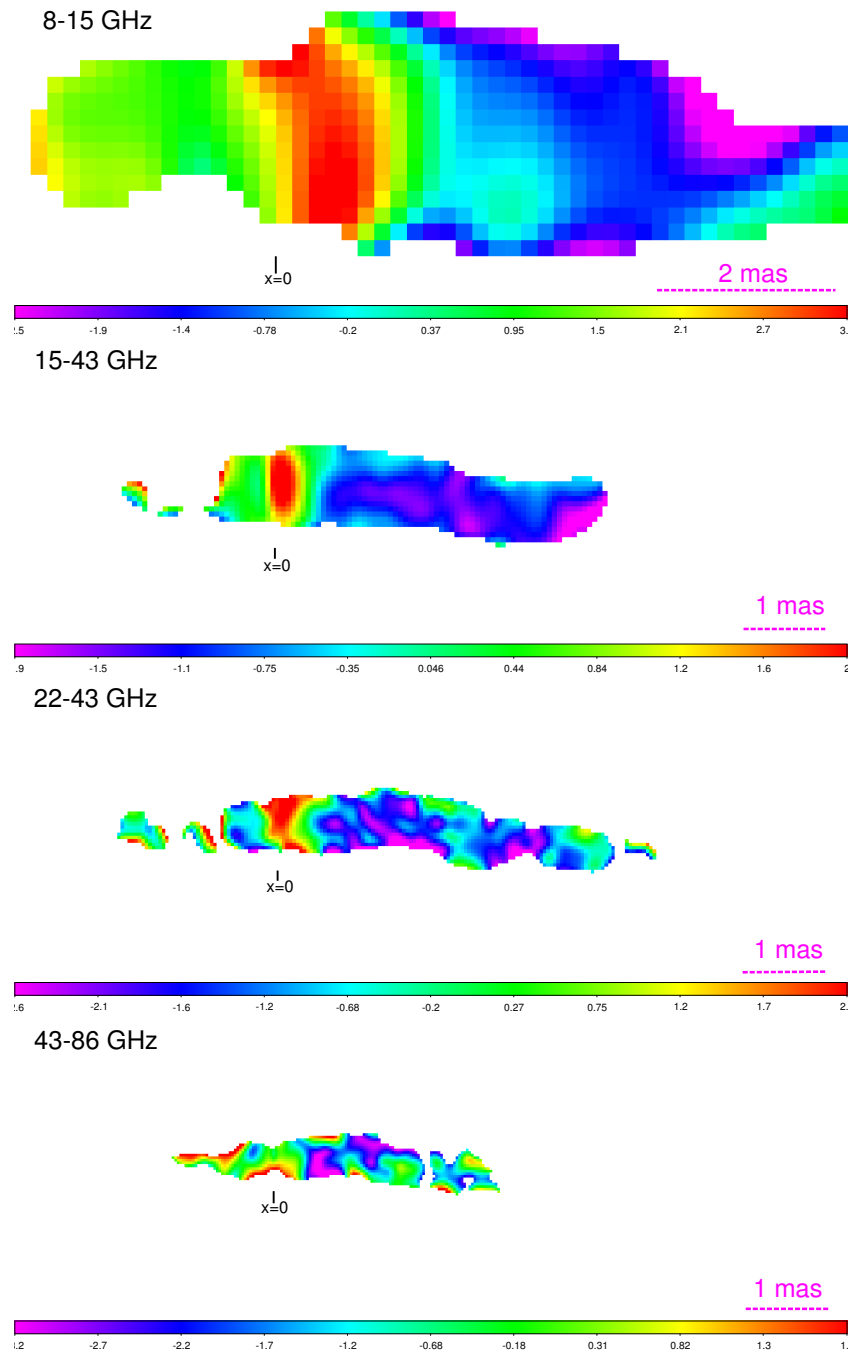


Figure 6.26: Spectral index maps of Cygnus A in the frequency range 8 - 86 GHz. $x=0$ indicates the position of the gap of emission.

6.4.3 Spectral fitting

In order to study in detail the spectral properties at different locations along the jet, a number of data sets was produced by binning the central 4 mas of the source in small intervals Δx and calculating the integrated flux in each interval at the 5 frequencies. The width of the interval was limited by the resolution of the map at the lowest frequency. Since the analysis at 8 GHz was performed on a slightly super-resolved map with a beam of 0.9 mas, the width of the intervals was set to 0.18 mas, which is the dimension of a single pixel at the lowest frequency. Among the maps at higher frequencies, those restored with the larger beam were chosen for this analysis, i.e. in Tab. 6.2.1, no. 2 for the frequency of 15 GHz, no. 4 at 43 GHz, and no. 8 at 86 GHz. This was done in order to make more solid the spectral fitting in the faint regions of the jets, avoiding flux losses. At 22 GHz, only a super-resolved map was available in the original data set (no. 5 in Tab. 6.2.1), therefore a new map with a larger beam of 0.45 mas was produced and analyzed. Then, a model synchrotron self-absorbed (SSA) spectrum was fitted to the data. Following [Türler et al. \(1999\)](#), this can be expressed as:

$$S_\nu = S_m \left(\frac{\nu}{\nu_m} \right)^{\alpha_{\text{thick}}} \frac{1 - \exp(-\tau_m(\nu/\nu_m)^{\alpha_{\text{thin}} - \alpha_{\text{thick}}})}{1 - \exp(-\tau_m)} \quad (6.4.1)$$

where S_ν is the flux density at frequency ν , ν_m is the turnover frequency, S_m is the flux density at the turnover, α_{thick} and α_{thin} are the spectral indices for the thick and thin part respectively and τ_m is the optical depth at the turnover. If the fit was stable enough, all parameters (S_m , ν_m , α_{thick} , α_{thin}) were set free, otherwise the optical thick spectral index was fixed to +2.5, the value expected assuming that the source is homogeneous. With the aim of probing the presence of a thick free-free absorber, the fit was also performed assuming an index of +4.5 for the optically thick part. This simplified method implicitly assumes that the SSA and free-free absorption (FFA) turnover frequencies coincide. While there is, in general, no reason why this condition should be verified, it will be shown that in the regions examined this appears to be often a good approximation. It should also be noticed here that, unlike in the two previous analyses (Sect 6.4.1, 6.4.2), flux densities from non-simultaneous observations were compared in this case. This introduces additional uncertainties related to the source variability, therefore error bars equal to 2σ (with σ defined in Sect. 6.4.1) were assumed. The results of the spectral fitting are reported in Table 6.4.1 and 6.4.2. The jet intervals reported in Table 6.4.1 are those where all the four parameters could be set free. Table 6.4.2, instead, presents the results for the remaining intervals, where both a standard SSA spectrum with $\alpha_{\text{thick}} = 2.5$ and a modified SSA with

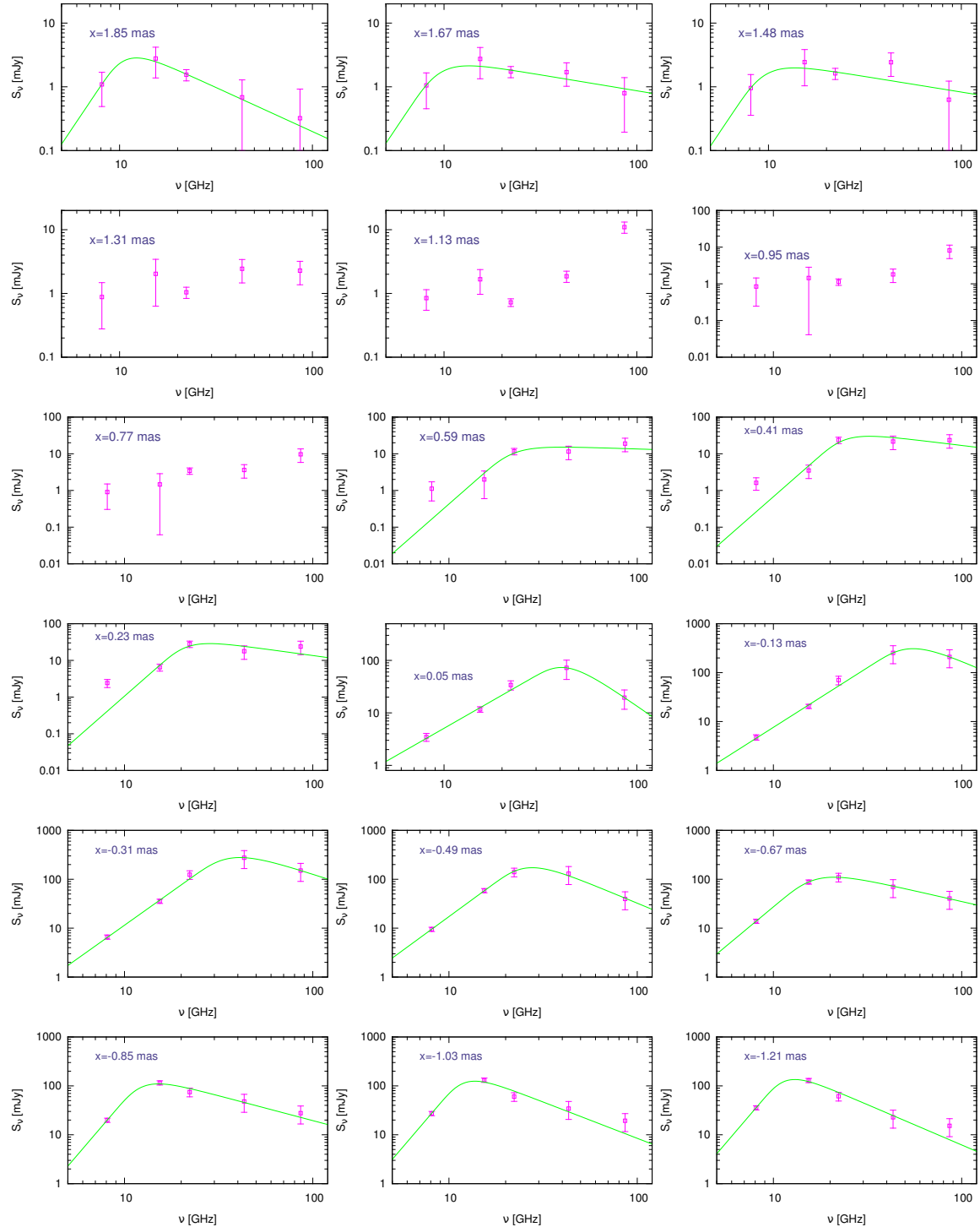
$\alpha_{\text{thick}} = 4.5$ were fitted.

Table 6.4.1: Spectral fitting in the central regions of the jets. All the four parameters in Eq. 6.4.1 were set free. Col. 1 - Distance from the gap of emission. Col. 2 - Flux density at the turnover. Col. 3 - Turnover frequency. Col. 4 - Optically thin spectral index. Col. 5 - Optically thick spectral index. Col. 6 - Reduced χ^2 (1 degree of freedom).

x [mas]	S_m [mJy]	ν_m [GHz]	α_{thin}	α_{thick}	χ_r^2
0.05	68.75 ± 25.83	46.00 ± 10.46	-2.54 ± 1.52	2.12 ± 0.35	1.55
-0.13	268.87 ± 154.5	70.38 ± 24.37	-1.71 ± 4.93	2.44 ± 0.32	2.01
-0.31	275.97 ± 107.9	43.48 ± 7.39	-1.25 ± 1.05	2.74 ± 0.20	1.13
-0.49	168.31 ± 15.89	30.32 ± 1.41	-1.60 ± 0.20	2.82 ± 0.07	0.11
-0.67	104.42 ± 1.23	25.66 ± 0.51	-0.88 ± 0.04	3.20 ± 0.05	0.01

Table 6.4.2: Spectral fitting in those jet intervals where the optically thick spectral index had to be fixed. Results from a standard SSA fit with $\alpha_{\text{thick}} = 2.5$ and from a modified SSA+FFA fit with $\alpha_{\text{thick}} = 4.5$ are compared in the two main columns. Col. 1 - Distance from the gap of emission. Col. 2 - Flux density at the SSA turnover. Col. 3 - SSA Turnover frequency. Col. 4 - SSA Optically thin spectral index. Col. 5 - Reduced χ^2 (2 degrees of freedom). Col. 6-9 - Same as Col. 3-5 but for SSA+FFA. Bold characters for the χ_r^2 values mark the best fit between the two.

x [mas]	SSA				SSA+FFA			
	S_m [mJy]	ν_m [GHz]	α_{thin}	χ_r^2	S_m [mJy]	ν_m [GHz]	α_{thin}	χ_r^2
1.85	2.34 ± 0.24	14.54 ± 0.90	-1.50 ± 0.32	0.09	2.82 ± 0.24	12.81 ± 0.36	-1.38 ± 0.19	0.04
1.67	1.95 ± 0.26	16.26 ± 2.66	-0.55 ± 0.26	0.35	2.13 ± 0.34	13.49 ± 1.30	-0.50 ± 0.24	0.32
1.48	1.76 ± 0.49	13.54 ± 4.09	-0.54 ± 0.47	0.94	1.93 ± 0.63	11.95 ± 2.17	-0.49 ± 0.45	0.93
1.31	-	-	-	-	-	-	-	-
1.13	-	-	-	-	-	-	-	-
0.95	-	-	-	-	-	-	-	-
0.77	-	-	-	-	-	-	-	-
0.59	14.26 ± 8.82	34.62 ± 12.64	-0.30 ± 1.29	2.39	13.79 ± 7.11	27.78 ± 6.48	-0.16 ± 0.87	2.19
0.41	26.35 ± 15.33	45.83 ± 13.46	-0.62 ± 1.74	3.90	29.93 ± 16.76	33.67 ± 6.62	-0.62 ± 1.24	3.56
0.23	25.72 ± 12.59	38.36 ± 9.35	-0.83 ± 1.71	3.84	28.56 ± 16.78	30.14 ± 5.61	-0.70 ± 1.41	6.83
-0.85	92.79 ± 18.87	23.48 ± 2.54	-1.41 ± 0.76	4.13	109.89 ± 8.30	15.18 ± 0.36	-1.02 ± 0.20	0.64
-1.03	102.72 ± 20.68	18.00 ± 1.96	-2.04 ± 1.16	5.29	123.34 ± 17.43	14.51 ± 0.61	-1.49 ± 0.45	2.21
-1.21	110.19 ± 15.17	16.81 ± 1.27	-2.06 ± 0.66	2.91	132.39 ± 14.56	13.90 ± 0.44	-1.65 ± 0.44	1.37
-1.39	106.78 ± 11.41	15.30 ± 1.87	-2.05 ± 0.44	1.84	128.31 ± 13.89	13.14 ± 0.40	-1.77 ± 0.31	1.26
-1.57	96.38 ± 10.00	13.67 ± 0.70	-2.02 ± 0.37	1.55	114.68 ± 12.93	12.29 ± 0.39	-1.86 ± 0.30	1.22
-1.75	86.34 ± 7.51	12.24 ± 0.58	-1.92 ± 0.26	1.00	99.79 ± 9.16	11.45 ± 0.34	-1.83 ± 0.22	0.78
-1.93	81.18 ± 9.57	10.99 ± 1.07	-1.71 ± 0.40	1.72	89.73 ± 12.45	10.63 ± 0.70	-1.65 ± 0.36	1.59
-2.11	82.54 ± 6.72	10.33 ± 0.92	-1.58 ± 0.26	0.98	89.26 ± 8.48	10.19 ± 0.61	-1.54 ± 0.23	0.93



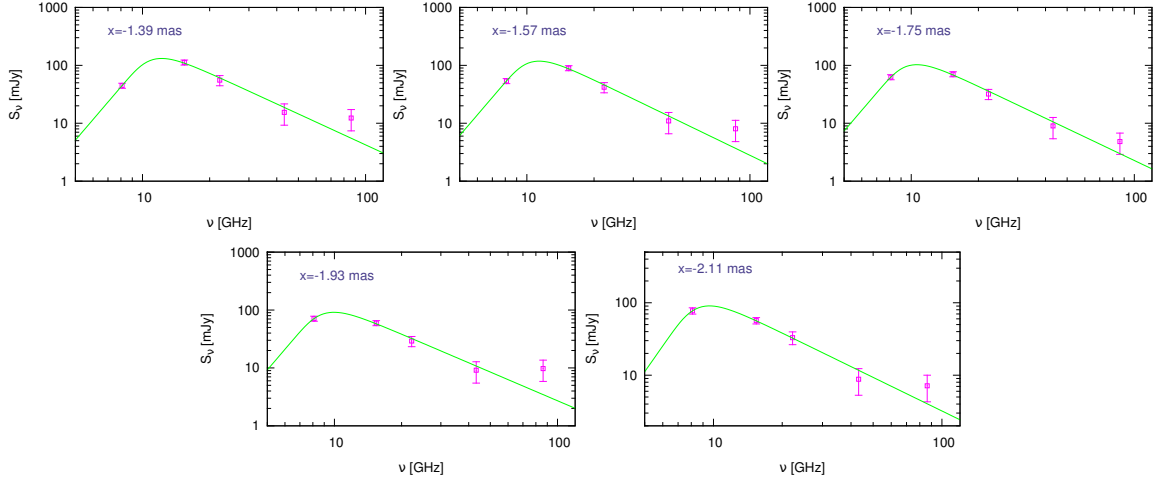


Figure 6.27: Fit of a Synchrotron self-absorption spectrum in different regions of the source.

By comparing the values of χ^2_r in Tab. 6.4.2, Col. 5 and Col. 9, it is clear that the SSA+FFA fitting yields significantly better results in most of the intervals. Figure 6.27 shows the best fits for all the intervals. Only in one case, at $x = 0.23$ mas, the SSA spectrum appears to fit better. By considering also the results in Tab. 6.4.1 we infer that only a narrow region between 0.23 and -0.13 mas, i.e. the gap of emission, can be well described without introducing additional opacity. The spectral properties in the jet side appear compatible with the presence of an absorber with FFA turnover frequency in the range 8-15 GHz, close to the SSA turnover frequency. However the counter-jet exhibits a more complex behavior, and the simplified model assumed may not be sufficient in this region. In the counter-jet, the optically thin part of the spectrum is either flatter compared to the jet side (i.e. between 1.48-1.31 mas 0.59-0.41 mas) or inverted up to high frequencies (between 1.13 and 0.77 mas). This indicates that the FFA turnover occurs at higher frequencies respect to the underlying synchrotron spectrum. This fact can also be noticed by comparing the obtained values of the turnover frequencies in jet and counter-jet (Fig. 6.28). While in the jet side the values are approximately those expected from the known locations of the VLBI cores, in the counter-jet the turnover frequencies are higher, especially in the first mas. These results will be further investigated in the next section.

Before concluding, we note that the spectral fitting provides, in principle, the necessary parameters for estimating the magnetic field at each location. Following Marscher (1983), the strength of the magnetic field B can be expressed as:

$$B = 10^{-5} b(\alpha) \phi^4 \nu_m^5 S_m^{-2} \left(\frac{\delta}{1 + Z} \right) \quad (6.4.2)$$

where $b(\alpha)$ is a tabulated parameter depending on the spectral index, ϕ is the size of the emitting region, δ is the Doppler factor and Z is the redshift. However, there are several factors which could prevent a correct estimate to be given. First, the formula applies to a uniform, compact and spherical emission region, while in this case the analysis takes into account the continuous distribution of the flow. Second, although the width of the jet is known at each point, this is not strictly the size of the emission region, which is actually produced only from the edges of the jet. Assuming that these effects are less severe in the proximity of the core, due the higher compactness of the emission, we attempt to estimate the magnetic field in this region. With a size of 0.06 mas for the 86 GHz core (Sect. 5.5), a Doppler factor of 1 and a maximum turnover frequency of 70 GHz (Fig. 6.28), the magnetic field strength in the surroundings of the 86 GHz core would be of the order of ~ 11 Gauss.

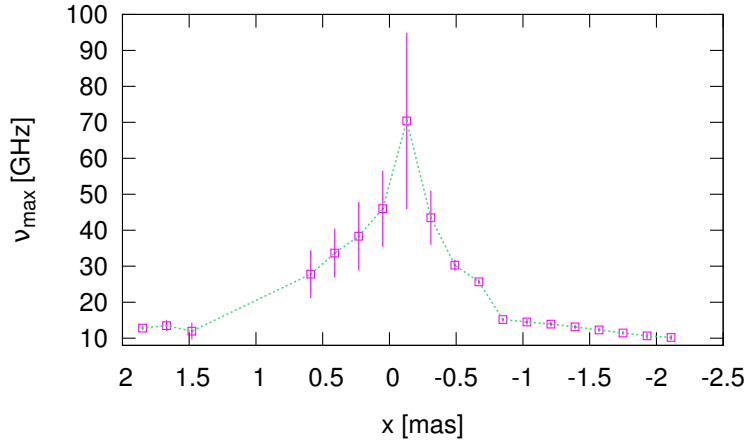


Figure 6.28: Turnover frequency versus distance from the gap.

6.5 FFA opacity

The previous section has provided a good understanding of the spectral properties of the jets, suggesting that, with the exception of the some very central regions in the surrounding of the gap, the presence of an absorber is needed for explaining them. One region in the counter-jet appears to be more strongly affected, showing a flat or inverted spectrum up to 86 GHz. We would now like to quantify the opacity along the source by fitting a free-free absorption model to the data. An optically thin synchrotron spectrum modified by FFA can be written as:

$$S_\nu \propto \nu^\alpha \exp(-\tau\nu^{-2.1}) \quad (6.5.1)$$

The opacity τ is a function of the temperature T , of the electron density n_e along the line of sight and of the path length s , and it can be expressed as:

$$\tau = 8.24 \times 10^{-2} T^{-1.35} n_e^2 s \quad (6.5.2)$$

In the counter-jet, Eq. 6.5.1 was fitted to the optically thin part of the spectra. The underlying synchrotron spectral index α was set to -1.5 or -1 based on the values determined in the jet side. In the approaching jet, there is no evidence for absorption at frequencies above the SSA turnover, therefore the only possibility for estimating the FFA opacity is to take into account the optically thick part of the synchrotron spectrum, assuming $\alpha = 2.5$. In general only two data points, from the frequencies 8 and 15 GHz, are available in this regime, thus the inferred τ is often poorly constrained and does not have an error bar (two free parameters for two data points). Results are shown in Fig. 6.29. The opacity τ appears to vary smoothly in the range 140-400 in core region and in the jet side. However a region in the counter-jet extending for ~ 1 -1.5 parsecs appears to feature much higher opacities, with τ up to ~ 1800 . These results indicate the presence of an absorber with two components: a diffuse material covering more uniformly the central 4 parsecs of the source (possibly more) and a denser and/or colder absorber with high compactness covering the counter-jet for ~ 1 -1.5 parsecs, located at a distance of ~ 0.5 parsec from the central engine. From eq. 6.5.2,

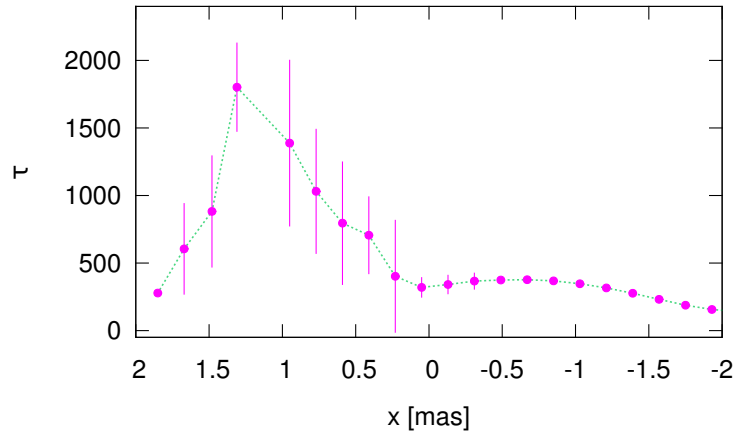


Figure 6.29: FFA opacity versus distance from the gap.

assuming a temperature $T = 10^4$ K and a path length of 1 parsec, the maximum opacity $\tau_{\max} = 1802 \pm 326$ implies a maximum electron density $n_e = (7.4 \pm 0.7) \times 10^4 \text{ cm}^{-3}$. Interestingly, similar results were found for the type 2 source NGC 1052 (Sawada-Satoh et al. 2009), both for the opacities and for the spatial extent and distribution of the absorber. For Cygnus A, this is the first evidence for the presence of such a dense absorber on sub-

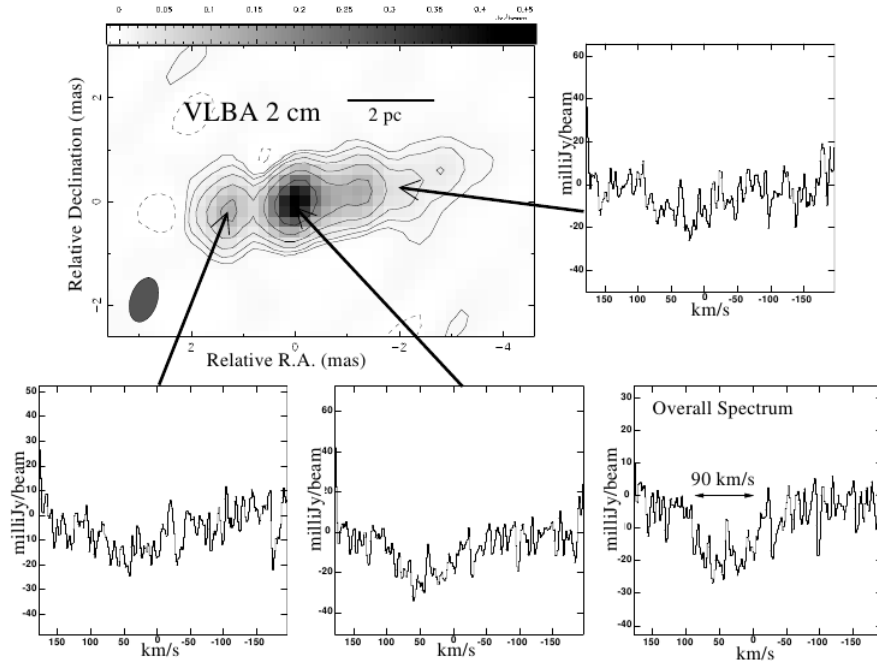


Figure 6.30: VLBI study of excited OH in absorption. A diffuse absorber is detected across the source ([Impellizzeri et al. 2006](#)).

parsec scale. Only one VLBI study searching for excited OH ([Impellizzeri et al. 2006](#)) had resulted in a tentative detection of a diffuse material spread over the entire source (Fig. 6.30), compatible with the diffuse component also detected in the present study. Given the high compactness of the second component, it is not surprising that this has not been detected in previous studies, evidently missing the necessary resolution.

6.6 Core shift

The determination of the core shift is not only crucial for the purposes of the spectral analysis, but also provides important information on the physical conditions at the base of the jet. In the classical Königl model ([Königl 1981](#)), the dependence of the core position on frequency is expressed as $z_{\text{core}} \propto \nu^{-1/k_r}$, where the power law index k_r is determined by three parameters:

- the magnetic field distribution $B = B_1(z_1/z)^m$
- the particle density distribution $N = N_1(z_1/z)^n$
- the shape of the electron energy spectrum, assumed to be a power law with index s , and giving rise to radiation with spectral index $\alpha = (1 - s)/2$ (see Sect. 1.3.2).

Here B_1 and N_1 are the magnetic field and particle density at $z_1 = 1$ parsec. In the case when only self-absorption takes place, the k_r index is fully described by the power-law indices m , n and α as:

$$k_r = \frac{((3 - 2\alpha)m + 2n - 2)}{(5 - 2\alpha)} \quad (6.6.1)$$

If the core is in equipartition, the power index k_r is equal to 1, which implies $m = 1$ and $n = 2$. Studies on large samples of blazars (e.g. [Sokolovsky et al. 2011](#); [Pushkarev et al. 2012](#)) reveal that most of the parsec-scale jets are indeed in equipartition. It is however possible to observe deviations, either indicating that equipartition is not verified or that additional opacity from surrounding material affects the core positions. Moreover, external pressure gradients of the kind $p \propto z^{-a}$ can also modify the dependence of B and N . Given the intrinsic power law index m , the magnetic field decreases as z^{-m_p} in the presence of an pressure external gradient, with $m_p = ma/4$. The index of particle density distribution, instead, can be expressed as $n_p = a(3 - 2\alpha)/4$. The analysis in Chapter 4 has suggested that the collimation profile and the acceleration properties of the flow in Cygnus A are compatible with the presence of an external pressure gradient with power law index $a \sim 2$. Let us now determine k_r from the measured core positions (Fig. 6.31). By fitting a power law of the kind $f(x) = A + Bx^C$, with $C = -1/k_r$, we obtain $k_r = 0.47 \pm 0.04$. The inferred index k_r deviates significantly from 1. One explanation for this is that the jet is not in equipartition, which is plausible based the results that the jet is magnetically-driven (Chapter 4). Alternatively, this deviation may be due to the external pressure gradient. Assuming a spectral index $\alpha = 0$, which is approximately the value inferred in Sect. 6.4.1 at the locations of each VLBI core (see Fig. 6.25), and $a = 2$ (estimated in Chapter 4) one obtains $n_p = 1.5$. With these values and with the calculated index k_r , the value of m_p inferred from Eq. 6.6.1 is 0.45, therefore $m = 0.9$. If these assumptions are correct, the value obtained for m is compatible with the expectation that the magnetic field has developed a significant toroidal component, whose strength should decrease as z^{-1} . Further investigation is necessary for clarifying this topic.

6.7 Conclusions

In this Chapter, a multi-frequency study of the parsec and sub-parsec scale structure in Cygnus A was presented. The results can be summarized as follows:

- A method combining the cross-correlation of 4 observables of the jet (lateral intensity profiles, 2D total intensity, width profile and ridge line profile) was employed for determining the opacity shifts between maps at different frequencies.

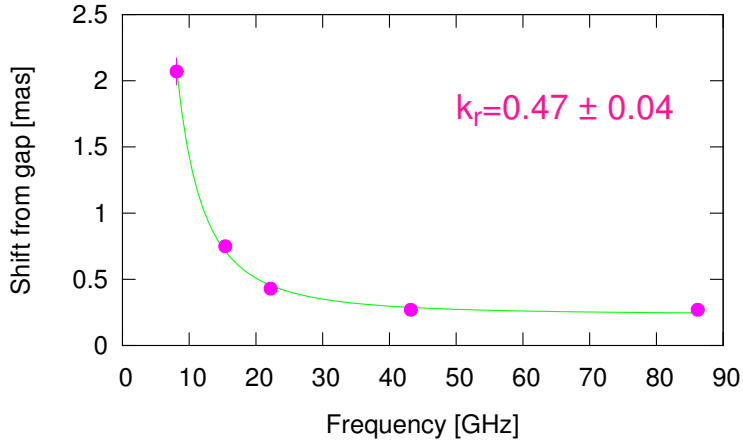


Figure 6.31: Core positions as a function of frequency.

- The spectral profile across the ridge line, as well as the spectral index maps, make clear that the gap is the region with the most inverted spectral index, varying between +0.5 and +2.5. This supports the hypothesis that the central engine is located in the gap of emission, whose spectral properties are consistent with those expected for a self-absorbed region.
- The spectral fitting indicates the presence of absorption, acting especially at 8 and 15 GHz. One region of the counter-jet is characterized by an inverted spectrum also at high frequencies, therefore the absorber may have an higher turnover frequency at this location.
- A free-free absorption spectrum was also fitted to the data in order to calculate the opacity. The analysis revealed the presence of an absorber with two components: a diffuse one spread homogeneously across the source and a denser and/or colder component with high compactness and confined between ~ 0.5 and 1.5 parsecs from the central engine. Assuming a temperature $T = 10^4 K$ and a path length of 1 parsec, the maximum electron density estimated for the compact component is $n_e = (7.4 \pm 0.7) \times 10^4 \text{ cm}^{-3}$.

Chapter 7

Conclusions and future work

The present thesis focused on a high resolution VLBI study of the radio galaxy Cygnus A. The data set mainly comprised observations at 43 and 86 GHz from Global VLBI arrays, and it was complemented by lower frequency VLBA data at 8, 15 and 22 GHz. Overall, data from observations performed in a time interval of 8 years (2006-2014) were considered.

The primary scientific motivation was to investigate the physical properties of a relativistic jet on scales which are relevant for testing jet formation models and the unified scheme for AGN. In this context, Cygnus A has probed to be an ideal object. VLBI observations at millimeter wavelengths provide, for this source, a spatial resolution of only ~ 200 Schwarzschild radii, which enables to image the nuclear regions and the base of the two-sided jet in great detail. Previous VLBI studies of relativistic jets have rarely probed such small scales, and those few cases have always concerned low-power FRI radio galaxies (e.g. Müller et al. 2011; Doeleman et al. 2012; Nagai et al. 2014). Indeed, FRII radio galaxies are often too faint on parsec and sub-parsec scales, especially at high radio frequencies. Cygnus A is in this sense a unique target, as the nuclear region appears still compact and bright enough at 86 GHz. Moreover, the large inclination of the jet relative to the line of sight ($\theta \sim 75^\circ$) facilitates the study of the intrinsic properties of the flow, as both geometrical and relativistic effects are much reduced.

The work of this thesis was divided in three parts addressing different topics and complementing each other at the same time. The first part was presented in Chapter 4 and it focused on the analysis of the acceleration and collimation properties of the flow from multi-epoch Global VLBI observations at 43 GHz. The importance of this study resides in the fact that, while theoretical models and simulations converge quite well in the predictions for magnetically-driven jets, very few observational constraints were provided until now. In this thesis it was shown that the flow in Cygnus A accelerates and collimates

on a scale of $\sim 10^4 R_S$, showing a parabolic shape ($r \propto z^{0.55 \pm 0.07}$) in the acceleration region and a cylindrical shape further downstream. According to recent studies (e.g. [Komissarov et al. 2007](#); [Lyubarsky 2009](#)) the extended nature of the acceleration is a characteristic signature in magnetically-driven jets. Moreover, the collimation profile is consistent with the jet being confined by a medium whose pressure is decreasing slowly with distance from the core ($p \propto z^{-2}$). The presence of such a medium should ultimately allow the jet to efficiently convert the magnetic energy into kinetic energy of the bulk flow until equipartition is reached. A similar analysis was previously only conducted for the FRI object M87 ([Asada & Nakamura 2012](#)). As pointed out in Chapter 4, the comparison between the results obtained for the two most famous FRI and FRII objects, M87 and Cygnus A respectively, indicates no significant difference in the acceleration region, where the two jets also have a very similar parabolic shape. However a substantial difference is observed on a scale of $\sim 10^5 R_S$, where the M87 jet becomes conical instead. Such a transition may occur if the pressure of the external medium is decreasing faster than $p \propto z^{-2}$, and it implies that no efficient acceleration can take place at this point. In this scenario, the high power, thin jets of the FRII sources and the lower power, broader jets of the FRI sources could be well reproduced if two originally similar flows propagate in external media with different pressure gradients. In other words, the results of the thesis suggest that the FRI/FRII dichotomy might result from different environmental conditions.

The imaging at 43 GHz also revealed a pronounced transverse stratification of the jet, which is limb brightened. The kinematic and light-curve analysis of the MODELFIT components indicates the presence of a transverse gradient of the bulk Lorentz factor Γ , with a fast layer accelerating from $\Gamma \sim 1$ to $\Gamma \sim 2.5$ and a slow layer flowing at mildly relativistic speeds ($\Gamma \sim 1$). Since any fast relativistic flow appears faint at large viewing angle (due to Doppler de-boosting), the observed limb brightening points towards a spine-sheath structure of the jet. In order to clarify the origin of these transverse gradients, the double ridge line was investigated also at 86 GHz (Chapter 5), with the aim of better tracing its structure in the nuclear regions. At 86 GHz, the double ridge line is indeed better resolved towards the core, and its detection in the immediate vicinity of the nucleus suggests that the jet is intrinsically stratified since its very origin as a direct result of the jet launching mechanism. In addition, the study at 86 GHz was targeted to test the hypothesis that the true central engine in Cygnus A is located at the position of an emission gap at 0.2-0.3 mas east of the 43 GHz core, from which the two jets appear to emanate. The gap is either less prominent or not visible at 86 GHz, and its physical properties (e.g. transverse width and flux density) appear more variable. These facts are in agreement with the expectations for a self-absorbed region, whose opacity decreases at high frequency. Also

the observed variability of the lateral intensity profiles at 86 GHz is consistent with the two jets emanating from this location. The analysis of the width profile at 43 and 86 GHz gave an interesting insight of the nature of the launching region. In fact it was inferred that the jet appears nowhere narrower than $135 \pm 27 R_S$. Since this size is larger than any possible ISCO¹ radius, the conclusion is that the jet launching region involves most likely the outer part of the accretion disk, as it is suggested by the [Blandford & Payne \(1982\)](#) mechanism. A contribution from the rotational energy of the black hole itself can however not be excluded. Some theoretical works (e.g. [Hardee et al. 2007](#); [Xie et al. 2012](#)) have proposed that both the Blandford-Payne and the [Blandford & Znajek \(1977\)](#) mechanisms may act simultaneously in relativistic jets, the former leading to the creation of an external sheath from a disk wind and the latter fueling a central spine from the ergosphere. In jets seen at large viewing angles, like in Cygnus A, it is expected that the slower disk wind would dominate the emission. This scenario fits well with the observed transverse gradients of bulk speed and of the intensity, as well as with the large transverse size of the jet base.

The third and last part of this thesis consisted of a spectral analysis, presented in Chapter 6. Its aim was twofold: on the one hand provide a conclusive evidence for the location of the central engine and on the other test and possibly quantify the absorption properties of a torus which, according to previous studies, should cover the inner portion of the counter-jet. A method combining the cross-correlation of various parameters of the jet (lateral intensity profiles, 2D total intensity, width profile and ridge line profile) was employed for determining the core-shifts between maps at 5 frequencies, in the range between 8 and 86 GHz. After the maps were correctly aligned, the spectral profiles across the ridge line and spectral maps were produced. The spectrally most inverted region coincides remarkably well at all frequencies with the location of the gap of emission, featuring a spectral index between +0.5 and +2.5 ($S_\nu \propto \nu^\alpha$). This is perfectly consistent with the expectations for a self-absorbed region at the base of the two- sided jet. In the counter-jet, the spectral index is flat or inverted ($\alpha > 0$), signaling the presence of free-free absorption, while the spectrum in the jet side is rather steep ($\alpha \sim -1$). In order to more precisely locate the absorber, a spectral fitting was performed after binning the jets in small intervals of 0.18 mas. This analysis indicates that, actually, both jet and counter-jet may suffer from free-free absorption at the lowest frequencies, at 8 GHz and sometimes at 15 GHz. However, part of the counter-jet is characterized by an inverted spectrum up to 86 GHz, therefore the absorber should have an higher turnover frequency at this location. The opacity of this material was quantified by also fitting a free-free absorption spectrum to the data, which indeed suggests the presence of an absorber with two components: a diffuse

¹Innermost Stable Circular Orbit

one spread homogeneously across the source and a denser and/or colder component with higher compactness and confined between ~ 0.5 and 1.5 parsecs from the central engine. Assuming a temperature $T = 10^4$ K and a path length of 1 parsec, a maximum electron density $n_e = (7.4 \pm 0.7) \times 10^4$ cm $^{-3}$ is inferred for this material. For Cygnus A, this is the first evidence for the presence of such a dense absorber on sub-parsec scales, expected in classical unified scheme for AGN but never clearly detected on small scales. Only one VLBI study searching for excited OH ([Impellizzeri et al. 2006](#)) had resulted in a tentative detection of a diffuse material spread over the entire source, compatible with the diffuse component also detected in this study. Given the high compactness of the dense component, previous studies were likely missing the necessary resolution for detecting it.

In conclusion, this thesis has provided a comprehensive view of the jet launching region in Cygnus A. The analysis presented here should certainly be improved in the future for consolidating the proposed interpretations. For example, detecting the counter-jet with an higher SNR would allow the approaching and receding sides to be more solidly compared, in order to test the symmetry properties expected in the unified scheme. As a part of the work of this thesis, several proposals for new data were submitted and accepted. The higher recording rates currently employed in VLBI observations promise a much improved sensitivity, which will certainly facilitate the investigation of the counter-jet in even greater detail.

The study of the obscuring torus in Cygnus A also represents a fundamental test of the unified scheme for AGN, and the results presented should be more deeply investigated. A set of truly simultaneous multi-frequency VLBI observations in a broader frequency range would be required for this scope.

Appendix A

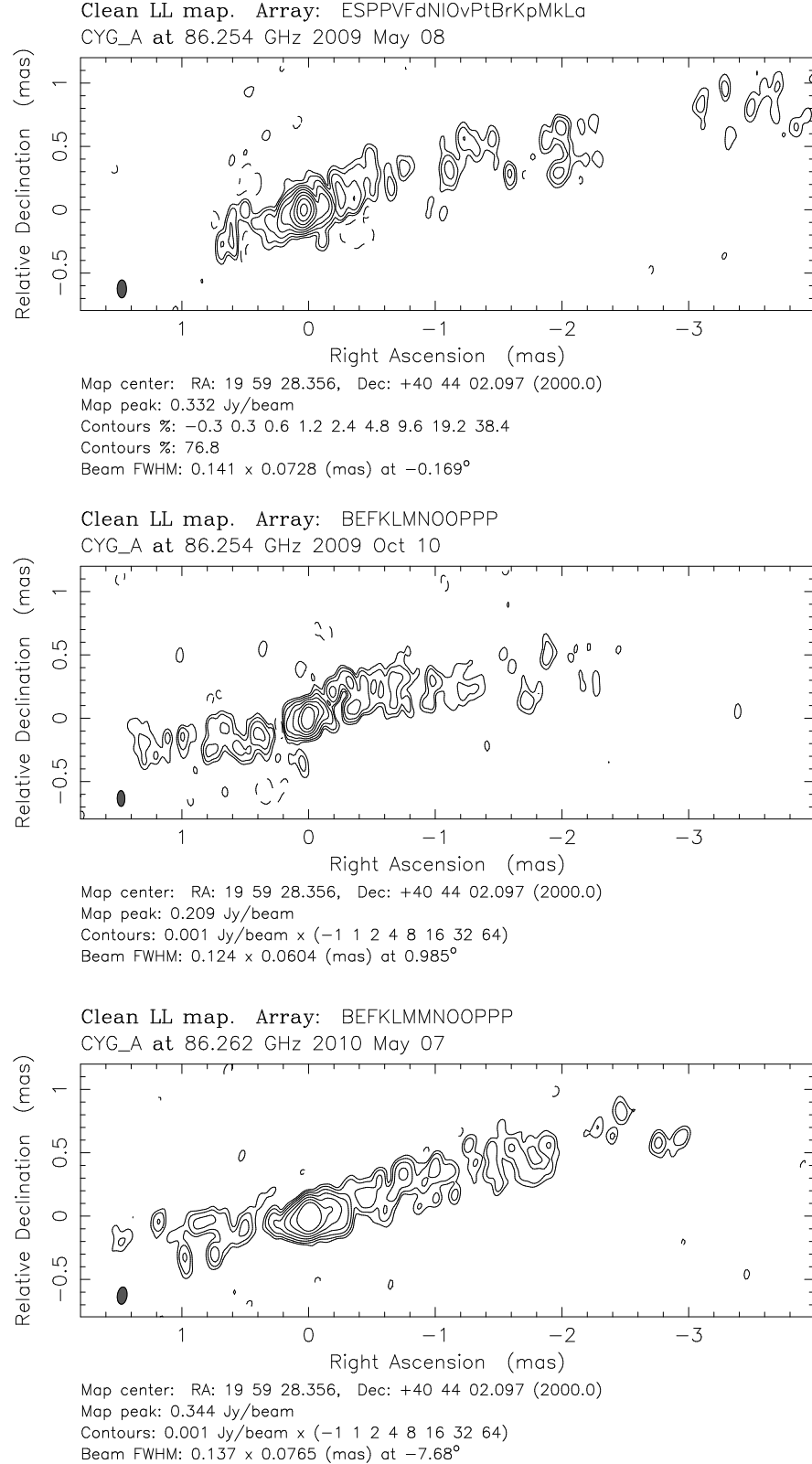


Figure A.1: Clean maps of Cygnus A at 86 GHz from GMVA observations in 2009-2010. A taper of 0.1 at a uv-radius of $2500 M\lambda$ was applied.

Bibliography

- Agudo, I., Thum, C., Wiesemeyer, H., & Krichbaum, T. P. 2010, ApJS, 189, 1
- Alef, W. & Porcas, R. W. 1986, A&A, 168, 365
- Antonucci, R. 1993, ARA&A, 31, 473
- Antonucci, R., Hurt, T., & Kinney, A. 1994, Nature, 371, 313
- Antonucci, R. R. J. & Miller, J. S. 1985, ApJ, 297, 621
- Asada, K. & Nakamura, M. 2012, ApJ, 745, L28
- Bach, U., Kadler, M., Krichbaum, T. P., et al. 2003, in Proceedings of the Second ENIGMA Meeting, ed. C. M. Raiteri & M. Villata, 216–223
- Bach, U., Krichbaum, T. P., Middelberg, E., Alef, W., & Zensus, A. J. 2008, in The role of VLBI in the Golden Age for Radio Astronomy, 108
- Balbus, S. A. & Hawley, J. F. 1991, ApJ, 376, 214
- Bartel, N., Sorathia, B., Bietenholz, M. F., Carilli, C. L., & Diamond, P. 1995, Proceedings of the National Academy of Science, 92, 11371
- Barthel, P. D. 1989, ApJ, 336, 606
- Begelman, M. C. 1979, MNRAS, 187, 237
- Begelman, M. C. & Li, Z.-Y. 1994, ApJ, 426, 269
- Beskin, V. S., Kuznetsova, I. V., & Rafikov, R. R. 1998, MNRAS, 299, 341
- Beskin, V. S. & Nokhrina, E. E. 2006, MNRAS, 367, 375
- Bianchi, S., Panessa, F., Barcons, X., et al. 2012, MNRAS, 426, 3225
- Blandford, R. D. & Königl, A. 1979, ApJ, 232, 34

- Blandford, R. D. & McKee, C. F. 1982, ApJ, 255, 419
- Blandford, R. D. & Payne, D. G. 1982, MNRAS, 199, 883
- Blandford, R. D. & Znajek, R. L. 1977, MNRAS, 179, 433
- Böttcher, M., Harris, D. E., & Krawczynski, H. 2012, Introduction and Historical Perspective, ed. M. Boettcher, D. E. Harris, & H. Krawczynski, 1–16
- Brandenburg, A., Nordlund, A., Stein, R. F., & Torkelsson, U. 1995, ApJ, 446, 741
- Burtscher, L., Meisenheimer, K., Tristram, K. R. W., et al. 2013, A&A, 558, A149
- Carilli, C. L., Bartel, N., & Linfield, R. P. 1991, AJ, 102, 1691
- Carilli, C. L. & Barthel, P. D. 1996, A&A Rev., 7, 1
- Carilli, C. L., Perley, R. A., & Harris, D. E. 1994, MNRAS, 270, 173
- Chiaberge, M., Capetti, A., & Celotti, A. 1999, A&A, 349, 77
- Chiaberge, M., Gilli, R., Lotz, J., & Norman, C. 2015, ArXiv e-prints
- Chiuderi, C. & Velli, M. 2012, Fisica del Plasma
- Clausen-Brown, E. 2012, PhD thesis, Purdue University
- Contopoulos, I., Gabuzda, D., & Kylafis, N., eds. 2015, Astrophysics and Space Science Library, Vol. 414, The Formation and Disruption of Black Hole Jets
- Contopoulos, J. 1995, ApJ, 446, 67
- Contopoulos, J. & Lovelace, R. V. E. 1994, ApJ, 429, 139
- Cotton, W. D. 1995, in Astronomical Society of the Pacific Conference Series, Vol. 82, Very Long Baseline Interferometry and the VLBA, ed. J. A. Zensus, P. J. Diamond, & P. J. Napier, 189
- Curran, S. J., Whiting, M. T., Combes, F., et al. 2011, MNRAS, 416, 2143
- Daly, R. A. & Marscher, A. P. 1988, ApJ, 334, 539
- Doeleman, S. S., Fish, V. L., Schenck, D. E., et al. 2012, Science, 338, 355
- Eckart, A., Genzel, R., Ott, T., & Schödel, R. 2002, MNRAS, 331, 917
- Edelson, R. A. & Malkan, M. A. 1986, ApJ, 308, 59

- Fanaroff, B. L. & Riley, J. M. 1974, MNRAS, 167, 31P
- Fendt, C. & Sheiknezami, S. 2013, ApJ, 774, 12
- Ferrarese, L. & Merritt, D. 2000, ApJ, 539, L9
- Fomalont, E. B. 1989, in Astronomical Society of the Pacific Conference Series, Vol. 6, Synthesis Imaging in Radio Astronomy, ed. R. A. Perley, F. R. Schwab, & A. H. Bridle, 213
- García-Burillo, S., Combes, F., Usero, A., et al. 2014, A&A, 567, A125
- Garofalo, D., Evans, D. A., & Sambruna, R. M. 2010, MNRAS, 406, 975
- Ghisellini, G., Tavecchio, F., & Chiaberge, M. 2005, A&A, 432, 401
- Ghisellini, G., Tavecchio, F., Maraschi, L., Celotti, A., & Sbarato, T. 2014, Nature, 515, 376
- Giroletti, M., Giovannini, G., Feretti, L., et al. 2004, ApJ, 600, 127
- Gopal-Krishna & Wiita, P. J. 2002, New A Rev., 46, 357
- Greisen, E. W. 1990, in Acquisition, Processing and Archiving of Astronomical Images, ed. G. Longo & G. Sedmak, 125–142
- Gubbay, J., Legg, A. J., Robertson, D. S., et al. 1969, Nature, 224, 1094
- Haardt, F. & Maraschi, L. 1991, ApJ, 380, L51
- Hada, K., Doi, A., Kino, M., et al. 2011, Nature, 477, 185
- Hardee, P., Mizuno, Y., & Nishikawa, K.-I. 2007, Ap&SS, 311, 281
- Harris, D. E., Carilli, C. L., & Perley, R. A. 1994, Nature, 367, 713
- Högbom, J. A. 1974, A&AS, 15, 417
- Homan, D. C., Lister, M. L., Kovalev, Y. Y., et al. 2014, ArXiv e-prints
- Hovatta, T., Valtaoja, E., Tornikoski, M., & Lähteenmäki, A. 2009, A&A, 494, 527
- Hughes, P. A. 1991, Beams and jets in astrophysics
- Impellizzeri, V., Roy, A. L., & Henkel, C. 2006, in Proceedings of the 8th European VLBI Network Symposium, 35
- Ito, H., Kino, M., Kawakatu, N., Isobe, N., & Yamada, S. 2008, ApJ, 685, 828

- Jaffe, W., Meisenheimer, K., Röttgering, H. J. A., et al. 2004, *Nature*, 429, 47
- Karamanavis, V. 2015, PhD thesis, University of Cologne
- Kellermann, K. I. & Pauliny-Toth, I. I. K. 1969, *ApJ*, 155, L71
- Khachikian, E. Y. & Weedman, D. W. 1974, *ApJ*, 192, 581
- Komissarov, S. S., Barkov, M. V., Vlahakis, N., & Königl, A. 2007, *MNRAS*, 380, 51
- Königl, A. 1981, *ApJ*, 243, 700
- Kovalev, Y. Y., Lister, M. L., Homan, D. C., & Kellermann, K. I. 2007, *ApJ*, 668, L27
- Krichbaum, T. P., Alef, W., Witzel, A., et al. 1998, *A&A*, 329, 873
- Krolik, J. H. & Begelman, M. C. 1988, *ApJ*, 329, 702
- Li, Z.-Y., Chiueh, T., & Begelman, M. C. 1992, *ApJ*, 394, 459
- Lister, M. L., Aller, M. F., Aller, H. D., et al. 2013, *AJ*, 146, 120
- Lister, M. L., Cohen, M. H., Homan, D. C., et al. 2009, *AJ*, 138, 1874
- Lobanov, A. P. 2005, ArXiv Astrophysics e-prints
- Lobanov, A. P. & Zensus, J. A. 2001, *Science*, 294, 128
- Lynden-Bell, D. 1969, *Nature*, 223, 690
- Lynden-Bell, D. 1996, *MNRAS*, 279, 389
- Lyubarsky, Y. 2009, *ApJ*, 698, 1570
- Mack, K.-H., Klein, U., O'Dea, C. P., & Willis, A. G. 1997, *A&AS*, 123, 423
- Markowitz, A. G., Krumpe, M., & Nikutta, R. 2014, *MNRAS*, 439, 1403
- Marscher, A. P. 1983, *ApJ*, 264, 296
- Marscher, A. P. 1996, in *Astronomical Society of the Pacific Conference Series*, Vol. 100, Energy Transport in Radio Galaxies and Quasars, ed. P. E. Hardee, A. H. Bridle, & J. A. Zensus, 45
- Matthews, T. A., Morgan, W. W., & Schmidt, M. 1964, *ApJ*, 140, 35
- Matthews, T. A. & Sandage, A. R. 1963, *ApJ*, 138, 30
- McKinney, J. C. 2006, *MNRAS*, 368, 1561

- Meier, D. L. 2012, Black Hole Astrophysics: The Engine Paradigm
- Meyer, L., Ghez, A. M., Schödel, R., et al. 2012, *Science*, 338, 84
- Michel, F. C. 1969, *ApJ*, 158, 727
- Miyoshi, M., Moran, J., Herrnstein, J., et al. 1995, *Nature*, 373, 127
- Moderski, R., Sikora, M., & Lasota, J.-P. 1998, *MNRAS*, 301, 142
- Moran, J. M. 1976, *Methods of Experimental Physics*, 12, 228
- Mortlock, D. J., Warren, S. J., Venemans, B. P., et al. 2011, *Nature*, 474, 616
- Müller, C., Kadler, M., Ojha, R., et al. 2011, *A&A*, 530, L11
- Nagai, H., Haga, T., Giovannini, G., et al. 2014, *ApJ*, 785, 53
- Narayan, R., Igumenshchev, I. V., & Abramowicz, M. A. 2003, *PASJ*, 55, L69
- Narayan, R. & Yi, I. 1994, *ApJ*, 428, L13
- Netzer, H. 2015, ArXiv e-prints
- Owen, F. N., Ledlow, M. J., Morrison, G. E., & Hill, J. M. 1997, *ApJ*, 488, L15
- Panessa, F. & Bassani, L. 2002, *A&A*, 394, 435
- Panessa, F. & Giroletti, M. 2013, *MNRAS*, 432, 1138
- Peebles, P. J. E. 1972, *ApJ*, 178, 371
- Peterson, B. M. 2006, in Lecture Notes in Physics, Berlin Springer Verlag, Vol. 693, Physics of Active Galactic Nuclei at all Scales, ed. D. Alloin, 77
- Peterson, B. M. 2014, *Space Sci. Rev.*, 183, 253
- Privon, G. C., Baum, S. A., O'Dea, C. P., et al. 2012, *ApJ*, 747, 46
- Pushkarev, A. B., Hovatta, T., Kovalev, Y. Y., et al. 2012, *A&A*, 545, A113
- Pushkarev, A. B., Kovalev, Y. Y., Lister, M. L., & Savolainen, T. 2009, *A&A*, 507, L33
- Raban, D., Jaffe, W., Röttgering, H., Meisenheimer, K., & Tristram, K. R. W. 2009, *MNRAS*, 394, 1325
- Rees, M. J. 1966, *Nature*, 211, 468
- Rees, M. J. 1970, *Nature*, 227, 1303

- Reynolds, C. S. 2014, *Space Sci. Rev.*, 183, 277
- Reynolds, C. S., Garofalo, D., & Begelman, M. C. 2006, *ApJ*, 651, 1023
- Robson, I. 1996, Active galactic nuclei
- Rohlfs, K. & Wilson, T. L. 1996, Tools of Radio Astronomy
- Rothstein, D. M. & Lovelace, R. V. E. 2008, *ApJ*, 677, 1221
- Ryle, M. & Hewish, A. 1960, *MNRAS*, 120, 220
- Ryle, M. & Vonberg, D. D. 1946, *Nature*, 158, 339
- Sadowski, A., Narayan, R., McKinney, J. C., & Tchekhovskoy, A. 2014, *MNRAS*, 439, 503
- Salpeter, E. E. 1964, *ApJ*, 140, 796
- Sawada-Satoh, S., Kameno, S., Nakamura, K., Namikawa, D., & Shibata, K. M. 2009, *Astronomische Nachrichten*, 330, 249
- Scheuer, P. A. G. & Readhead, A. C. S. 1979, *Nature*, 277, 182
- Schinzel, F. K., Lobanov, A. P., Taylor, G. B., et al. 2012, *A&A*, 537, A70
- Schmidt, M. 1963, *Nature*, 197, 1040
- Schwab, F. R. & Cotton, W. D. 1983, *AJ*, 88, 688
- Seyfert, C. K. 1943, *ApJ*, 97, 28
- Shakura, N. I. & Sunyaev, R. A. 1973, *A&A*, 24, 337
- Shepherd, M. C., Pearson, T. J., & Taylor, G. B. 1994, in *Bulletin of the American Astronomical Society*, Vol. 26, *Bulletin of the American Astronomical Society*, 987–989
- Sokolovsky, K. V., Kovalev, Y. Y., Pushkarev, A. B., & Lobanov, A. P. 2011, *A&A*, 532, A38
- Sol, H., Pelletier, G., & Asseo, E. 1989, *MNRAS*, 237, 411
- Soltan, A. 1982, *MNRAS*, 200, 115
- Spruit, H. C. 2010, in *Lecture Notes in Physics*, Berlin Springer Verlag, Vol. 794, *Lecture Notes in Physics*, Berlin Springer Verlag, ed. T. Belloni, 233
- Spruit, H. C., Foglizzo, T., & Stehle, R. 1997, *MNRAS*, 288, 333
- Stickel, M., Padovani, P., Urry, C. M., Fried, J. W., & Kuehr, H. 1991, *ApJ*, 374, 431

- Struve, C. & Conway, J. E. 2010, A&A, 513, A10
- Suganuma, M., Yoshii, Y., Kobayashi, Y., et al. 2006, ApJ, 639, 46
- Tacconi, L. J., Genzel, R., Blietz, M., et al. 1994, ApJ, 426, L77
- Tadhunter, C., Marconi, A., Axon, D., et al. 2003, MNRAS, 342, 861
- Taylor, G. B., Carilli, C. L., & Perley, R. A., eds. 1999, Astronomical Society of the Pacific Conference Series, Vol. 180, Synthesis Imaging in Radio Astronomy II
- Tchekhovskoy, A., McKinney, J. C., & Narayan, R. 2008, MNRAS, 388, 551
- Tchekhovskoy, A., McKinney, J. C., & Narayan, R. 2009, ApJ, 699, 1789
- Tchekhovskoy, A., Narayan, R., & McKinney, J. C. 2011, MNRAS, 418, L79
- Thirring, H. 1918, Physikalische Zeitschrift, 19, 33
- Tomimatsu, A. 1994, PASJ, 46, 123
- Türler, M., Courvoisier, T. J.-L., & Paltani, S. 1999, A&A, 349, 45
- Urry, C. M. & Padovani, P. 1995, PASP, 107, 803
- Uzdensky, D. A. & MacFadyen, A. I. 2006, ApJ, 647, 1192
- vanden Berk, D., Yip, C., Connolly, A., Jester, S., & Stoughton, C. 2004, in Astronomical Society of the Pacific Conference Series, Vol. 311, AGN Physics with the Sloan Digital Sky Survey, ed. G. T. Richards & P. B. Hall, 21
- Vlahakis, N. & Königl, A. 2004, ApJ, 605, 656
- Wald, R. M. 1974, Phys. Rev. D, 10, 1680
- Xie, W., Lei, W.-H., Zou, Y.-C., et al. 2012, Research in Astronomy and Astrophysics, 12, 817
- Xu, C., Baum, S. A., O'Dea, C. P., Wrobel, J. M., & Condon, J. J. 2000, AJ, 120, 2950
- Zamaninasab, M., Clausen-Brown, E., Savolainen, T., & Tchekhovskoy, A. 2014, Nature, 510, 126
- Zel'dovich, Y. B. & Novikov, I. D. 1964, Soviet Physics Doklady, 9, 246

Acknowledgments

The completion of this thesis work is not only the result of my dedication, but also of the contribution of many others.

First of all, I am grateful to all those people who gave me the chance to study, learn and progress in these three years. Although I often forget it, this makes me extremely lucky and privileged. Therefore I deeply thank Prof. Zensus for this opportunity and for the trust he showed me, and my second referee Prof. Eckart for following my progress over time. I am also grateful to my advisor Dr. Thomas Krichbaum for his support and for being always passionate about science. Our discussions have been exhausting for me sometimes, but also made me think, argue and learn more.

Being part of the IMPRS was another important element in my PhD experience. I have very much enjoyed the activities of the school, both educational and recreational. I am thankful for this to Manolis, Rainer and Simone, who have always put much effort in their work, and to all the IMPRS students in Bonn and Cologne.

In these three years I have also been part of the VLBI group. Working with such friendly people was truly helpful, both when having a scientific discussion or a beer out. I thank all the members and especially Uwe, Eduardo, Andrei, Tuomas and Stefanie. And of course Richard! Meeting the “philosopher” of the VLBI group was a real pleasure for me, and I will always remember our long conversations.

A special place needs to be dedicated to my fellow PhD students and to the other young researchers of the group. I have had a lot of fun with you guys and I feel I cannot thank you enough. Vassilis, Laura, Florent, Jeff, Ioannis, Dhania, Bindu, Shoko, Sebastian, Christoph, Moritz, Mohammed, Eric. Thank you from the bottom of my heart!

In these three years I have met many nice people, and deep friendships were consolidated. Without them my life in Bonn would have been much harder. Therefore I thank Alice. Together we have been on a roller coaster of emotions, and I know we will always be there for each other. I thank Monica for being such a sensible and wonderful woman. And of course Gabriele, Andrea, Lorenzo, Alberto (il sardo ed il lungo), Luca, Emiliano, Carlo e Sara... a magic ensemble of amazing people.

Finally, I thank my family for being my true lifeline.

Bonn, 31 August 2015

Erklärung

Ich versichere, dass ich die von mir vorgelegte Dissertation selbständig angefertigt, die benutzten Quellen und Hilfsmittel vollständig angegeben und die Stellen der Arbeit, einschließlich Tabellen, Karten und Abbildungen, die anderen Werken im Wortlaut oder dem Sinn nach entnommen sind, in jedem Einzelfall als Entlehnung kenntlich gemacht habe; dass diese Dissertation noch keiner anderen Fakultät oder Universität zur Prüfung vorgelegen hat; dass sie, abgesehen von unten angegebenen Teilpublikationen – noch nicht veröffentlicht worden ist sowie, dass ich eine solche Veröffentlichung vor Abschluss des Promotionsverfahrens nicht vornehmen werde. Die Bestimmungen der Promotionsordnung sind mir bekannt. Die von mir vorgelegte Dissertation ist von Prof. Dr. J. Anton Zensus und Prof. Dr. Andreas Eckart betreut worden.

Köln, den 31.08.2015

Publication / Teilpublikationen

- The stratified two-sided jet of Cygnus A. Acceleration and collimation. **Boccardi, B.**, Krichbaum T.P., Bach, U., Mertens, F., Ros, E., Alef, W., and Zensus J.A., 2016, A&A, 585, A33
- High resolution mm-VLBI imaging of Cygnus A. **Boccardi, B.**; Krichbaum, T. P.; Bach, U.; Ros, E.; Zensus, A. J. Proceedings of the 12th European VLBI Network Symposium and Users Meeting (EVN 2014). 7-10 October 2014. Cagliari, Italy.
- Radio and Gamma-ray emission in nearby BL Lacs. Giovannini, G.; Liuzzo, E.; **Boccardi, B.**; Giroletti, M. Multiwavelength AGN Surveys and Studies, Proceedings of the International Astronomical Union, IAU Symposium, Volume 304, pp. 200-203
- Radio and gamma-ray emission in faint BL Lacs. Liuzzo, E.; **Boccardi, B.**; Giroletti, M.; Giovannini, G., 11th European VLBI Network Symposium, ed. P. Charlot et al., Bordeaux (France), October 9-12, 2012
- Exploring the bulk of the BL Lacertae object population. I. Parsec-scale radio structures. Liuzzo, E.; Giroletti, M.; Giovannini, G.; **Boccardi, B.**; Tamburri, S.; Taylor, G. B.; Casadio, C.; Kadler, M.; Tosti, G.; Mignano, A., 2013, A&A, 560, 23
- Radio properties of faint BL Lacs. (Liuzzo+, 2013) Liuzzo, E.; Giroletti, M.; Giovannini, G.; **Boccardi, B.**; Tamburri, S.; Taylor, G. B.; Casadio, C.; Kadler, M.; Tosti, G.; Mignano, A., 2013, yCat, 35609023
- Exploring the bulk of the BL Lac object population: parsec scale radio properties and gamma ray emission. Giovannini, G.; Liuzzo, E.; Giroletti, M.; **Boccardi, B.**; Tamburri, S.; Casadio, C.; Taylor, G. B.; Kadler, M.; Tosti, G.; Mignano, A., 2013, EPJWC, 6108006

Lebenslauf

Persönliche Daten

Biagina Boccardi

Geburtsdatum: 11. April 1986

Geburtsort: San Giovanni Rotondo, Italien

Staatsangehörigkeit: Italienisch

Anschrift

Max-Planck-Institut für Radioastronomie

Auf dem Hügel 69

53121 Bonn

Deutschland

email: bboccardi@mpifr-bonn.mpg.de

Ausbildung

- 2012–2015 Doktorand an der Universität zu Köln und dem
Max-Planck-Institut für Radioastronomie in Bonn
Stipendium der International Max Planck Research School for
Astronomy and astrophysics
wiss. Betreuer Dr. Thomas P. Krichbaum und
Prof. Dr. J. Anton Zensus
Titel: “*The two-sided relativistic outflow in Cygnus A: extragalactic jet physics
at extreme spatial resolution*”
- 2005–2012 Diplomstudent an der Università di Bologna,
Diplom Physik
wiss. Betreuer Prof. Dr. Gabriele Giovannini
Titel: “*Nuclear properties of a sample of BL Lac
objects in the radio and gamma-ray bands*”
- 2000–2005 Allgemeine Hochschulreife am Liceo Scientifico Alfano da
Termoli, Termoli, Italien